

Department of Precision and Microsystems Engineering

**The design of a planar precision stage using
cost effective optical mouse sensors**

Gihin Mok

Report no	: MSD 2015.002
Coach	: ir. J.W Spronck
Professor	: Prof. dr. ir. J.L. Herder
Specialisation	: Mechatronic System Design
Type of report	: Master Thesis
Date	: 29 January 2015

THE DESIGN OF A PLANAR PRECISION STAGE USING COST EFFECTIVE OPTICAL MOUSE SENSORS

by

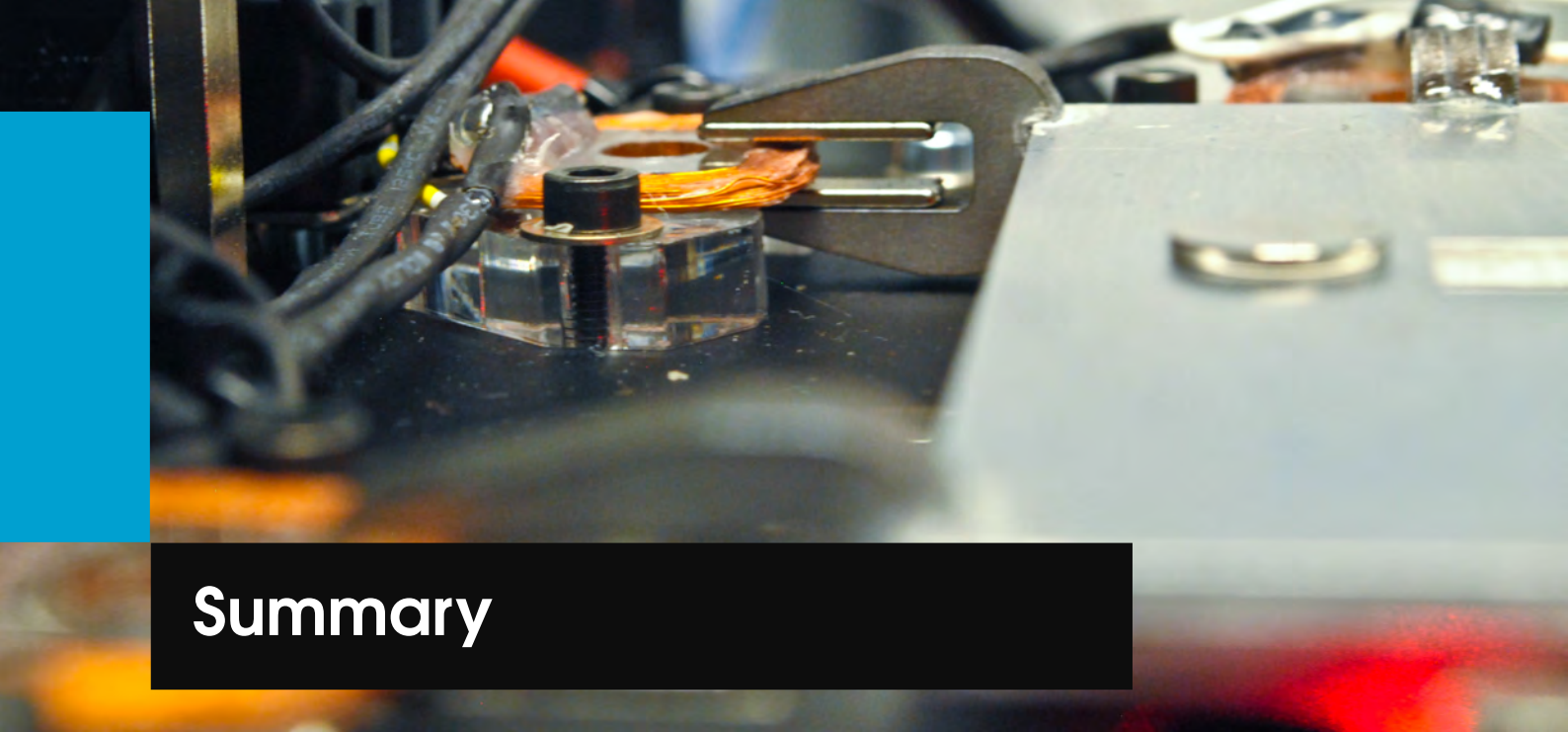
Gihin Mok

in partial fulfillment of the requirements for the degree of

Master of Science
in Mechanical Engineering

at the Delft University of Technology,
to be presented on Thursday January 29, 2015 at 12:45.

Supervisor: ir. J.W. Spronck
Thesis committee: Prof. dr. ir. J.L. Herder, TU Delft
dr. ir. B.A.J. Lenseigne, TU Delft



Summary

To reduce the cost of sub-micrometer precision stages, a new sensor system needs to be found. Optical computer mouse sensors might be a suitable candidate. They are low cost because of mass production, can measure planar displacements and have unlimited stroke. Leading to the following thesis objective: *"Design of a new sensor system with micrometer precision using cost effective off-the-shelf optical mouse sensors, and integrate this sensor system in a planar stage system design"*. The internal operation of the mouse is left as a black box and is not within the scope of this thesis.

A suitable sensor is selected with the following criteria: resolution, dynamic performance, compactness and ease of use. The ADNS 9800 optical mouse sensor chip, normally used in high-end gaming mouses turned out to meet these requirements best. This sensor takes pictures of the measurement surface with a photodiode array and compares these pictures to determine the displacement. Interpixel interpolation can be used to achieve a resolution of up to $3\mu\text{m}$. To get the position, the displacement signal needs to be integrated introducing an integration error. This integration error needs to be reset periodically, to avoid the accumulation of error.

With an optical magnification the resolution can be enhanced even more. This optical magnification can be done with an external lens. However, this increase in resolution is inverse proportional with the maximum tracking speed. Another problem is the light intensity on the sensor, which decreases quadratically with the magnification. Therefore, an externally focused laser has been used to illuminate the measurement surface.

To validate the mouse sensor and the magnification concept, an experimental setup is built. The optical mouse sensor is positioned above a motion controlled stage with its own reference measurement. Steps of $50\mu\text{m}$ to 10mm are made with predefined mouse settings, measurement surfaces, sensor heights, velocity and acceleration profiles. The output of the optical mouse sensor is compared with the reference encoder of the stage to determine the precision and sensitivity of the optical mouse sensor. The sensitivity is defined as the amount of incremental displacement counts of the mouse sensor per traveled distance.

As known from literature, the sensitivity is dependent on the traveled distance of a step. Meaning that smaller steps (below $200\mu\text{m}$) have a decreasing sensitivity with lower step sizes. While for larger step sizes (above $2000\mu\text{m}$) the sensitivity remained constant. With optical magnification the sensor "sees" a larger displacement. Resulting in a constant sensitivity, even for step sizes of $50\mu\text{m}$. Hence, making magnification even more important, it keeps the sensor sensitivity constant for different step sizes

and additionally increases the resolution.

The precision of the sensor increases with higher magnifications, up till a maximum of $19\times$. The measurement precision of the sensor is displacement dependent due to the accumulation of error, the 3σ value is 0.1% of the traveled distance. The maximum acceleration and velocity before the sensitivity and precision deteriorates are 500mm/s^2 and 30mm/s respectively for this magnification.

With these results, the sensor meets the requirements for microscopy applications such as blood research or production inspection of bonding pads of chips (e.g. a blood cell and the smallest bonding wire have a diameter of 8 and $17.5\mu\text{m}$ respectively). From these applications the requirements for the stage were deduced. Since this stage is a demonstrator extra design criteria were included, such as in-house producibility, adjustability and low cost electronics.

After extensive system design, simulation and validation, a compact and cost effective system has been realized, see Fig.1. Two optical mouse sensors measure from the bottom of the stage, in line with the region of interest. Lenses and mirrors are used to magnify the image up to $40\times$ and used for a more compact design, this magnification factor can be easily changed by interchanging the bottom plate.

Three Lorentz actuators are designed to actuate the stage in the 3 DOFs. A moving magnet configuration is chosen such that thermal expansion will not influence the region of interest. The mover is floating on a layer of ferrofluid, to decrease friction and remove stick-slip for higher positioning accuracy, see Fig.2.

Low cost and high thermal efficiency were the criteria to choose for switch-mode amplifiers. To reduce the high frequency current ripple a LC filter is added. A measurement circuit to measure the current is designed for validation and can be in current feedback control. All produced components are separately validated and meet the designed requirements.

Maximum velocity and sensor delay are challenges which needs to be solved by the control system design. To cope with the maximum tracking velocity of the optical mouse sensor, a cascaded velocity-position PID controller is designed. With a frequency sweep the dynamic behavior of the mouse was revealed. This dynamic behavior is caused by digital filtering integrated in the sensor and can be represented by a FIR filter with a cut-off frequency of 3.5Hz . With this information, a model based observer is designed to predict the movements of the stage, to counter the delay of the built-in filter of the optical mouse sensor.

The cost effective requirement applies on the peripheral equipment too. Therefore, the complete controller, observer, amplifier control and sensor read-out are implemented on an Arduino Due, a low cost microcontroller. The full system is supplied by a simple 12V DC adapter and runs on open source software.

A laser triangulation sensor is used as reference measurement system to calibrate and validate the system. This reference measurement system is not used in the feedback loop and is only used as a reference measurement. The system has a 3σ repeatability of $9.7\mu\text{m}$ and includes the measurement error of the optical mouse sensor and the servo error of the controller. The settling time for a 1mm step is 1.0s.

Reflecting back on the objective of this thesis. A cost effective micrometer resolution 2DOF precision sensor system using optical mouse sensors has been developed. These optical mouse sensors are successfully integrated into the planar stage system design, with a component cost of only €200,-.

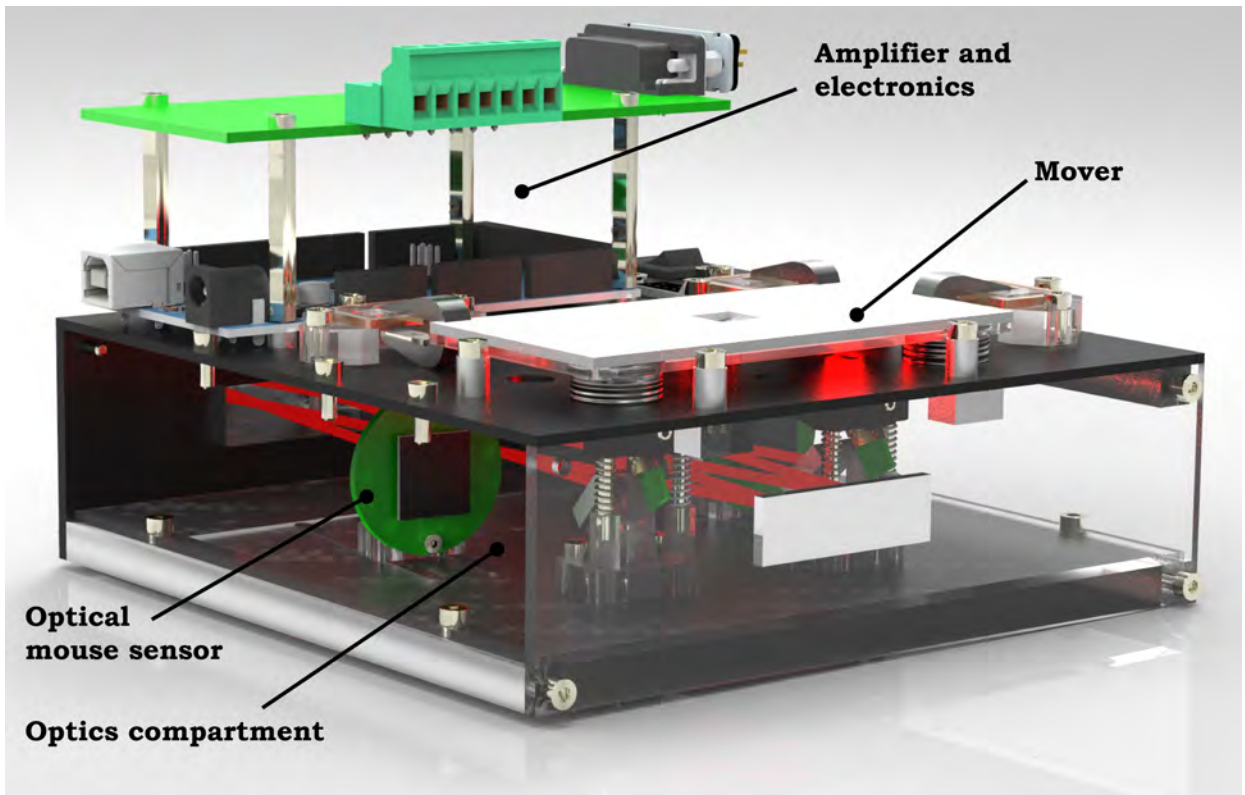


Figure 1: Visualization of the full positioning system. The front plate is made transparent for better visualization of the optics compartment. The red light originates from the diffuse reflection of the laser. The optics compartment magnifies the images which are projected on the optical mouse sensors.

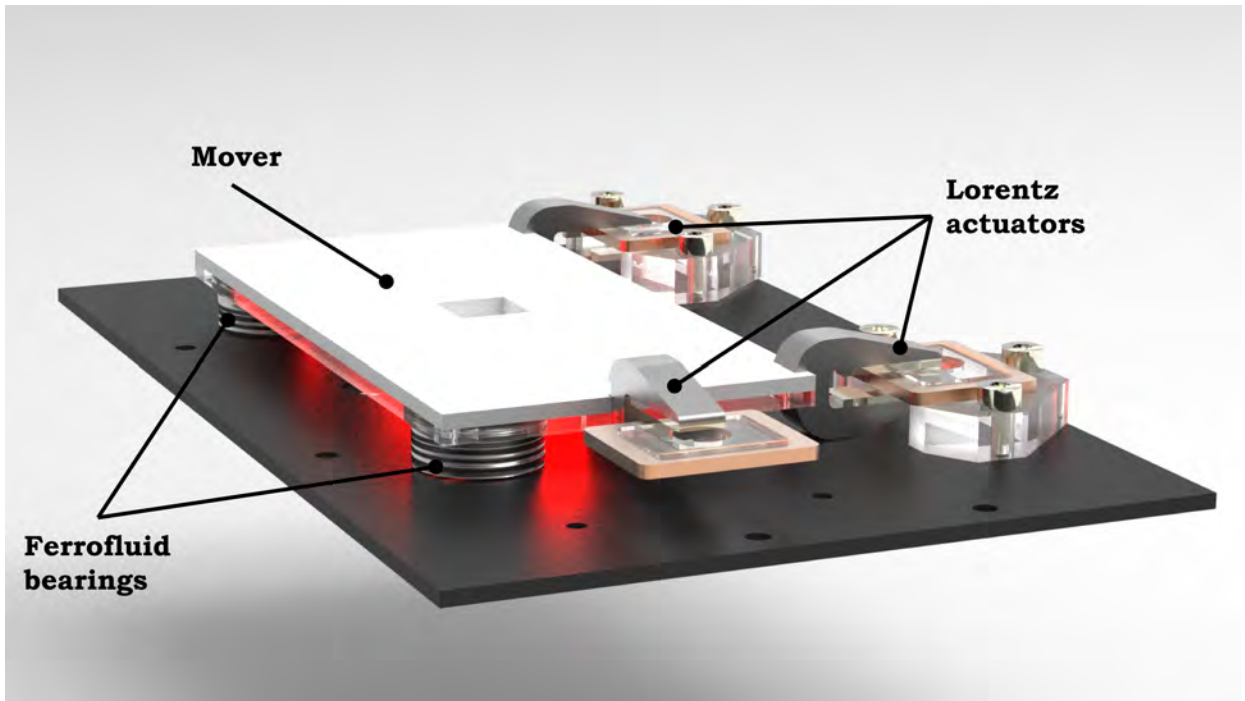
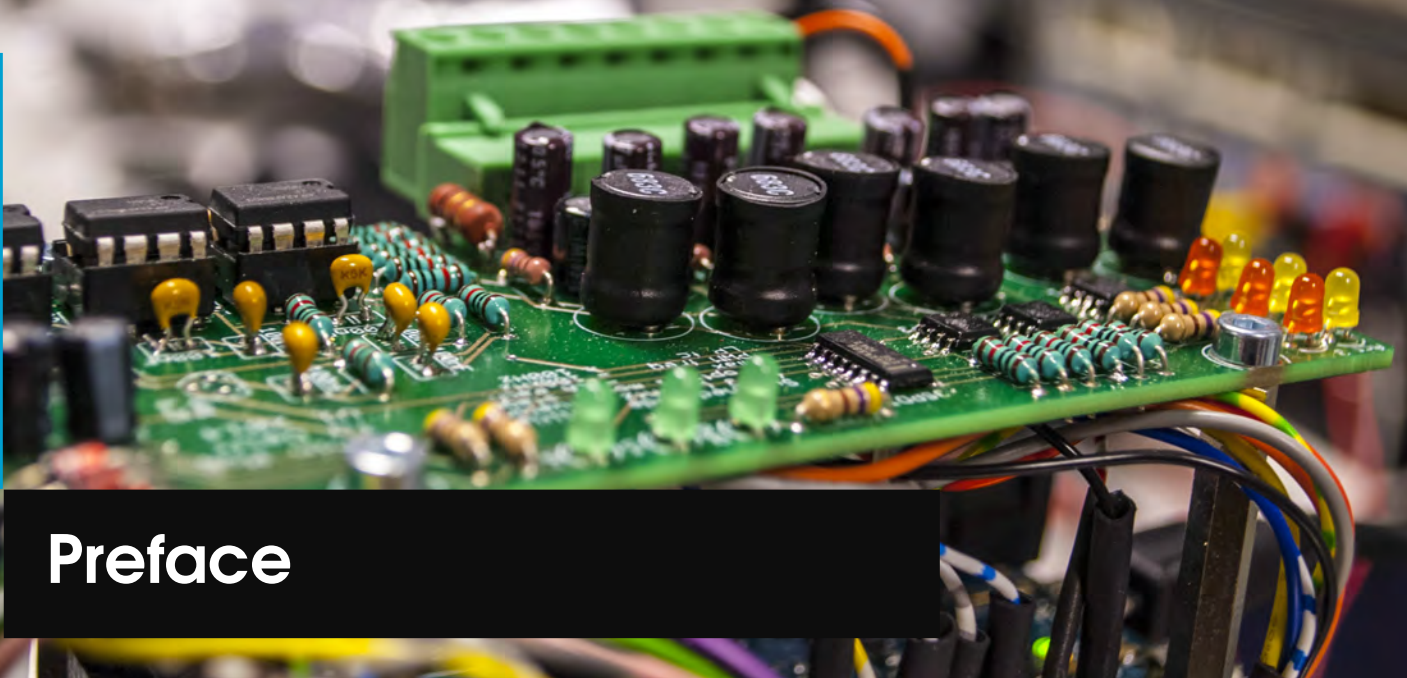


Figure 2: A close up on the mover showing the three Lorentz actuators. On the mover three magnet yokes are attached, while the coils are mounted on the base. The mounting of the front coils is hidden so that the coil can be seen. Three ferrofluid bearings are used for frictionless positioning, one of the bearings is hidden under the mover.



Preface

The last year was a journey I enjoyed very much. There were some downs, but mostly there were ups. I love the environment of the MSD group and made lots of new friends. The group is really close, making it easier to learn from each other. The long (not always technical) discussion during the coffee breaks, everyone trying to make his own 3D printer and our dream to fry a bitterbal of 1 cubic meter. It was awesome!

Besides the fun, I've also learned incredibly much. Some examples are scientifically conducting experiments, designing my own electronics and writing my own software. From now on I can also call myself an expert in the internals of "real" mice, by combining the search terms "Laser", "Mouse" and "Internals". But the most important lesson, no matter what you do, or what your problem is, you'll always end up with ferrofluids.

Acknowledgment

Hereby I would like to express my gratitude to everyone who contributed directly or indirectly to this thesis.

First of all I would like to thank Jo Spronck, he is not only my supervisor. He is also the mentor of this incredible group. First he encouraged us to spent more time together as group. Now he's telling us to get back to work, when we are drinking coffee (again). Thank you for the outstanding support and advice during the project. But more important, thanks for creating this fantastic working environment in this group.

Paul Ouwehand, thanks for all the in-depth discussions, proofreading, constant support and taking over my rotation sensor concept.

Arjan Meskers, thanks for all the advice about optics and how to write a good thesis. The 3D printing discussions were fun, with countless "I told you so"s.

Charlie van der Schoor, thanks for your 3D printing services for the stage and of course your outstanding talent for puns. We really missed you the last couple of months.

Oscar and Johan, thanks for the countless discussion and help when I'm stuck.

Ruud, Pjotr, Haris, Bart, Martijn, Rens, Arjan and Floris, thank you guys for proofreading, the discussions and the support.

Rob Luttjeboer, thanks for the assistance in the lab and ordering components.

René, thanks for your always happy mood and the assistance in the workshop.

Jos van Driel, thanks for the lab equipment and help with LabView.

Hassan HosseinNia, thanks for the advice for the controllers.

Merlijn van Spengen, thanks for the advice for the electronics.

Just Herder and Boris Lenseigne, thank you for taking the time to be in the exam committee.

I've mentioned the MSD group several times now, thank you all for all the fun and constructive discussions. I wish you guys success and good luck with your own theses!

I would like to thank my parents for their endless support through all those years.

At last but not least, the most important one, Carmen, my dear girlfriend. Thank you for supporting me through all those years. Your support is sincere and unconditionally, in everything I did. No matter what I did, studying, building racecars or as you say yourself "making tiny things I don't understand" you are always there and inspires me to do my best. I know that your new job demands a lot of you, still you are willing to help and take care of me during the last phase of this project. Even though you have no background in this work, you tried and that is what matters. Thank you again and let's book a flight to [destination of your choice]!



Contents

Summary	1
Preface	IV
1 Introduction	1
Sensor System Design	3
2 Optical mouse sensor	3
2.1 Working principle	3
2.1.1 Measuring surface	4
2.1.2 Mouse sensor as position sensor	6
2.2 Chip selection	6
2.2.1 ADNS 9800	6
2.3 Optical magnification	7
2.3.1 Geometric optics	7
2.3.2 Optical path length	7
2.3.3 Irradiance on the sensor	8
2.4 Conclusions	9
3 Sensor system concept validation	11
3.1 Experimental setup	11
3.1.1 Setup 1: Optimal settings	11
3.1.2 Setup 2: Higher resolution, magnification	12
3.1.3 Setup 3: Folding the optical path	13
3.1.4 Measurement method	13
3.2 Results	15
3.2.1 Measurement sensitivity and precision	15
3.2.2 The effects of magnification	16
3.2.3 Velocity and acceleration limitation	17
3.2.4 Sensitivity over full stroke	17
3.2.5 Error build-up	17
3.2.6 Sensor delay	17
3.3 Conclusions	17

Planar Stage System Design	18
4 Pre-design	19
4.1 Requirements	19
4.1.1 Bandwidth and error rejection	20
4.1.2 Additional design goals	20
4.2 Conceptual overview of all subsystems	20
5 Detailed system design	21
5.1 Optics and sensors	21
5.1.1 Sensor placement	21
5.1.2 Reset error build-up	22
5.1.3 Optics assembly	22
5.1.4 Sensors and mirrors	23
5.2 Actuator	26
5.2.1 Lorentz force	26
5.2.2 Magnet and coil configuration	27
5.2.3 Magnetic circuit	28
5.2.4 Optimizing yoke shape	29
5.2.5 Coils	31
5.2.6 Validation	31
5.3 Amplifier	33
5.3.1 Dual-ended configuration	33
5.3.2 Output filter	33
5.3.3 Schematics	36
5.3.4 Board design	36
5.3.5 Validation	37
5.4 Mover	39
5.4.1 Bearings	39
5.4.2 Ferrofluids	39
5.4.3 Modal analysis	40
5.5 Conclusion: Final design	42
6 Control system design	45
6.1 Model	45
6.1.1 Control and velocity limit	45
6.1.2 Inner-loop design	46
6.1.3 Outer-loop design	47
6.2 System identification	49
6.3 Model based observer	54
6.4 Implementation	55
6.4.1 Structure	55
6.4.2 Control parameters	55
6.4.3 The Y and rotation DOFs	56
6.4.4 Difficulties	56
6.5 Conclusions	56
7 Results	57
7.1 Step response	57
7.2 Positioning precision	58

7.3	Positioning stability	59
7.4	Constant sensitivity	60
7.5	Conclusions	60
8	Conclusion	61
9	Recommendations	63
	References	65
A	Appendix	67
A.1	Market research	67
A.2	Laser rotation sensor	68
A.3	Laser alignment	72
A.4	Additional control concepts	74
A.5	Wiring demonstrator stage	75
A.6	Arduino structure	76
A.7	Drawing full system	78
A.8	Drawing mover	79
A.9	Reference sensor noise measurement	80
A.10	How to design your own electronics	81
B	Datasheets	85
B.1	ADNS 9800	86
B.2	Thorlabs Linear Stage DDSM100	92
B.3	MICRO-EPSILON optoNCDT 1402-5	93



1 Introduction

This thesis looks into the possibility of decreasing the cost of precision stages. A stage is a device which can be positioned either manually or motorized. They exist in all different sizes and sorts and are used from simple ink-jet printers to high tech nanometer precision lithography machines. Stages are widely used in microscopy too, adding motion control to these stages enables higher resolutions and the possibility to scan the whole specimen.

The market for microscopy stages is large, and prices starting at several thousands of euros are common. The resolution and precision of these stages are in the micrometer range, with maximum speeds of several mm/s. The results of the market research in microscopy stages can be found in Appendix A.1.

These stages consist of actuators, some sort of bearing and sensors. For high precision the costs of these parts can be high, driving up the cost of the stage. These costs can be in expensive sensor equipment or in the production of high tolerance parts. Sensor systems based on interferometry or capacitive sensing are expensive. However, cheaper rotary encoders can also become expensive, because they need precisely machined mechanical parts to reduce backlash and hysteresis. Therefore it is interesting to look for new sensor systems which are inherently cost effective and do not use high tolerance machined parts. This way the price of the stages can be reduced.

So a low cost, micrometer resolution sensor system needs to be found. For an effective microscope stage design, the sensor needs to preferably measure in both planar directions with reasonable long stroke. A computer mouse is a good potential candidate, it measures in planar direction, has an unlimited stroke and is low cost. However, can a computer mouse reach micrometer resolution and what about stability, drift and non-linearity?

Reformulating, can these, widely available, mass produced optical sensors be used as a position sensor on micrometer scale? Luckily, in literature some work has already been done.

The first patent of an optical mouse was filed in as early as 1986[1], but optical mouses only became commercially available about 15 years later. From this point, different researchers got the idea to use these cheap sensors for position measurement. A 2 DOF measurement proposal and characterization was done, achieving resolutions up to $65\mu\text{m}$ [2], followed by implementation in a manual microscope stage for region of interest tracking[3]. A research about how a second mouse can be used to measure

3DOFs was also performed[4]. A least squares method was presented to reduce this error by using multiple mouses for robot odometry[5]. Next to robots, more macro scale applications were found such as AGV's and vibration measurements[6][7]. However none of these works looked at the performance on small scale and in motion control applications. Therefore this thesis will look into if and how these mouse sensors can be used as precision position sensors and how they can be integrated in a planar stage.

Objective

Resulting in the following thesis goal: "*Design of a new sensor system with micrometer precision using cost effective off-the-shelf optical mouse sensors, and integrate this sensor system in a planar stage system design*". The internal operation of the mouse is left as a black box and is not within the scope of this thesis.

Requirements

The requirements for such a system should be in the same order as the specifications of the stages which are available on the market. This means that the stage should have a resolution in the sub-micrometer regime, a position precision of several microns and a speed of several mm/s. All this should be achieved while being more cost effective. More detailed design requirements will be discussed in Chapter 4.

Overview of this thesis

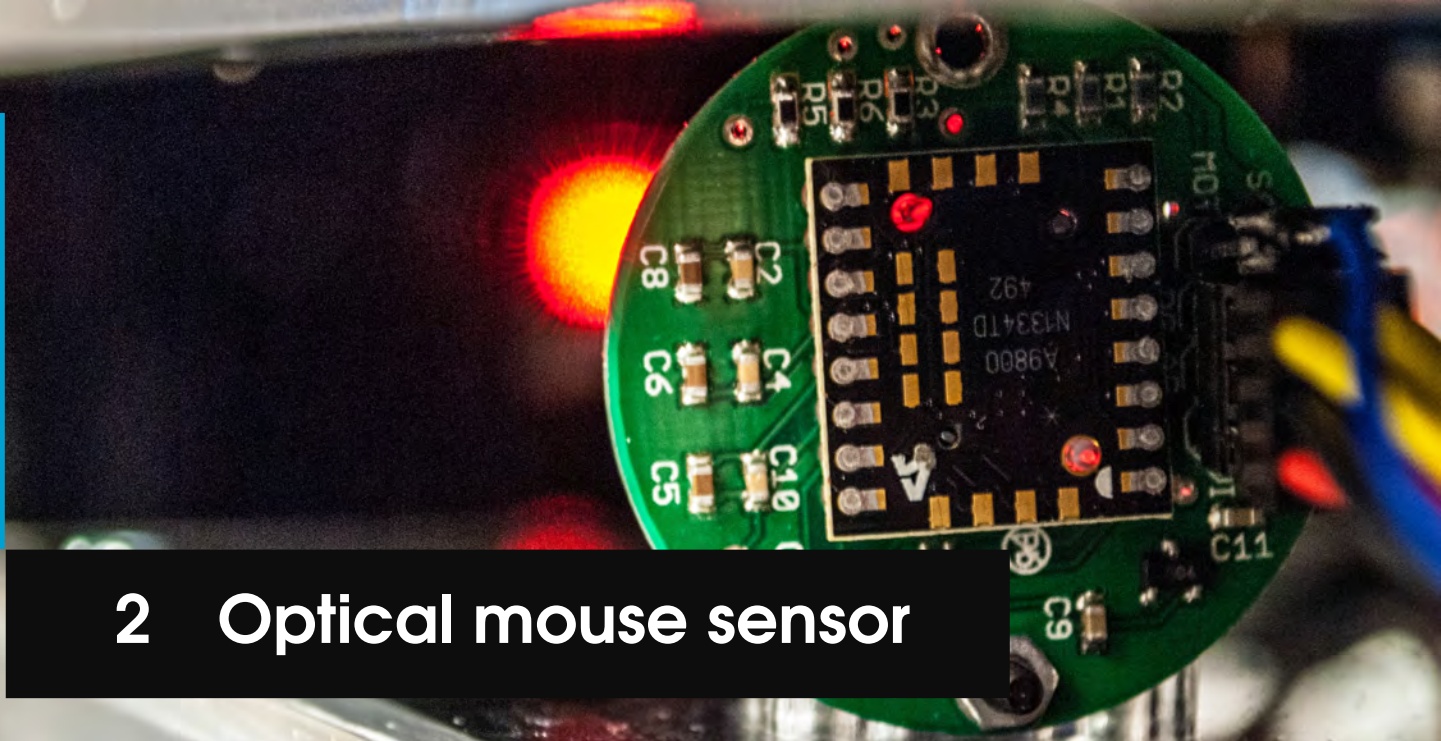
This thesis is divided into two parts, where the first part is about the design and validation of the sensor system. The second part is about the integration of this sensor in a planar stage system design.

Part 1: Sensor system design

Before the design of the system, the working principle needs to be discussed. This is done in the beginning of Chapter 2, followed by how optics can enhance the sensor's performance. In Chapter 3 the experimental setup to test the sensor system is presented, different performed tests are shown and the obtained results are discussed. These results are then interpreted and are used as design goals for the demonstrator stage.

Part 2: Planar stage system design

With the formulated sensor specification the process of pre-design is discussed in Chapter 4. Followed by the detailed design of the demonstrator stage in Chapter 5, discussing the different design choices of each part of the stage. The design and tuning of the controller are shown in Chapter 6, and the results of the finalized stage are discussed in Chapter 7. As last, the conclusion and recommendations are discussed in Chapter 8.



2 Optical mouse sensor

The optical mouse sensor is a mass produced sensor system and can be found on almost any desk. But how do they work, what are the key performances, and are they usable in precision motion control systems? These questions are answered in this chapter.

2.1 Working principle

Optical mouse sensors usually consist of several components, which are shown in Fig. 2.1. The light source, usually a laser or LED, illuminates the surface. The light emitted from the light source reflects diffuse in all directions from the surface. Light which goes through the plastic molded lens, is projected on the photo-diodes array and creates an image which can be seen by the sensor.

The most important part of the sensor is the photodiode array (PDA). These photodiodes conduct a photocurrent proportional to the received irradiance of the projected image. Figure 2.2, shows this sensor with a 400 times magnifications. The individual photodiodes can be seen with a size of $15\mu\text{m}$ and a pitch of $75\mu\text{m}$. This figure was obtained by opening the sensor packaging of one of the broken optical mouse sensors.

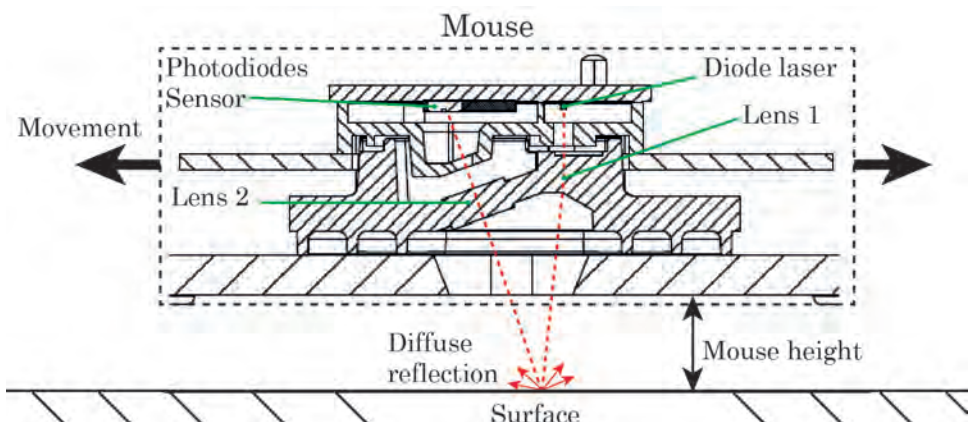


Figure 2.1: Cross section of the ADNS 9800 optical laser mouse sensor. The laserdiode emits a laser through the first lens which focuses the laser beam. The laser beam hits the surface and diffusely reflects to all directions. Some of the scattered light will go through lens 2 and will be projected on the sensor consisting of 30 by 30 photodiodes. This diffuse reflection contains information of the surface which can be observed by the surface. The optimal mouse height is specified as 2.4mm in the datasheet. Figure is taken from the datasheet in Appendix B.1.

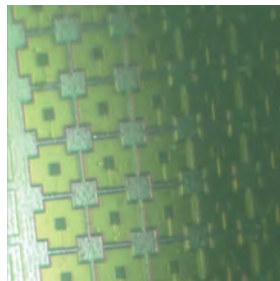


Figure 2.2: A 400 times magnification of the photodiode array of the ADNS 9800 optical mouse sensor. The individual photodiodes can be seen with a size of about $15\mu\text{m}$ and a spacing of $75\mu\text{m}$.

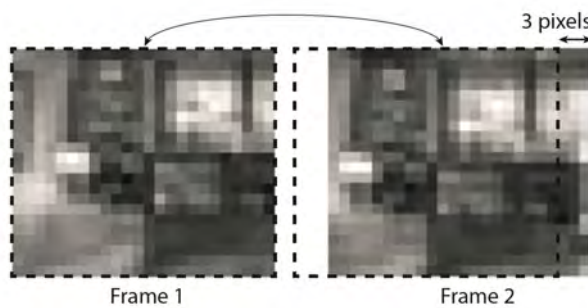


Figure 2.3: The mouse sensor compares different frames with each other to determine how much the mouse has moved. By taking a closer look the pattern can be recognized and a shift of 3 pixels can be observed. The sensor uses digital image correlation to do this at 12kHz. This figure is taken from [8].

The chip receives all the signals and uses digital image correlation (DIC) to compare the patterns from different frames to calculate how much the object has moved[8]. In most optical mouse sensors the resolution can be improved with interpolation to achieve sub-pixel resolution. The basics of the correlation technique is shown in Fig.2.3.

The optical mouse sensor can perform the process of taking pictures and using digital image correlation at a speed of 12kHz. This speed is mainly being limited by the exposure time on the photodiodes to acquire an image with enough surface details. This means that an adequate irradiance on the sensor is required to have a high frame rate, thereby having a sensor capable of tracking high speed movements.

2.1.1 Measuring surface

The performance of the optical mouse sensor is limited by the quality of the measurement surface it is looking at. A simple experiment to verify this, is to put a mouse on a glass table, most mouse devices will perform considerably worse.

For a high precision, the sensor needs to be reproducible. This means that an uniform material is preferred, such that the sensitivity of the sensor is not influenced by local patterns, thus a position independent sensitivity. The sensitivity is defined as the amount of incremental displacements counts of the optical mouse sensor per traveled distance.

The sensor needs high surface details in its field of view to detect motion. Which means that a rough surface is required. Which is quite obvious when two extremes are compared in Fig.2.4.

Another benefit of surface roughness is that it is more efficient in diffuse reflection.

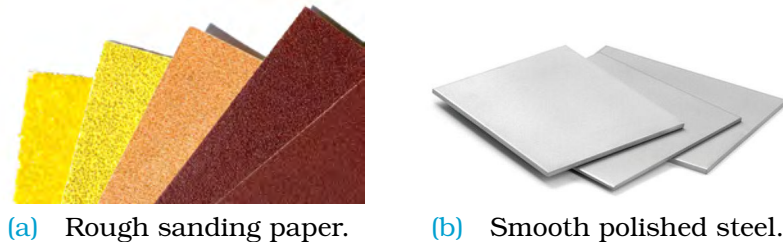


Figure 2.4: Two extreme examples demonstrate that high surface roughness gives more distinguishable surface details than smooth surfaces, it's even visible to the naked eye.

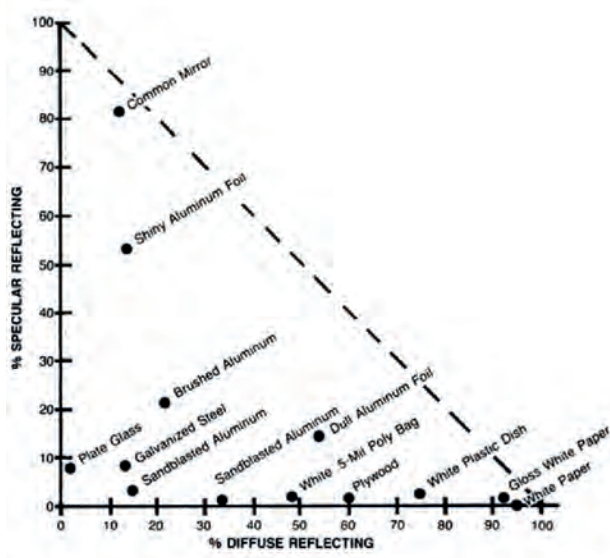


Figure 2.5: This figure shows the reflective properties of different materials. From the selected materials white paper has the highest efficiency ,95%, in diffuse reflection. This figure is taken from [9].

To get a high irradiance on the sensor, a material with Lambertian reflection or ideal diffuse reflection is desired. This means that all incident light is diffusely reflected back and no light is absorbed or specular reflected[9]. Figure 2.5 shows different materials and their reflection. From the selected materials in the figure, white paper has the highest efficiency in diffuse reflection. This is in line with the findings in a publication where the optical mouse performance was tested on measurement surfaces of different materials[10]. Ordinary white paper as measuring surface had the high sensitivity and repeatability.

However paper is sensitive for moist and other external influences. Alumina, a polycrystalline ceramic made from fine powder Al_2O_3 , has a high diffuse reflection efficiency too[11]. Both materials are compared with an experiment setup, which will be discussed in Chapter 3.

2.1.2 Mouse sensor as position sensor

For a position sensor, an absolute position signal is preferred. However, as discussed in the previous section, mouse sensors measure the displacement between frames. These displacements can be summed or integrated to get the position. However, small errors in the displacement are integrated into position errors, these errors accumulate over the distance which is traveled. Consequently, the position must be periodically corrected by for example resetting the sensor on a predefined position, before continuing with the measurement.

2.2 Chip selection

There are hundreds of different optical mouse chips available all with different characteristics. This research is about high precision position sensors, so the most important criteria is resolution. Framerate, maximum speed and accelerations are also important for high dynamic performance. Last but not least, the chip needs to be commercially available and easy to use.

2.2.1 ADNS 9800

With some market research, the ADNS 9800 was selected. The ADNS 9800 is an infrared laser mouse sensor chip with a PDA consisting of 30 by 30 photodiodes and a native resolution of 1600 counts per inch (CPI), or $15.8\mu\text{m}$. This resolution can be enhanced to 8200 CPI, or $3.1\mu\text{m}$ with interpixel interpolation. This resolution value was the highest of all commercial available sensors at the time of the market research.

Another advantage of this sensor was that it was sold as a module, where it was assembled with all peripheral electronics included on a PCB. Via the Serial Peripheral Interface (SPI) communication protocol, the sensor can be read out, with a microcontroller.

Moreover, the mouse has high tolerable acceleration and speed compared to other mouse sensors. The key performance characteristics are shown in table 2.1. A reduced datasheet of the optical mouse sensor is shown in Appendix B.1.

Table 2.1: Important performance characteristics on the ADNS 9800, according to the specifications of the manufacturer.

Resolution	$3.1\ \mu\text{m}$
Speed	3.8 m/s
Acceleration	$300\ \text{m/s}^2$
Framerate	12 kHz

2.3 Optical magnification

This resolution of $3.1\mu\text{m}$ is impressive for an ordinary mouse but not good enough for micrometer positioning. A new concept to increase the resolution, which has not been discussed in literature before, is to magnify the image of the measurement surface which is projected on the PDA with the use of an extra lens.

2.3.1 Geometric optics

A positive lens, also known as biconvex lens, can be used to make a larger image of an object. This is also known as magnification and this principle is used in for example common magnifying glasses. A schematic drawing can be seen in Fig.2.6.

The relation between S_1 and S_2 is determined by the focal distance f , following a simple relation that can be derived by trigonometry. This relation is called the Gaussian lens formula [12],

$$\frac{1}{S_1} + \frac{1}{S_2} = \frac{1}{f} \quad (2.1)$$

The magnification is determined by the distance between the lens and the object S_1 and the distance between the lens and sensor S_2 .

$$M = -\frac{S_1}{S_2} \quad (2.2)$$

The minus sign represents the image location at the opposite side of the optical axis as the location of the object.

2.3.2 Optical path length

Equation 2.1 and 2.2 can be rewritten to give the optical path length

$$S_1 = \frac{f(1+M)}{M} \quad (2.3)$$

$$S_2 = f(1+M) \quad (2.4)$$

$$l = S_1 + S_2 = f \left(2 + \frac{1}{M} + M \right) \quad (2.5)$$

In this form it can be seen that the length of the optical path increases with increasing focal distance and magnification. For ease of alignment and rejection of variation in

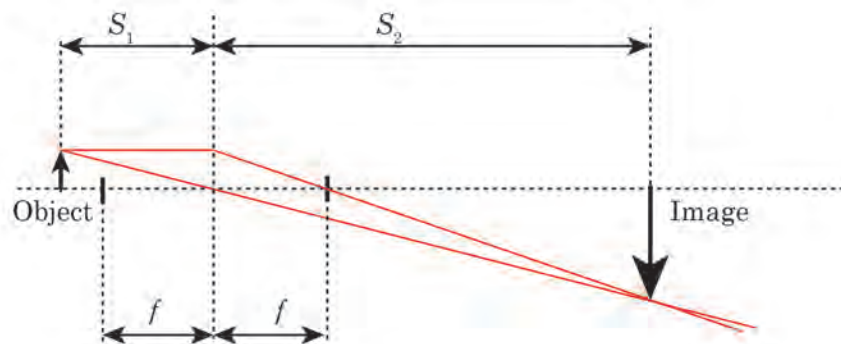


Figure 2.6: A positive lens can be used to magnify an object, the magnification is the ratio of S_1 over S_2 . f is the focal length of the lens

sensitivity, high focal lengths are desired. Since small variations in the optical path lengths will induce a change in magnification, thus a change in sensitivity.

$$M = \frac{S_1 + \epsilon_1}{S_2 + \epsilon_2} \quad (2.6)$$

This relation shows that $\delta M \propto S/\epsilon$, resulting in a trade-off between ease of alignment and error rejection, and compactness.

2.3.3 Irradiance on the sensor

The irradiance on the sensor should be high enough as mentioned in Section 2.1. The downside of magnification is that the irradiance decreases quadratically with the magnification factor. This is due to the fact that the same light is spread over a larger area, while only a part of the image is on the detector, see Fig.2.8a.

This can be solved several ways, adding a more powerful laser source, choosing a measurement surface with a higher diffuse reflection efficiency or by changing the size and distance of the lens.

When picking an external laser the wavelength should be matched with the spectral sensitivity of the sensor (how efficient the sensor detects a certain wavelength), see Fig.2.7. The peak sensitivity of the sensor is at 830nm, which is infrared light and dangerous to work with. Therefore, a 630nm (red) is selected with a spectral sensitivity of 90%. The laser spot can be used more effectively when another lens is used to focus the laser spot on the measurement surface. The light is then concentrated on a smaller area, which has the inverse effect of magnifying.

Fig.2.8b. Lenses which are larger and closer to the object catch more light. However, when moving the lens closer to the object, the distance S_1 decreases. To obtain the same magnification, the focal distance f of the lens needs decrease as well. When picking a lens there is a trade-off between diameter and focal distance.

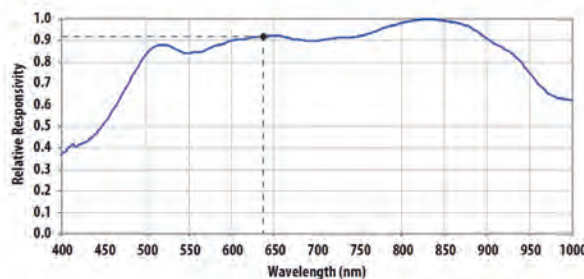
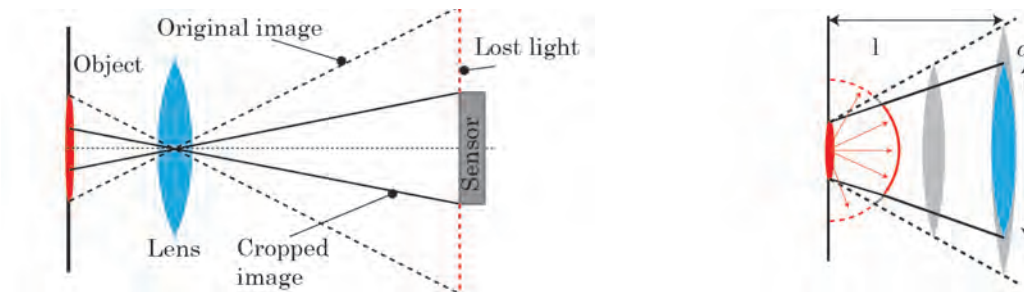


Figure 2.7: The spectral sensitivity of the sensor. The sensor has a peak sensitivity at 830nm which is infrared light. Infrared laser sources are dangerous to work with, because infrared light is invisible to the human eye, but still can cause damage. Therefore a laser with 630nm (red) is chosen, which still has about 90% of the efficiency of detection.



(a) When zooming in on an object with constant radiance, the light is spread over a larger area. Meaning that the irradiance, the incoming light intensity per unit area, decreases. Since the magnified image doesn't fit on the sensor, the total irradiance on the sensor will decrease.

(b) More light can be captured when either the lens diameter d is increased or when the distance between the object and lens S_1 is decreased.

Figure 2.8: Other ways to influence the irradiance on the detector.

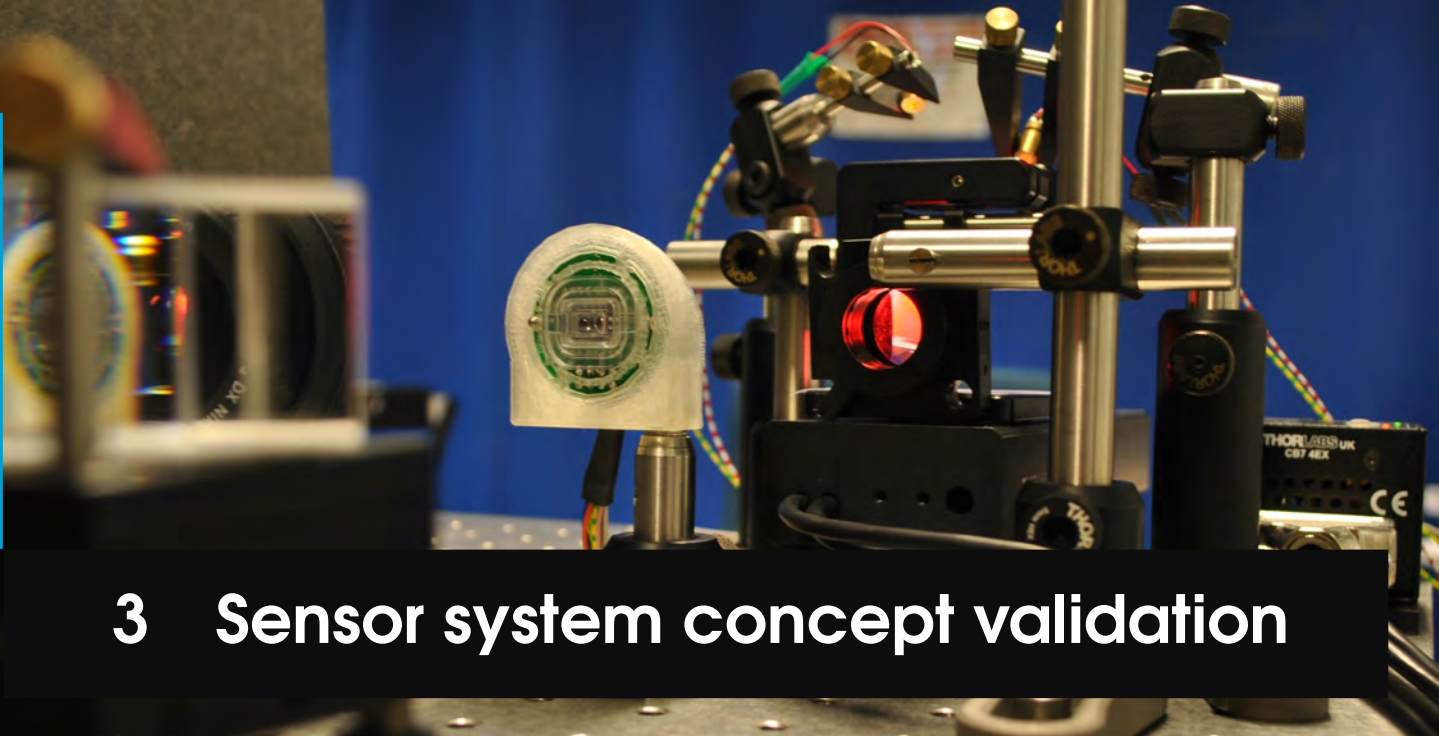
2.4 Conclusions

An optical mouse sensor compares different pictures with each other to determine the displacement. The position can be obtained by integrating these displacements. However, the integration will introduce an integration error, creating an error build-up. Periodically resetting the position signal is required to prevent large accumulation of integration error.

For high precision and sensitivity, the measuring surface, where the mouse is looking at, should be uniform, white and have a high surface roughness. White paper or ceramic alumina are potential candidates.

The ADNS 9800 optical mouse sensor, is selected for its high resolution. This resolution can be enhanced even more by using optical magnification to increase the image which is projected on the sensor. However, when using optical magnification, more light is required to reach the same irradiance on the sensor. By using a stronger laser, a larger lens or by moving the lens closer to the object, the irradiance on the sensor can be kept constant.





3 Sensor system concept validation

In this chapter the experimental setup to validate the sensor and magnification concept is shown. The results of these tests are discussed and the sensor specifications are derived. With these specifications it will become clear if the optical mouse sensor is suitable for precision positioning systems.

3.1 Experimental setup

The precision and resolution of the mouse as stand alone sensor and with the magnification concept needs to be tested. This can be tested by repeating the same relative displacement between the mouse and the measuring surface, while measuring with a reference sensor. This displacement needs to be repeatable and preferably follow certain dynamic profiles, so that the influence of acceleration and velocity on the precision of the measurement can be observed.

To fulfill these requirements, a motion controlled stage is required. The Thorlabs DDSM-100 stage is selected for the previous mentioned criteria. It has an accuracy of $0.5\mu\text{m}$, it is fast and the dynamic profiles can be configured. The specifications are shown in Appendix B.2.

The optical mouse sensor readout and the control of the Thorlabs stage were performed on an Arduino and in LabView respectively, data processing was done afterwards in MATLAB. The whole setup, electronics, software and data management had to be developed prior to the experiments.

3.1.1 Setup 1: Optimal settings

First the optimal mouse height, mouse software settings and measurement surface needs to be determined. This was done by mounting the mouse above the stage without any additional optics on a manual linear stage, see Fig.3.1. Different measurement surfaces were attached to the stage so that they could be compared. By manipulating this stage, different sensor heights could be compared. For this setup the default laser source of the mouse was used. The most important software settings which has an influence on the performance of the optical sensor are frame/shutter rate and interpolation factor, these were configured with the Arduino and could be compared with each other.

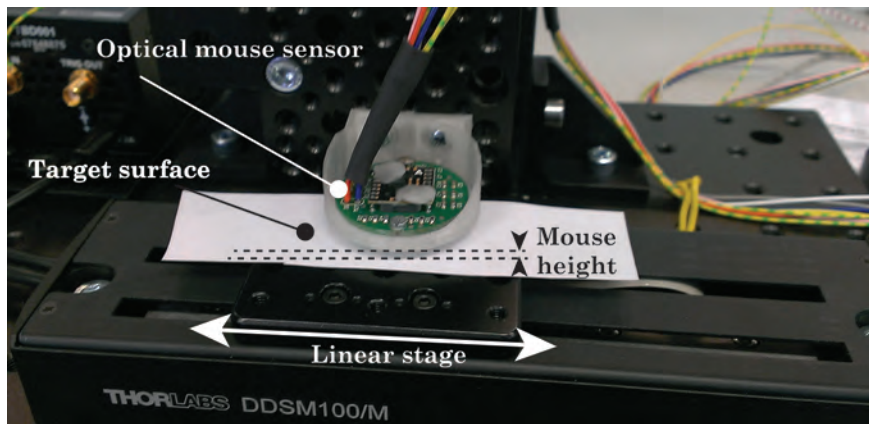


Figure 3.1: The mouse was mounted above the stage. Sensor height, target surface and mouse settings were adjusted to find the optimal settings

3.1.2 Setup 2: Higher resolution, magnification

After obtaining the optimal settings, the magnification concept can be validated. Another manual linear stage was placed between the mouse sensor and the stage, a lens with a focal length of 20mm was placed in between. An external laser with a wavelength of 630nm was used to illuminate the surface target. The magnification was increased by manipulating the distances between the surface and the lens and the lens with the sensor, as described in section 2.3.1. The setup is shown in Fig.3.2

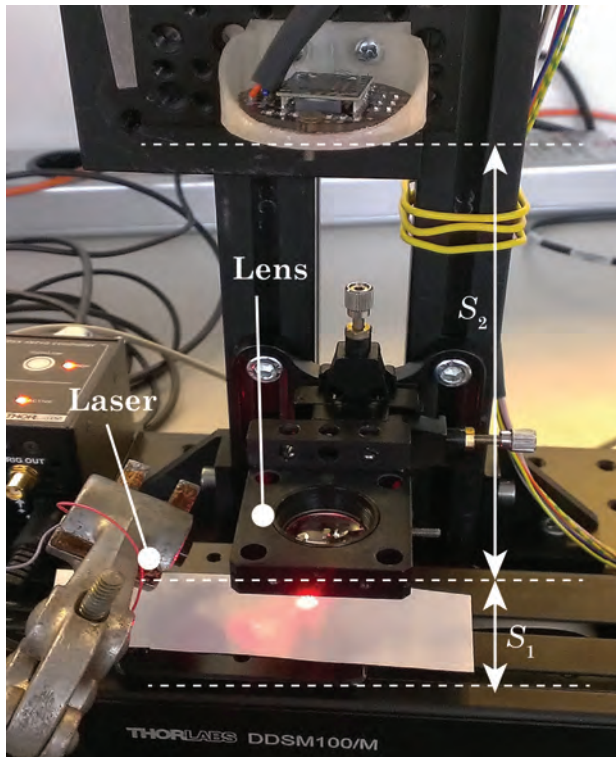


Figure 3.2: An extra lens was added between the sensor and the target surface. An additional laser was required to illuminate the target surface. By changing the location of the sensor and the lens the magnification can be adjusted.

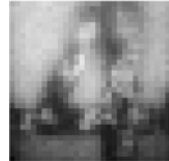


Figure 3.3: By outputting the current frame of the as gray values the quality of focus and alignment can be found, this frame is of a printed "4" on white paper

The quality of focus and alignment was found by letting the mouse output its current frame in grey values per pixel and visualized as a 30 by 30 figure, see Fig.3.3. With this figure it is possible to "see" what the mouse sensor is "looking" at and to check the optical alignment such as focus and illumination. This visual feedback method shortened the time to align all the optical elements.

3.1.3 Setup 3: Folding the optical path

Setup 2 gets bigger with increasing magnification. Therefore, it was tested if the optical path can be made more compact by using mirrors. The setup was rebuild by placing a mirror very close to the measurement surface, to reflect the optical path horizontally for easier alignment. Then another mirror was placed halfway to fold the optical path. This setup is shown in Fig.3.4 and proved that mirrors can be used to get a more compact optical design.

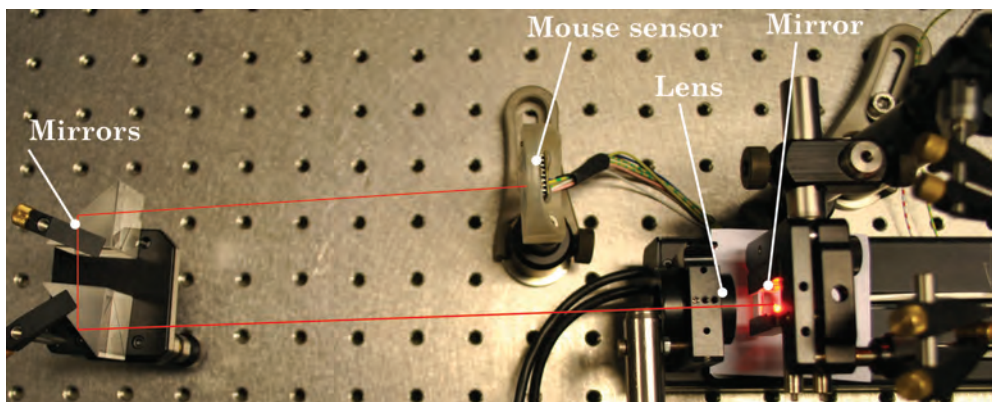


Figure 3.4: Third setup, a mirror was placed very close to the target surface, to reflect the optical path horizontally for easier alignment and a mirror halfway to fold the optical path.

3.1.4 Measurement method

For all the different setups the same measurement method was used. A large data set was obtained by performing the same stepping sequence for multiple time, 5 of these steps are shown in Fig.3.5a. The sensitivity was determined by averaging the measured incremental mouse counts divided by the measured displacement of the encoder. The mouse signal was then divided by this sensitivity value to obtain the position information. The measurement error is determined by taking the difference between the reference encoder position signal and the optical mouse position signal at the end of each step, this error is visualized in a scatter plot in Fig. 3.5b.

Normal distribution

The normal distribution is a good way to represent the random drift which is observed in the measurement error. The repeatability of the optical mouse sensor or in other

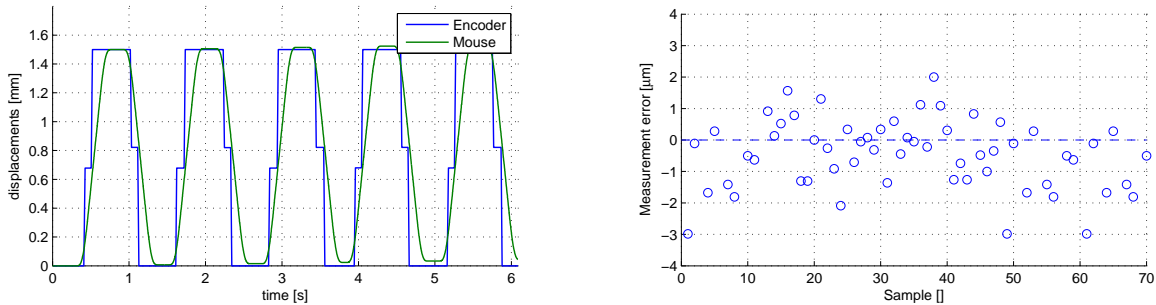
words the measurement precision can be expressed with the standard deviation σ ,

$$\sigma = \left(\frac{1}{n-1} \sum_{i=1}^n (x_i - \bar{x})^2 \right)^{\frac{1}{2}} \quad (3.1)$$

where \bar{x} is the average of the error, in these measurements the average is used to determine the sensitivity. This means that \bar{x} is always zero and no information about the accuracy can be determined.

These measurement errors are also plotted in a normalized probability density function (PDF), see Fig.3.6a. The red line is the contour of a standard normal distribution with a corresponding average and σ .

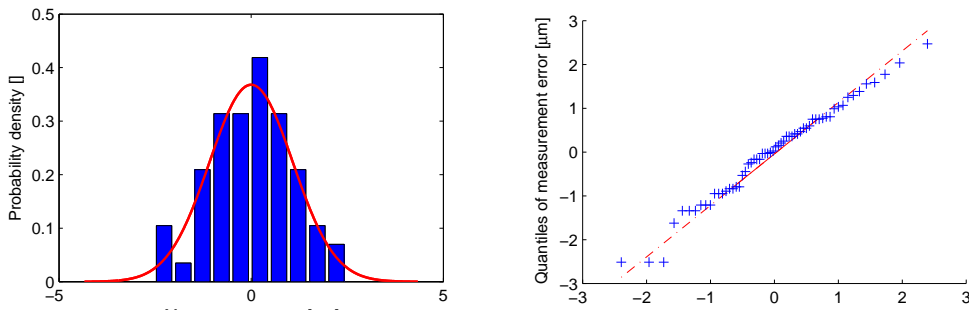
Another way to visualize this is with a Q-Q plot, see Fig. 3.6b. The plot is obtained by comparing the points in the PDF of the measured position error with the same points on the PDF of a standard normal distribution. The position error of these points are plotted on the Y-axis and the value of the standard normal distribution is plotted on the X-axis. Resulting in a straight linear line when the distributions match, while the slope tells something about the difference in σ .



(a) Blue is the reference encoder, due to the low read out rate the position profile looks strange and only the steady state position can be used. Green is the optical mouse sensor.

(b) The measurement error at then end of each step can be visualized with a scatter plot.

Figure 3.5: The displacement is repeated for multiple times so that the repeatability of the measurement system can be determined, thus the measurement precision.



(a) Probability density function of the measurement error, the red line is the contour of a normal distribution

(b) QQ-plot of the measurement error. The line is straight which means that the measurement error is normally distributed

Figure 3.6: The measurement error is normally distributed

Table 3.1: The mouse settings determined from the first setup are used in all experiments

Settings	Values	Comment
Sensor Height	2.4mm	as specified in the datasheet
Framerate	12kHz	highest setting
Resolution	8200DPI or $3.1\mu\text{m}$	highest setting
Surface	Alumina ceramic	same performance as white paper

3.2 Results

The optimal settings are determined and are shown in Table 3.1. The sensor has a depth of focus of 0.22mm around the average sensor height of 2.4mm according to the specifications. By configuring the mouse in the middle of its depth of focus seems to have a slightly better performance. Highest framerate and resolution settings proved to increase the measurement precision too. The ceramic alumina is selected as material for the measurement surface, because it doesn't suffer from moist and other external influences, while having the same performance.

3.2.1 Measurement sensitivity and precision

To determine the measurement sensitivity and precision, different displacements varying from $100\mu\text{m}$ to 2mm were repeated. From these steps the standard deviation of the measurement error is determined and is shown in Fig.3.7. The σ measurement error is approximately $2\mu\text{m}$, plus an additional linear error of $4.5\mu\text{m}$ per traveled mm. All displacements are performed with a speed of 10mm/s and an acceleration of 100mm/s². At a first glance, these results are not bad and already better than the $65\mu\text{m}$ resolution which was achieved in literature[2].

In figure 3.8 the blue line shows the sensitivity of the optical mouse sensor. Smaller movements seems to have a decreasing sensitivity with decreasing displacements. On the other hand, larger displacements seems to be more constant. This behavior is extremely unwanted in a position sensor. A hypothesis for this behavior could be that the mouse has some sort of noise rejection filter. While the mouse is standing still, the mouse sensor should not drift. Therefore, it could be that the sensor requires a displacement larger than a certain threshold, before registering it as a movement. Due to the scope of this project, this is not investigated further.

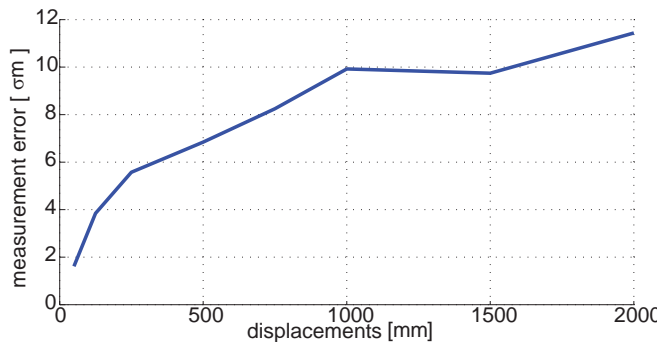


Figure 3.7: The figure shows the standard deviation of the measurement error of the mouse sensor when performing different step sizes, ranging from $2\mu\text{m}$ at small displacement steps to almost $12\mu\text{m}$ at a displacement of 2mm. Each data point consist of 100 samples. The value for the error at 1mm seems a bit too high, since it not in line with the other points. All displacements are performed at 10mm/s and 100mm/s².

3.2.2 The effects of magnification

Besides increasing resolution and precision, magnification is also used to eliminate the non-constant sensor sensitivity. This is due to the fact that the mouse "sees" a magnified displacement. For example, movements of $100\mu\text{m}$ seems to be 1mm at a magnification of $10\times$. This eliminates the non-constant sensitivity problem, which is shown as the green line in Fig.3.8.

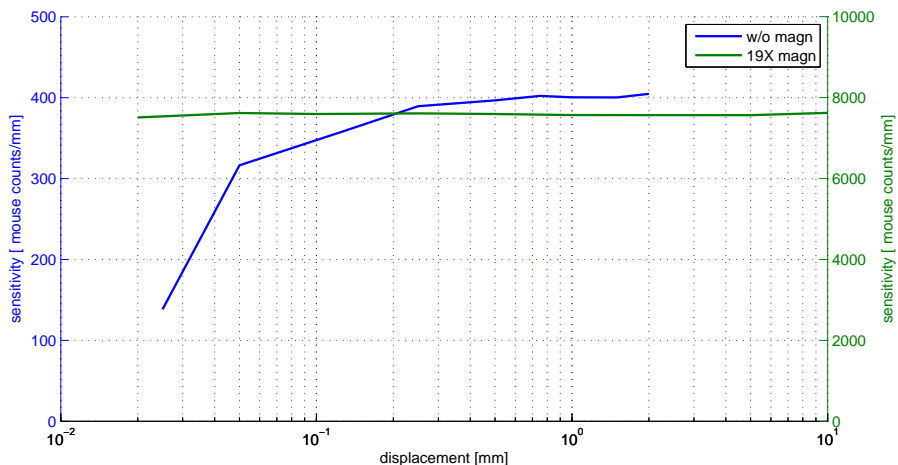


Figure 3.8: This figure shows the sensor sensitivity (incremental sensor counts per traveled distance). Blue is the unmagnified optical mouse sensor sensitivity and it shows that the sensitivity decreases with smaller displacements. With larger displacements the sensitivity stays more constant. The green line is the sensitivity of the optical mouse sensor with $19\times$ optical magnification. It shows that the sensitivity is raised by a factor $19\times$ and that sensitivity is constant, even for smaller steps. Note that the green line should be read out with the right axis

Another benefit of magnification is the increase in precision. This is shown in Fig.3.9, the standard deviation of the measurement error is decreasing with increasing magnification. The tests went till a magnification factor of $19\times$, where the standard deviation of the measurement error is approximately $0.6\mu\text{m}$ per traveled mm plus a constant uncertainty of $0.3\mu\text{m}$. Giving for a 1mm displacement a 3σ precision of $2.7\mu\text{m}$.

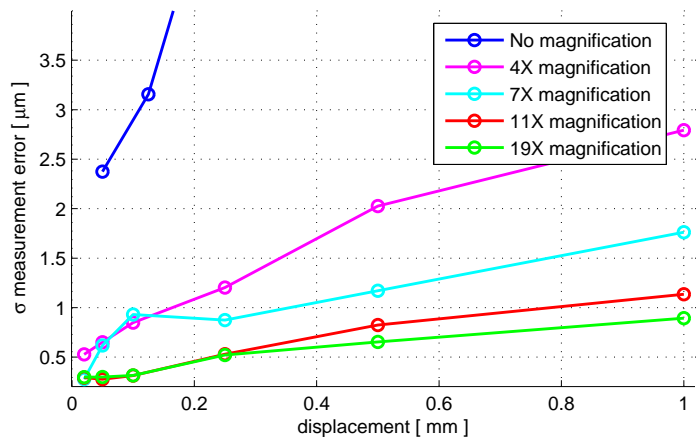


Figure 3.9: This figure shows the standard deviation of the measurement error, with different magnifications and different displacement steps. It shows that the precision of the sensor increases with higher magnification and that the measurement uncertainty increases with larger displacements, which is logical because measurement errors are integrated.

3.2.3 Velocity and acceleration limitation

The downside of magnification is that the speeds and accelerations the sensor senses increases proportional with the magnification factor. To determine the maximum velocity and acceleration to reach the presented results, the velocity and acceleration are increased till an decrease in precision could be observed. With a velocity of 30mm/s and an acceleration of 500mm/s² the precision started to deteriorate. This is considerably less than the specifications (200mm/s 1500mm/s², including magnification) of the manufacturer.

3.2.4 Sensitivity over full stroke

Up till now, the tests were all done from the same starting positions, thus the same trajectory. In a positioning system the sensor should be able to have the same sensitivity over the full stroke. This is simulated by starting from different starting location, the mouse will sens a different trajectory. This gave a sensitivity spread of 0.25% which is in the same order of measurement uncertainty as starting from the same location.

3.2.5 Error build-up

The region of interest (ROI) tracking capabilities of this sensor system is also validated. This is done by manually ordering the stage to move forth and back with a predefined maximum velocity and acceleration. The measurement error between the encoder and the mouse sensor is then divided by the total traveled distance. This gave an error build-up of less than 0.1% of the traveled distance.

3.2.6 Sensor delay

Due to the fact that the encoder read out was so low, only the steady state values were compared. The assumption was made that with a 12kHz frame rate, the mouse sensor should be fast enough. However, at a later stadium when the demonstrator stage was finished severe dynamic problems were found such as heavy digital filtering in the mouse sensor. This will be discussed in detail in Section 6.2.

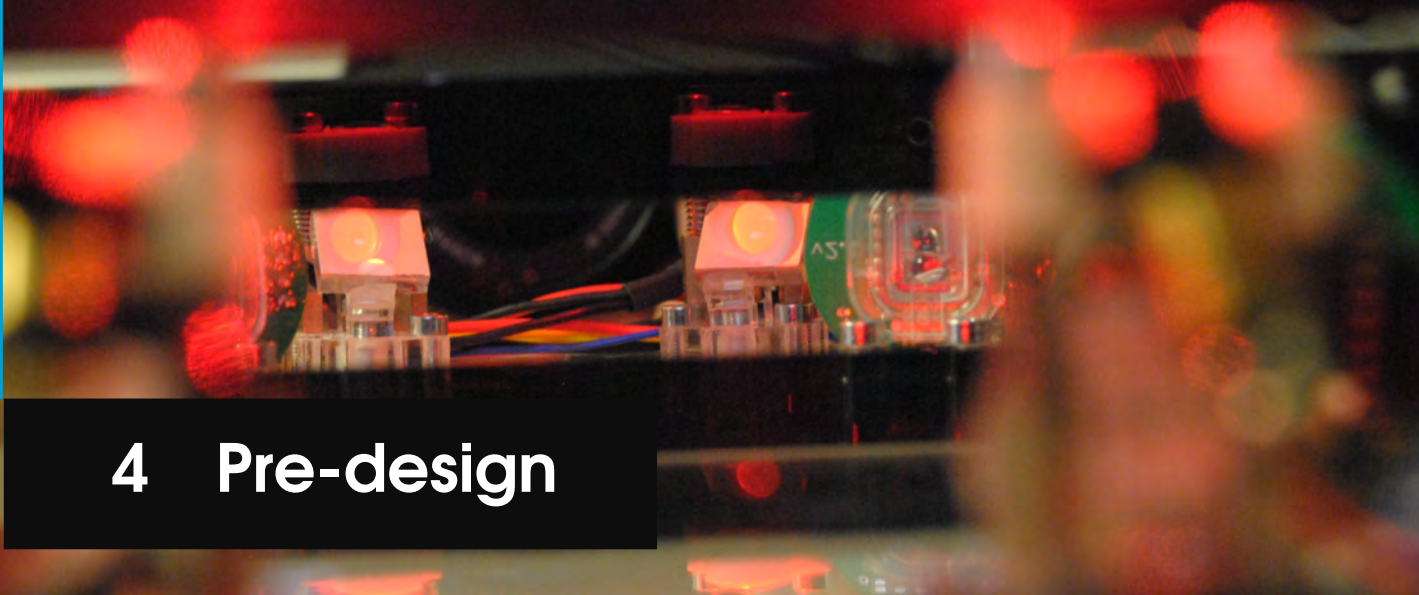
3.3 Conclusions

The non-constant sensitivity as function of the displacement can be removed by introducing optical magnification. With an experiment setup it has been validated that the concept works and that it indeed makes the sensitivity constant. Additionally, the optical magnification improves the measured resolution from $2.5\mu\text{m}$ to $0.13\mu\text{m}$.

Drift is present in the optical mouse sensor. By resetting this drift before every step and using the optical magnification concept, the 3σ measurement repeatability on a 1mm step can be reduced to $2.7\mu\text{m}$, meaning that 99.7% of the measurements fall between $\pm 2.7 \mu\text{m}$ of the 1mm.

The optical magnification also has a downside, since it decreases the maximum tracking velocity and accelerations to 30mm/s and 500mm/s².

Reflecting back on the thesis goals, the first part can be answered now. Optical mouse sensors can be used as position sensors, but will not perform well. Unless the above mentioned methods are used to enhance their performance to the required performance for precision positioning.



4 Pre-design

Before starting with designing, it is important to know what we want to build. This is done by defining the requirements of the stage and the design goals. At last a conceptual overview of the demonstrator is shown.

4.1 Requirements

The goal of this thesis is to design and build a planar stage system with low cost components. The sensor system concept has just been validated, now the rest of the system can be discussed.

The validated optical mouse sensors have a specification which are in the same order of magnitude as the other microscope stages found during the market research. To get the maximum performance out of the system, the rest of the planar stage system should be slightly over-designed, to make sure that the validated specifications of the optical mouse sensor can be met. The requirements are shown in Table 4.1.

The other requirements, such as payload and stroke, are based on microscope applications like blood cell or chip inspection.

Table 4.1: Requirements of the planar stage system for microscope applications, based on the experiments performed with the mouse sensor.

Requirement	value
Payload	20g
Stroke	10 x 10mm ²
Speed	30mm/s
Acceleration	500mm/s ²
Resolution	< 0.2µm
Accuracy	< 10µm (1mm step)
Precision (3σ)	< 5µm (1mm step)
Settling time	< 1s (1mm step)
Rotational precision (3σ)	< 0.1°
Control bandwidth	10Hz
Component costs	< €300,-

4.1.1 Bandwidth and error rejection

A high bandwidth is required to suppress external vibrations and for fast positioning. According to a measurement of floor vibrations which has been conducted in the mechatronics lab[14], the largest amplitude is 2.2mm/s^2 with a frequency of 10Hz. The requirement for positioning precision is set at $5\mu\text{m}$. This means that the control stiffness needs to be at least 44N/m . Resulting in a bandwidth of

$$\omega_c = \sqrt{\frac{k}{m}} = 20.7\text{rad/s} = 3.3\text{Hz} \quad (4.1)$$

As a safety factor and for a faster step response, a control bandwidth of 10Hz is set as target. The hardware components of the planar stage system will be over-designed for a control bandwidth of at least 100Hz. With this higher bandwidth the planar stage system will not limit the optical mouse sensor performance, so that the full potential of this system can be shown. Additionally, it adds the possibility to be re-used for future projects.

4.1.2 Additional design goals

Additional design goals are added since the system is a demonstrator:

- **Adjustability** is important, so that different configurations can be tested and so that parts can be aligned when components are produced with low tolerances.
- **Amount of parts**, leads to less parts that needs to be aligned, decreases the time to assemble and decreases the component cost.
- **Should be produced in-house**, reducing production costs, no dependencies on manufacturers and enables quick iterations between design and production.
- **Cost effective software and electronics**, the goal to design a cost effective system also applies on the lab equipment. Therefore, a simple cost effective Arduino is used to control the stage. Open-source software is used to communicate and the whole system is fed with a standard 12V DC voltage supply.

4.2 Conceptual overview of all subsystems

Figure 4.1 shows a conceptual components placing. The most important part is the sensing location and is placed directly in line with the field of view of the microscope to reduce error. For a compact design the optical path is "folded" with mirrors. Actuators are required to actuate the mover which is suspended on bearings with a high height stiffness, so that the distance between the lens and target surface doesn't change. This is required to keep a constant magnification, thus a constant sensor sensitivity, as described in Section 2.3.1.

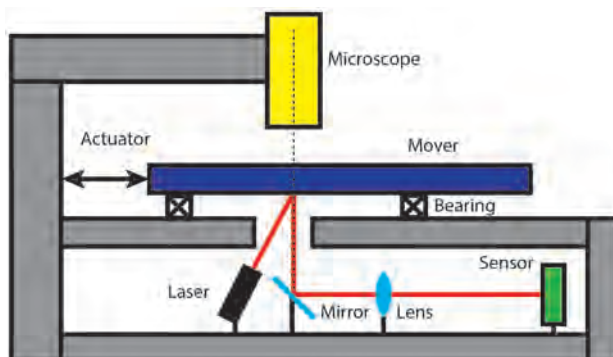
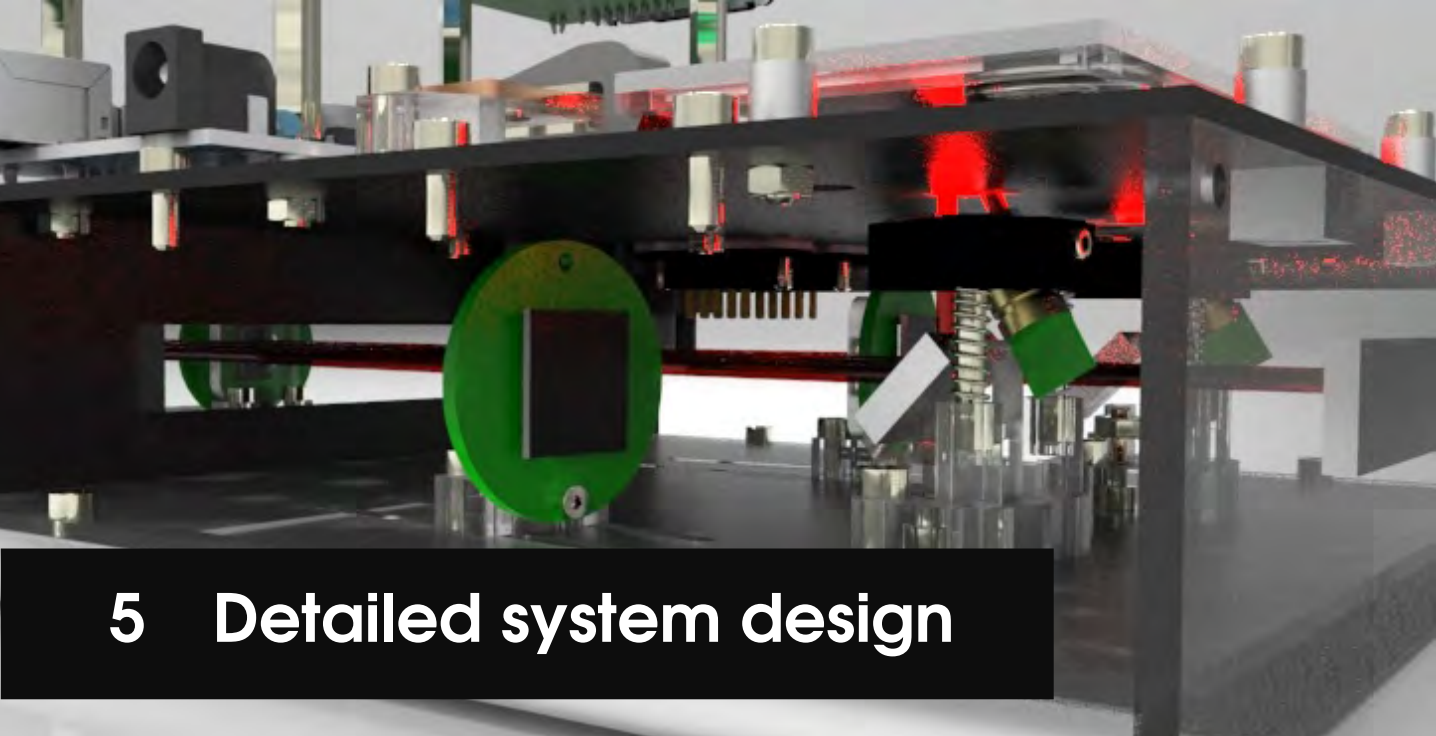


Figure 4.1: Schematic overview of the concept of the planar stage. The mouse sensors placed in line with the microscope to reduce error. Mirrors are used to fold the optical path for a compact design. The amplifiers, electronics and control systems are not visualized, but are designed.



5 Detailed system design

The design of the stage system was a parallel process with various iterations between all the different sub-systems, this is required to obtain a comprehensive system design where all sub-systems work in conformity. For readability the design is presented per sub-system beginning with the sensors and the optics. Followed by the actuator and the amplifier. At last the design of the mover is shown.

5.1 Optics and sensors

This section shows how the selected and validated ADNS 9800 optical mouse sensor with the optical magnification concept has been implemented in the planar stage system design.

5.1.1 Sensor placement

The optical mouse sensor is placed below the mover directly in line with the field of view of the microscope, to reduce the error. The sensor is "looking" at the bottom of the stage, measuring the in-plane(X,Y) movements. Adding another sensor adds the possibility to measure the rotation too, by taking the difference between the position signals of the mouse sensors as shown in Fig.5.1. A benefit is that the redundant x-coordinate can be used to reduce the error over this axis.

In order to have a high rotation sensitivity and a small rotation error due to sensor noise, the sensors needs to placed as far apart as possible. This distance between the sensors is the rotation arm. The maximum angle error due to sensor error can be described with,

$$\epsilon_\theta = \arcsin \left(\frac{\epsilon_y \cdot 2}{d} \right) \quad (5.1)$$

where ϵ_θ is the rotation measurement uncertainty, ϵ_y is the measurement error in y position of the sensors and the d is the distance between the sensors.

The two sensors do not have the same field of view, they are both looking at a different location on the measurement surface. In Section 3.2.4, this uncertainty was determined as 0.25% of the traveled distance. This results in a maximum rotation error of 0.05°, when the sensors are positioned 50mm apart from each other and a stroke of 10mm is made. This is lower than the requirement of 0.1°.

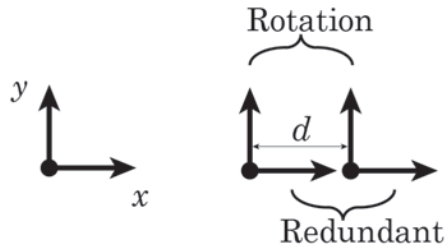


Figure 5.1: The number of mouse sensors to use in the system. With just one sensor only the x and y position can be measured. Adding another sensor makes it possible to observe and control the rotation. In the redundant axis this additional sensor makes it possible to reduce the error by combining the measurement of both sensors.

5.1.2 Reset error build-up

The optical mouse sensor is a relative displacement sensor, meaning that the position is obtained by integrating the displacement signal. This introduces an accumulation of integration error. During the experiments in Section 3.2.5 the error is reset by ordering the stage to go to home. In the planar stage, this home location has been designed.

The precision of such a homing system is mainly dependent on the ability to overcome the contact stiffness of the home contacts[15]. If one of the contact points sticks, self locking and hysteresis can occur. A schematic overview of all forces is shown in Fig. 5.2. The friction forces create a torque around the poles p_1 and p_2 , with these three forces it is always possible to get the mover in its zero position without hysteresis.

The forces of the resetting procedure are repeatable, meaning that the stiffness requirements for the contact points are not critical. The deformation, only if it is repeatable, will not reduce the precision, meaning that the contact points can be integrated with the endstops of the planar stage system.

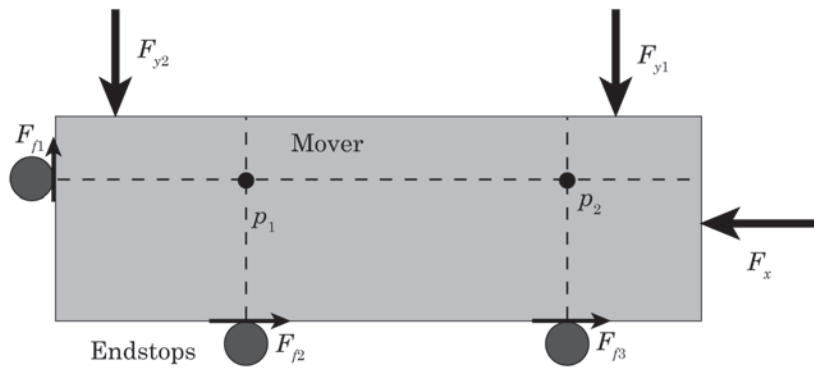


Figure 5.2: Schematic topview of the mover with the contact points of the home location. The actuation and friction forces are drawn. With these three actuation forces it is possible to overcome the torques of the friction forces. The contact stiffness is not critical, because the force for the homing procedure is repeatable, enabling the integration of the contact points with the endstops.

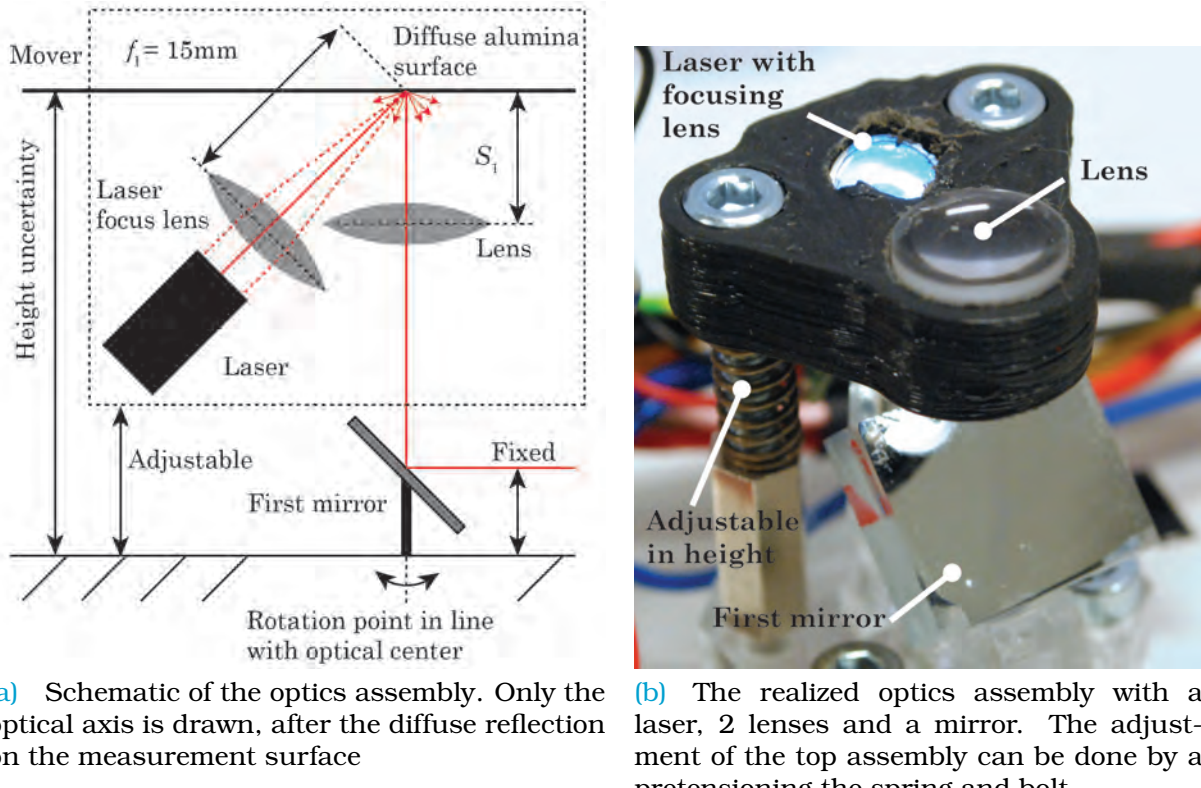
5.1.3 Optics assembly

Optics are used to illuminate the measurement surface and to magnify this image on the optical mouse sensor for a higher resolution and measurement precision.

The alignment of all these parts with respect to the measurement surface is critical, to have a constant magnification and a laserspot in the field of view of the mouse, see

Fig.5.3a. Therefore, they are all fixed on a frame with respect to each other. This frame needs to be adjustable in height, so that it can be aligned with the mover.

With these requirements, the optical assembly in Fig.5.3b has been designed. A 3D printed holder for the optical component which can be adjusted in height with a bolt with pretension. This frame is mounted on top of a platform which can rotate around the optical center so that rotations will not lead to parasitic translations. On this platform the first mirror is mounted to reflect the vertical beam horizontally. The height of this horizontal beam is fixed by the height of the sensor.



(a) Schematic of the optics assembly. Only the optical axis is drawn, after the diffuse reflection on the measurement surface

(b) The realized optics assembly with a laser, 2 lenses and a mirror. The adjustment of the top assembly can be done by a pretensioning the spring and bolt.

Figure 5.3: The laser, focusing lens and magnification lens needs to be fixed with respect to each other but adjustable in height, due to uncertainty in the height of the mover.

5.1.4 Sensors and mirrors

The optical magnification concept has been validated with a magnification factor of 19. The possibility to test even higher magnification is included in the design up to a magnification of $40\times$. The implemented magnification is only $16\times$, since only the potential of this system needs to be showed. Making alignment and the control system design (due to tougher velocity and acceleration limitations) easier.

A compact design has been realized by folding the long optical paths with a 4 mirror configuration as shown in Fig.5.4. The two shown configurations are just examples, other configurations can be obtained easily from the parametric CAD model. The blue and red lines are $16\times$ and $40\times$ magnification respectively. To change the magnification, the optical assembly (introduced in Fig.5.3b) has to change its angle, while the sensor location needs to be changed completely.

This alignment is solved by having multiple laser cut base plates with each their own magnification configuration. For easy interchanging of base plates and easy alignment,

the complete optics compartment can be removed from the stage system with only 4 bolts. Giving full access to all optical parts while keeping the alignment intact. Methods used to align the optical components are shown in Appendix A.3.

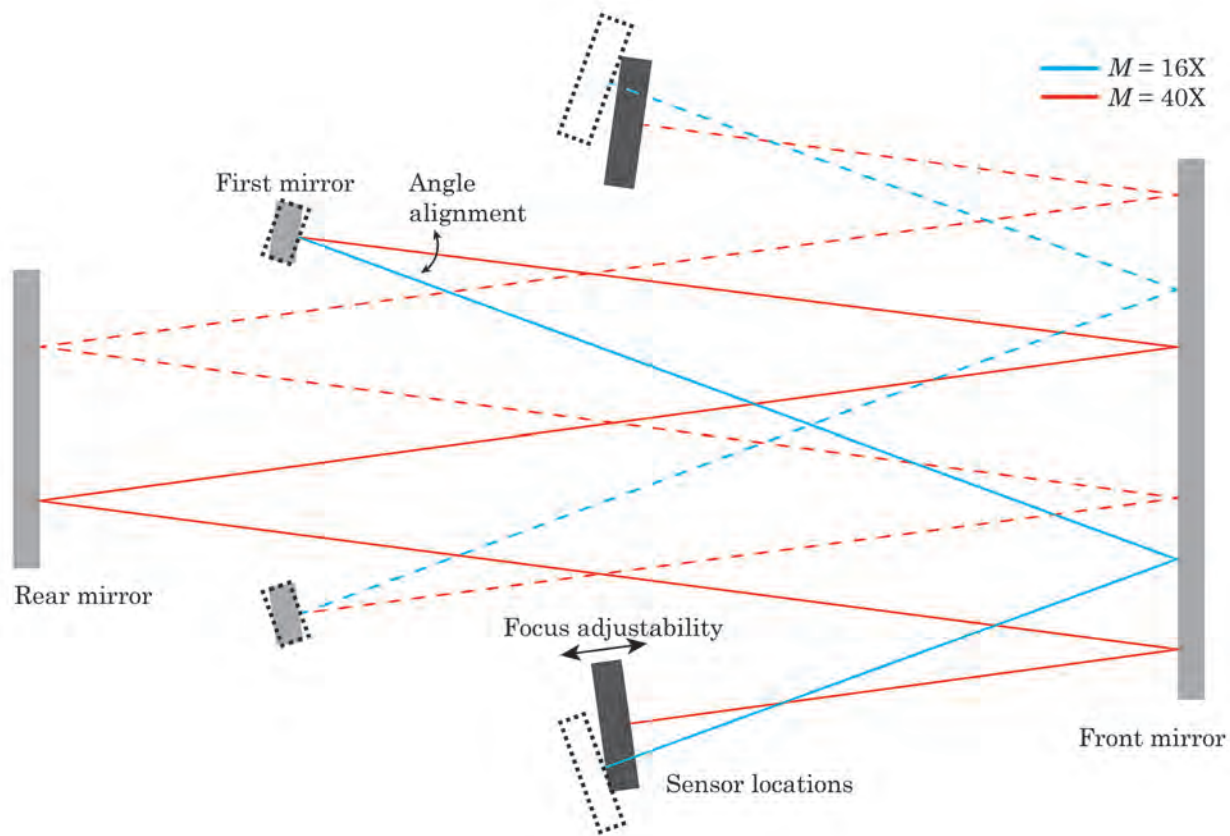


Figure 5.4: Topview of the optical path, the blue and red lines are 16 and 40 times magnifications respectively. The dashed lines represent the optical paths for the second sensor. The front and rear mirrors are fixed, the "first mirror" and sensors can be adjusted and are used for alignment.

The front and rear mirror are fixed and are attached to the container wall. The sensors and the first mirror are used for aligning and focusing. The rotation axis of this optics assembly coincide with the optical axis of the vertical reflected beam, making sure that the rotations do not introduce a translation for the horizontal beam.

This results in a compact and adjustable optical compartment with low parts count. Figure 5.5 shows a visualization of the design, the parameters of the optical path are shown in Table 5.1.

Table 5.1: The parameters of the optical path

Parameters	$M=16\times$	$M=40\times$
f	12mm	12mm
f_l	15mm	15mm
S_1	12.75mm	12.3mm
S_2	204mm	492mm

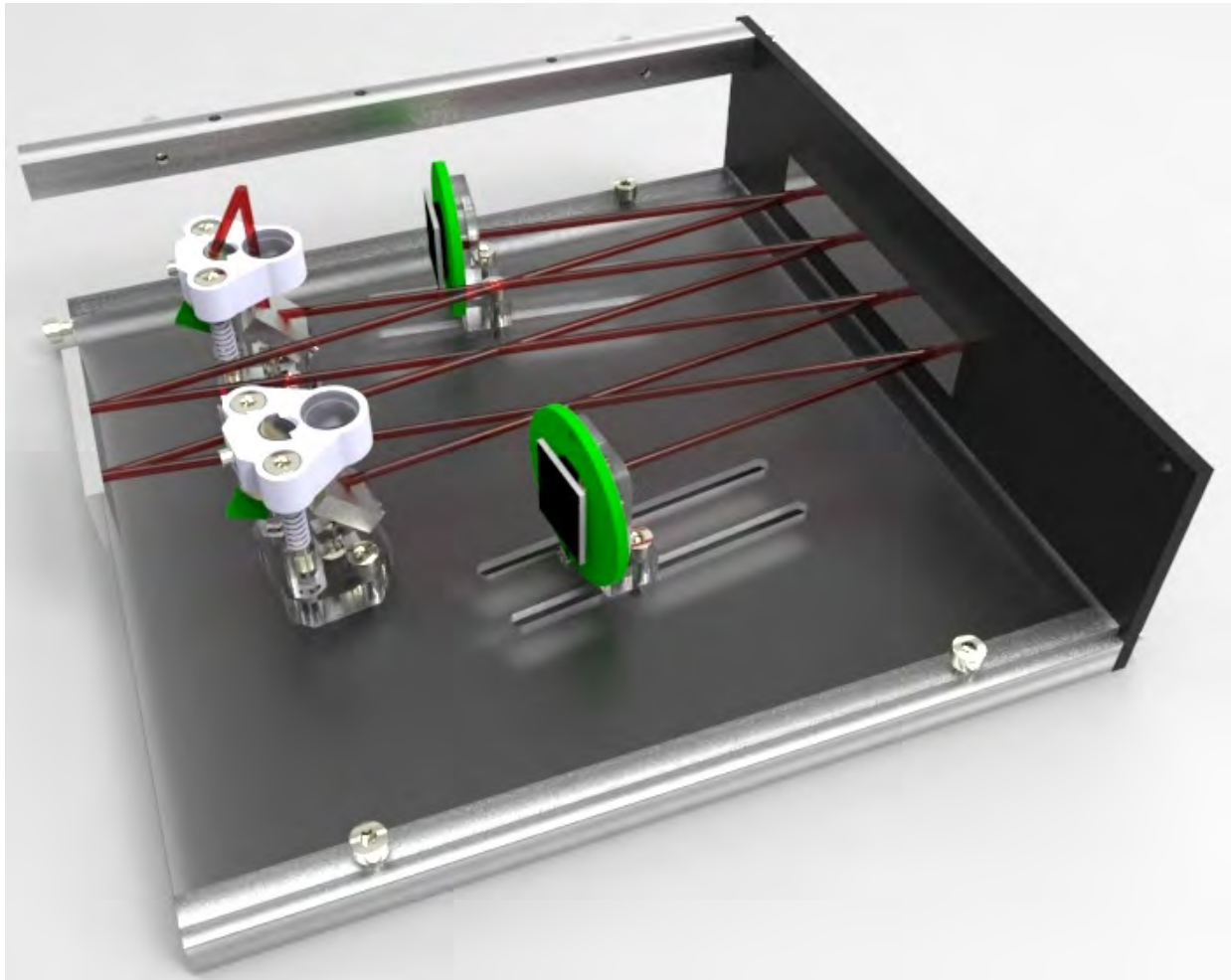


Figure 5.5: Visualization of the optical compartment, with the $40\times$ magnification configuration. This complete optical compartment can be removed easily from the system for easy and quick adjustments. The second laserspot is hidden for better visibility.

5.2 Actuator

The actuator for the planar stage system should

- be able to actuate in the 3 DOFs without stacking
- have long strokes
- be linear

With these criteria the Lorentz actuator concept has been selected.

Figure 5.6 shows how the actuators needs to be oriented to control all 3 DOFs. The force transformation matrix shows how the 3 DOFs can be actuated with the three actuators.

$$\begin{bmatrix} F_x \\ F_y \\ T_z \end{bmatrix} = \begin{bmatrix} 1 & 0 & 0 \\ 0 & 1 & 1 \\ l_1 & l_2 & -l_3 \end{bmatrix} \begin{bmatrix} F_{act-x} \\ F_{act-y1} \\ F_{act-y2} \end{bmatrix} \quad (5.2)$$

The different l 's are the perpendicular distances between the force of each actuator and the center of mass.

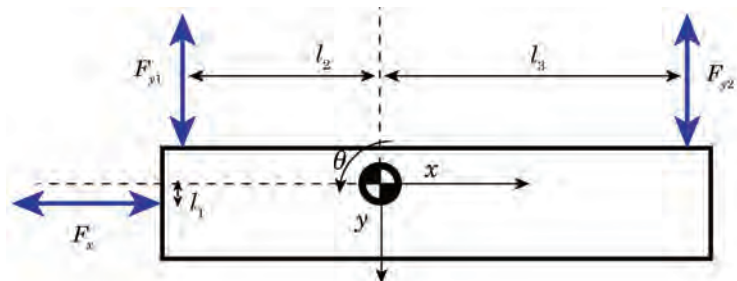


Figure 5.6: Schematic topview of the moving stage with the location of the three actuation forces to actuate the three planar degrees of freedom. X and Y translation and θ the planar rotation. When the center of mass is not in the middle a transformation matrix needs to be used to convert the global forces to actuator forces.

5.2.1 Lorentz force

The Lorentz force is an interaction between the current in a coil and a magnetic field. This force is described with[16]

$$\mathbf{F} = n \cdot l \cdot \mathbf{I} \times \mathbf{B} \quad (5.3)$$

where \mathbf{F} is the Lorentz force, n is the number of wires, l is the length of the coil in the magnetic field, \mathbf{I} is the current and \mathbf{B} is the magnetic field. A representation is shown in Fig.5.7.

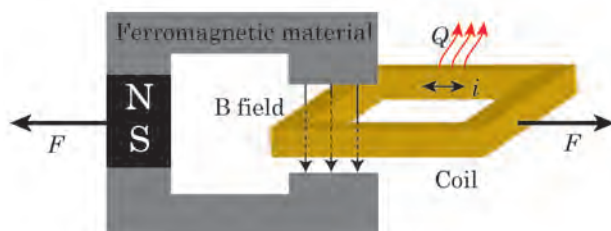


Figure 5.7: A schematic representation of a Lorentz actuator. A force is generated between the two parts due to the interaction between the magnetic field and the current in the coil. The current produces heat, which is unwanted in a precision stage.

5.2.2 Magnet and coil configuration

The force of the Lorentz actuator works between the coil and the magnet. So one of these parts should be connected to the mover. Figure 5.7 shows that heat is dissipated in the coil

$$Q = I^2 R \quad (5.4)$$

Heat causes thermal expansion which is not desired on the mover, where the sample is placed on and where the accuracy is required.

$$\delta = \alpha l \Delta T \quad (5.5)$$

where α is the thermal expansion coefficient, l is the distance between the edge of the mover, thus homing location and the point of interest.

This thermal expansion is already $11\mu\text{m}$ when the mover has an increased ΔT of 10K , on an aluminum stage with an l of 50mm . Therefore, the coils are placed on the base and the magnets on the mover, thus a moving magnet configuration.

Sizing

The actuator needs to work over the full stroke of the mover, in both DOFs. Figure 5.9 shows how this is achieved. In the actuation direction the coil is much smaller than the magnet, so that it can be kept in the middle part of the magnet where the magnetic flux density is higher and more constant. In the non-actuated direction the coil is longer than the magnet, making sure that it is always covered by the magnet.

A magnet has been selected which fulfills all these requirements. The stroke of the stage is 10mm , the coil width is 2mm and the edges of the magnets should be avoided due to stray. Resulting in a magnet length of 14mm . A small and thin 14mm magnet was found, see Fig.5.8.

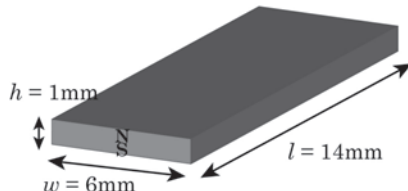


Figure 5.8: A small thin plate magnet has been selected for a lightweight actuator

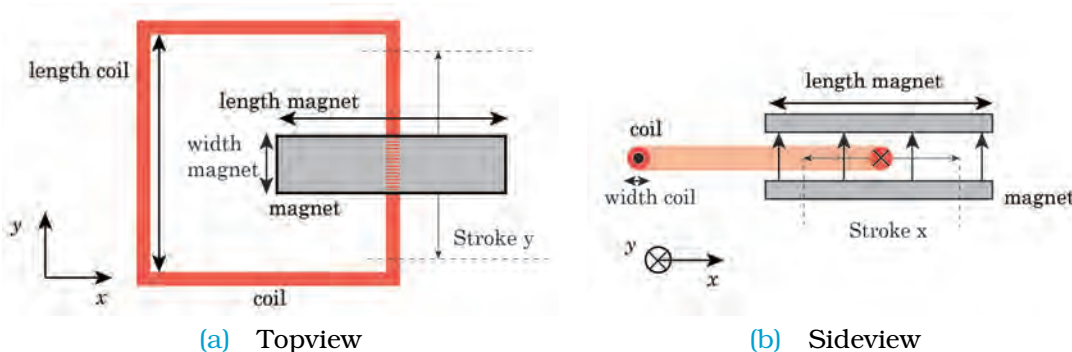


Figure 5.9: Schematic of the magnet coil configuration. The length of the coil is bigger than the magnet such that the coil is always covered by the magnet over the whole y -range. In the x -direction the magnet length is much larger than the coil width, making sure that the coil is always covered by the magnet.

5.2.3 Magnetic circuit

To determine the Lorentz force, the flux density B needs to be determined. Before showing that, some theory about magnetism is introduced first.

The flux in a magnetic circuit can be written as[12]

$$\Phi = \frac{\mathcal{F}}{\mathcal{R}_t} = \frac{B_r l_m}{\mu_0 \mathcal{R}_t} \quad (5.6)$$

where \mathcal{F} is the magnetomotive force and \mathcal{R}_t the total reluctance in the system. B_r and l_m are the remanent flux and length of the magnet and μ_0 is the permeability constant.

The total reluctance can be determined by the summation of the reluctance of all components in the magnetic circuit

$$\mathcal{R}_t = \sum_{i=1}^n \mathcal{R}_i = \sum_{i=1}^n \frac{l_i}{A_i \mu_0 \mu_{r,i}} \quad (5.7)$$

where the index i denotes the different reluctance components and n the total number of reluctance components. A , l and μ_r are the area, length and relative permeability of each component. The relative permeability is almost unity for magnets and air, ferromagnetic materials can have very large μ_r .

The flux density in each component can be determined with

$$B_i = \frac{\Phi}{A_i} \lambda_i \quad (5.8)$$

where λ is the stray flux coefficient in such a component. This coefficient indicates how much flux is effectively used.

Hopkinson's law is used to visualize these magnetic properties, see Fig.5.10. Here, the analogy is made between an electrical and magnetic circuit: reluctance \mathcal{R} is equivalent to resistance, flux Φ to current and voltage to magnetomotive force \mathcal{F} .

For a high Lorentz force a high flux density in the airgap B_g is preferred. This can be achieved by increasing the flux, which can be done by either selecting a stronger and larger magnet, or by decreasing the reluctance.

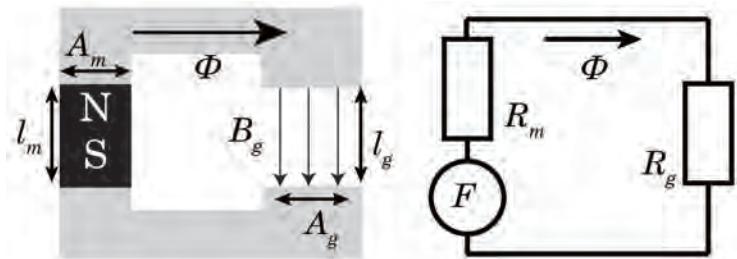


Figure 5.10: 1D representation of a magnet circuit with Hopkinson's analogy. The reluctance of the ferromagnetic yoke is neglected because the μ_r is very high, this is only valid when the material is not saturated.

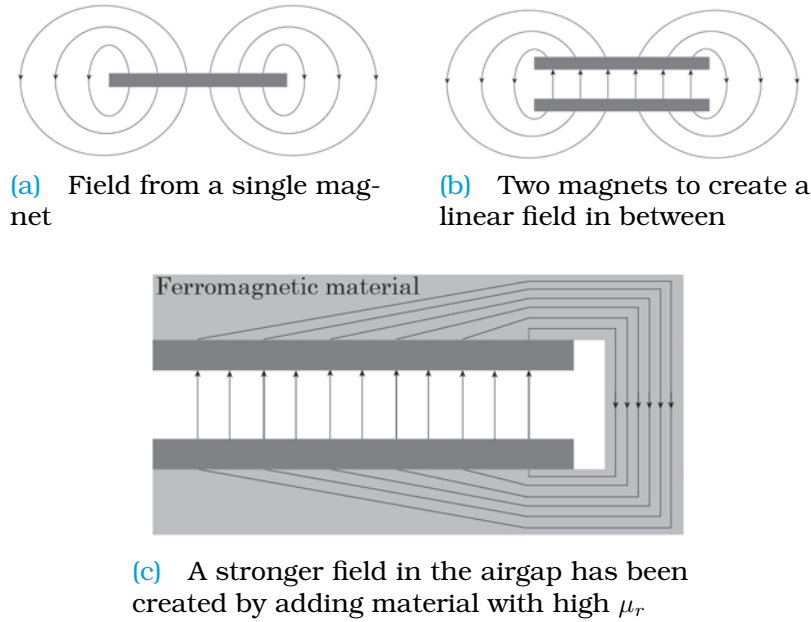


Figure 5.11: A double magnet configuration with a yoke of low reluctance material is chosen, for a more uniform and higher flux density in the airgap.

In the case of a single magnet the field lines are going curved, see Fig.5.11a. The flux density decreases with increasing distance from the surface. This is solved by placing another magnet with the same alignment. Since the reluctance and distance between the two magnets are constant the flux density will be uniform. This is shown in Fig.5.11b.

If the reluctance of the return path is lowered using a ferromagnetic yoke with high relative permeability, the magnetic flux density in the gap can be raised. This configuration is shown in Fig.5.11c.

Soft magnetic 1010 steel has been selected as yoke material, with a saturation flux of 2.0T. Hysteresis shouldn't be a problem in this actuator, since the magnetic flux is constant. The cross sectional area of the yoke is sized such that it doesn't saturate. However, sizing it too big will add extra weight to the mover, indirectly reducing the effectiveness of the system.

Now that the magnet configuration has been designed, the flux density in the airgap can be calculated with Equation 5.6 to 5.8. The flux density in the airgap is approximated on 0.49T, with a stray flux coefficient λ of 0.9 and a permanent magnet with a remanent flux B_r of 1.32T.

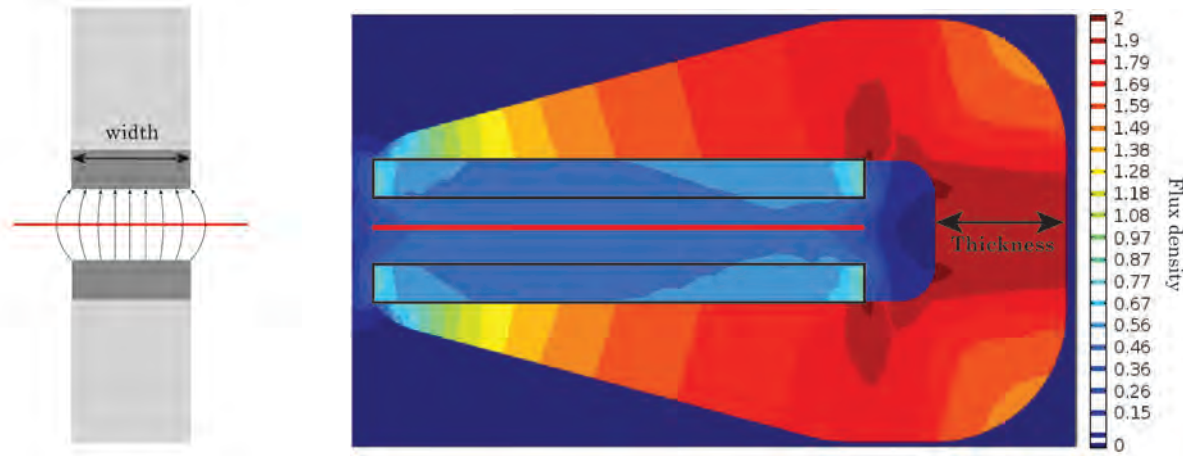
5.2.4 Optimizing yoke shape

The schematic yoke configuration shows that the yoke is not efficiently utilized. In the arms where the magnets are attached the flux in the material is decreasing linearly. To save moving mass, the optimal shape has been determined by making a 3D FEM simulation of the magnetic flux in COMSOL.

The simulation shows that the field lines are indeed not evenly distributed and that the reduction of moving mass is possible. With a parametric sweep different yoke thicknesses were modeled quickly. The thinnest and lightest configuration without saturation is 4mm, see Fig.5.12b. The flux density in the yoke is shown, the material is

indeed apart from the flux concentrations not fully saturated.

The coil is much longer than the magnet and will even pick up the strayed field lines. Therefore, the effective flux density is determined by taking the integral of the flux over the red line in Fig.5.12a, divided by the width of the magnet(6mm). The effective flux over length of the airgap is shown in Fig.5.13. It shows that the effective flux density in the first and last 1.5mm are not constant. The middle part has a light increasing slope of less than 5%.



(a) Front view of the actuator. The coil picks up all the flux over the whole range, even the strayed lines at the sides.

(b) Cross section of the yoke, showing the flux density. There are some flux concentrations which are saturated, but in general the flux is evenly distributed. Meaning that the magnetic material is efficiently used. The red line in the middle is the integral plane for Fig.5.13

Figure 5.12: The simulation show that a 4mm yoke thickness is the lightest solution without saturation.

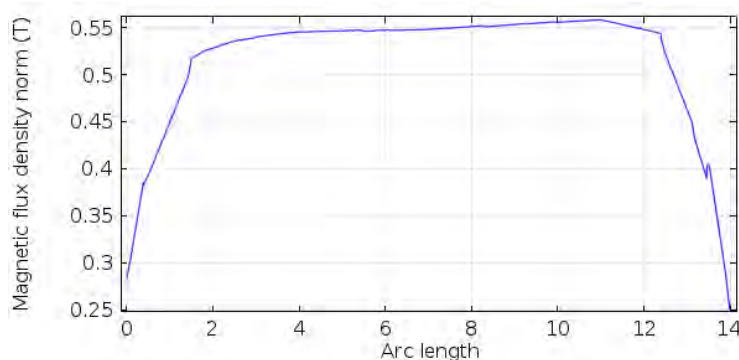


Figure 5.13: This figure shows the effective flux density in the airgap over the length of the magnet. It is determined by integrating the flux density and dividing it by the width of the magnet. It shows that the middle part of the magnet is quite linear with a slope of less than 5% and an average airgap flux density of 0.55T.

5.2.5 Coils

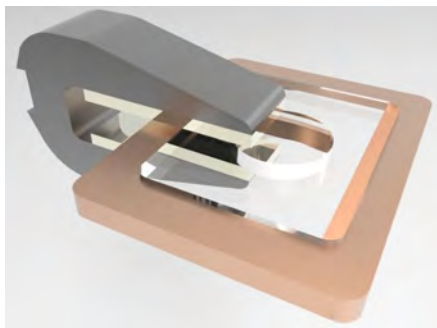
Now that the magnets are determined the other part of the actuator, the coils, are sized. The required force is 0.5N and with an effective flux density B_g of 0.55T and a magnet length l of 6mm. A coil with an $I \cdot n$ of 150 needs to be designed.

For high efficiency, low currents and large amount of windings is preferred. This is because of the squared relation between current and heat dissipation. However, when too many windings are used it decreases the producibility.

After some iterations (which included the compatibility with the amplifier, discussed in Section 5.3) an 1A with 150 turns configuration is selected which is fed with a 12V voltage supply and can produce 0.5N. The coil was designed without a flange so that the airgap is used more efficiently. The full design is shown in Fig.5.14a and an overview of all actuator parameters are shown in Table 5.2. The measured values are determined in Section 5.2.6.

Table 5.2: Overview of all designed and validated parameters, the validated parameters are discussed in Section 5.2.6.

Parameter	Designed	Measured
Height airgap	3 mm	3 mm
n turns	150	150
current	1 A	1A
Airgap flux density	0.55 T	0.48T
Force	0.5 N	0.38N



(a) Final design of the actuator. The coil is wound around a plastic center, and is placed between two thin plate magnets with a ferromagnetic yoke



(b) The built actuator, the yoke was made by lasercutting the contour out of a 2mm thick steel plate. Three of these are stacked together to get the full yoke.

Figure 5.14: The designed and built actuator.

5.2.6 Validation

The coils are self-wound and were measured with an RLC meter so that the resistance and self-inductance can be determined. These parameters are necessary for the design of the filter for the amplifier which were discussed in section 5.3 and are shown in Table 5.3

The yokes are measured with a Gaussmeter which gave an airgap flux of 0.48T, this is very close to the 1D approximation with a stray flux coefficient of 0.9. The results of

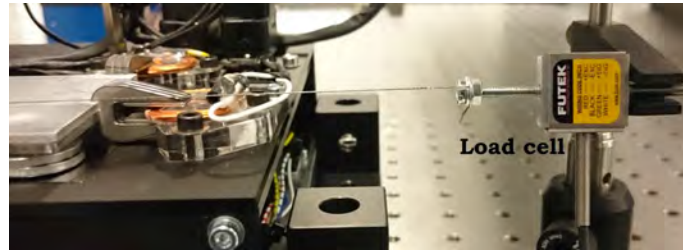


Figure 5.15: Load cell setup to determine the force and motor constant of each actuator, the load cell measures the force in the cable. While the current and the position of the stage are measured.

the simulation is expected to be higher the stray at the sides is included.

To check if the material was saturated, another yoke slice was added increasing the cross sectional area by 33%. This didn't result in a raise in flux in the airgap and means that the material was not saturated.

To check how much force the actuator can produce, a load cell was used to determine the motor constant of each actuator. The setup is shown in Fig.5.15. A cable was attached on the mover in line with the actuator force, this force will be transmitted through the cable and was measured by the loadcell. The current through the coil and the location of the mover were also measured. The motor constant is obtained with

$$K_t = \frac{F}{I} \quad (5.9)$$

This means that the maximum force at 1A is 0.38N, 24% less then calculated. The difference can be explained by the reluctance force of the coil on the ferromagnetic yoke is attracting the yoke to the coil. The direction of the measured force was out of the coil while the reluctance force wants to pull the yoke into the coil. However, the force is still more than enough to reach the requirement of 500mm/s².

By repeating this measurement on different location the position dependency on the K_t can be determined, see Fig.5.16, an increase of 0.4% per mm can be observed. This matches the slope of the increasing field density from the FEM model in Fig.5.13.

Table 5.3: Overview of the coil values

Actuator	L [μH]	R [Ω]	K_t [N/A]
Actuator 1(x)	740	9	0.383
Actuator 2(y1)	730	11	0.365
Actuator 3(y2)	730	11	0.358

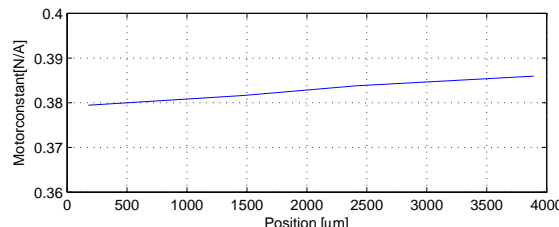


Figure 5.16: The motor constant over the x stroke, only a small portion could be measured due to the range of the displacement sensor. The motor constant increases linearly with 0.4% per mm, which matches the flux density simulations.

5.3 Amplifier

The amplifier of the planar stage system should be

- thermally efficient
- compact
- low cost

With these requirements, a switched mode amplifier has been selected. These amplifiers can control the voltage or current, by switching on and off. The ratio between on and off determines the amplitude and is called pulse width modulation (PWM).

5.3.1 Dual-ended configuration

To have a bi-directional force with the Lorentz actuators, a bi-directional current is required. A dual-ended amplifier can switch in forward and backward direction, as shown in Fig.5.17.

5.3.2 Output filter

Due to the switching of the amplifier, current ripple is introduced [17]. Therefore, an output filter has been designed to reduce this ripple. High switching frequencies can efficiently be filtered out by a low-pass filter. Therefore a dual-ended amplifier with a switching frequency of 100kHz was selected which fulfills the power specifications.

Since the Lorentz actuator is an inductive and resistive load. It already works as an RL low-pass filter for the ripple current. However this ripple is reduced even more by introducing another filter. A 2nd order LC filter is added to the circuit. This filter is preferred above an RC filter because it has a steeper roll-off after the cut-off frequency. Additionally, no power is dissipated over the resistor. However, this LC circuit has a resonance, which needs to damped with an RC damper. This is shown in Fig.5.18.

This filter was modeled by first calculating the total impedance of the parallel components.

$$\frac{1}{Z(s)} = \frac{1}{Z_C(s)} + \frac{1}{Z_{damper}(s)} + \frac{1}{Z_{load}(s)} \quad (5.10)$$

$$Z(s) = \frac{1}{Cs + \frac{1}{R_d + \frac{1}{C_d s}} + \frac{1}{R_l + L_l s}} \quad (5.11)$$

The transfer function from input to output voltage is then given by,

$$H(s) = \frac{V_o}{V_i} = \frac{Z(s)}{R_f + L_f s + Z(s)} \quad (5.12)$$

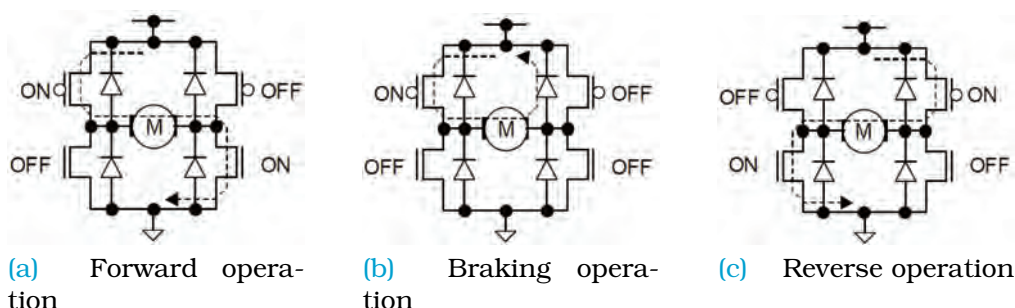


Figure 5.17: The 3 modes of operation of the dual-ended amplifier, which are controlled by a PWM signal generated by the controller on the Arduino.

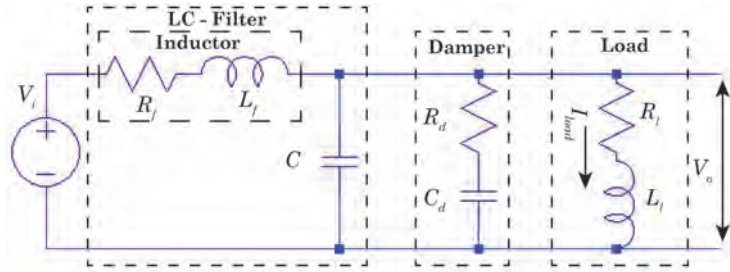


Figure 5.18: This figure shows a schematic of the output filter. The amplifier with the Lorentz actuator are only the voltage source and the load. To reduce the current ripple an LC filter is added, this is required to filter the 100kHz ripple current. This LC circuit has a resonance frequency where it will resonate, by adding a resistance in parallel as damper this resonance is damped. This resistor however will dissipate power, therefore an additional capacitor is placed in series so that the resistor will only dissipate energy near the resonance frequency of the LC filter.

Dividing this voltage transfer function by the impedance of the load gives the transfer function of the current on the load.

$$H_I(s) = \frac{I_o}{V_i} = \frac{H(s)}{Z_{load}(s)} \quad (5.13)$$

$$H_I(s) = \frac{C_d R_d s + 1}{k_1 s^4 + k_2 s^3 + k_3 s^2 + k_4 s + (R_l + R_f)} \quad (5.14)$$

with

$$k_1 = CC_d L_l L_f R_d \quad (5.15)$$

$$k_2 = C_d L_l L_f + C L_l L_f + C C_d L_f R_l R_d + C C_d L_l R_d R_f \quad (5.16)$$

$$k_3 = C L_f R_l + C L_l R_f C_d L_l R_d + C_d L_f R_l + C_d L_l R_f + C_d L_f R_d + C C_d R_l R_d R_f \quad (5.17)$$

$$k_4 = C R_l R_f + C_d R_l R_d + C_d R_l R_f + C_d R_d R_f + L_l + L_f \quad (5.18)$$

This gives 5 unknowns which are complexly coupled. Therefore a simplified LC filter with a chosen cut-off frequency will be determined first.

$$LC = \frac{1}{(2\pi f_c)^2} \quad (5.19)$$

The cut off frequency is chosen to be 500 Hz, this is over-designed so that the amplifier can be used for other projects too. The ratio of L and C has been determined by looking at the maximum peak current through the inductor.

$$L_f = \frac{V_{i_ppr}}{2\pi f_{pwm} I_{L_rpp}} \quad (5.20)$$

where V_{i_ppr} is the expected peak to peak ripple voltage, f_{pwm} the carry frequency and I_{L_rpp} the maximum desired current through the inductor. An inductor was selected with $68\mu\text{H}$ and a rated current of 1.3A. This was matched with a $10\mu\text{F}$ capacitor to have a cut off frequency of 610 Hz.

The damping resistor should be chosen low enough to reduce the Q factor of the resonance, but not too low to prevent high power losses at high frequency.

$$Q = R \sqrt{\frac{C}{L}} \quad (5.21)$$

Table 5.4: The designed filter variables.

Filter variables	Values	Filter variables	Values
L_l	$736 \mu\text{H}$	L_f	$68 \mu\text{H}$
R_l	9.6Ω	C_f	$10 \mu\text{F}$
C_d	$47 \mu\text{F}$	R_f	0.2Ω
R_d	4.7Ω		

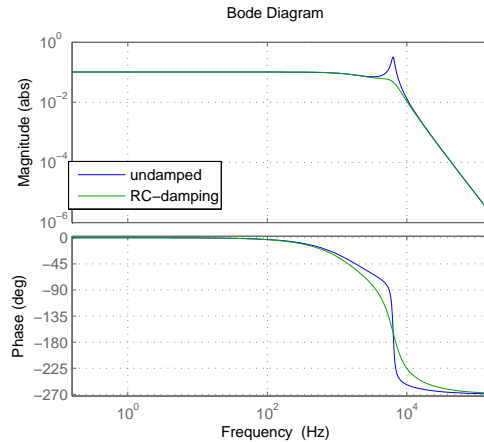


Figure 5.19: Frequency response of the amplifier and filter with a coil as load. The resonance is damped out by an extra RC branch. Till around 1kHz the magnitude is constant. The carry frequency is 100kHz, which has a magnitude of around 10^{-5} .

Table 5.4 shows the designed filter values and a frequency response is shown in Fig.5.19. The gain is constant up to about 1kHz, the gain at the PWM frequency of 100kHz is 10^{-5} , resulting in ripple current of less than 0.05 mA in the coil.

LTspice model

Because a dual-ended amplifier is used, the load is filtered on both sides. This second branch was not taken into account in the Matlab model, and was modeled in LTspice, see Fig.5.20. The model of the dual-ended filter is shown on the left, where all variables denoted with a 2 is the mirrored version of the previously determined filter. On the right the frequency response of this system is simulated. The simulation gave the same result as the Matlab model.

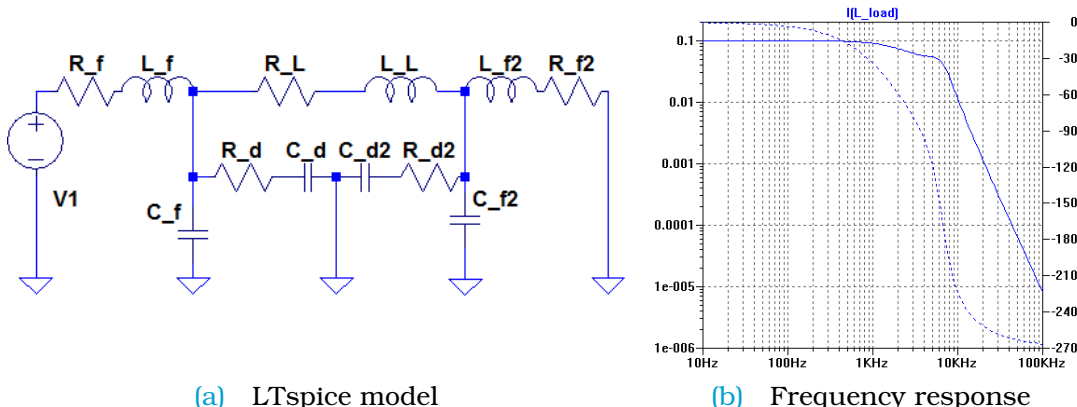


Figure 5.20: The simulation of the same filter in LTspice with components in dual-ended configuration. This matched with the simplified Matlab model.

5.3.3 Schematics

A shunt resistance of 1Ω is placed between the coil and the filter to measure the current. The voltage drop over this current induced by the current cannot be directly measured, this is because the shunt is bi-directional and thus floating. A differential amplifier with high input resistances is used to measure the voltage difference. This signal is amplified with a factor 1 and filtered with a lowpass filter with a f_c of 160 Hz, by putting a capacitor parallel to the feedback resistor. This can be seen in Fig.5.21 in one of the measurement circuits blocks. This signal is conditioned such that it can be fed into the analog-to-digital converter (ADC) of the Arduino or directly on the scope and data acquisition devices (DAQ) devices.

5.3.4 Board design

On the left side of the board, the dual-ended amplifiers and their filters are located. The measurement circuit is on the right side. These parts are separated to reduce crosstalk on the more sensitive measurement circuits. A separated ground plane is added to reduce the crosstalk and electromagnetic interference (EMI).

The measurement circuit is only used during the validation of the electronics and can be omitted from the actual amplifier board, this can reduce the cost and size with a factor two. The full wiring schematic showing how the amplifier is connected to the Arduino, coils and power supply can be found in Appendix A.5.

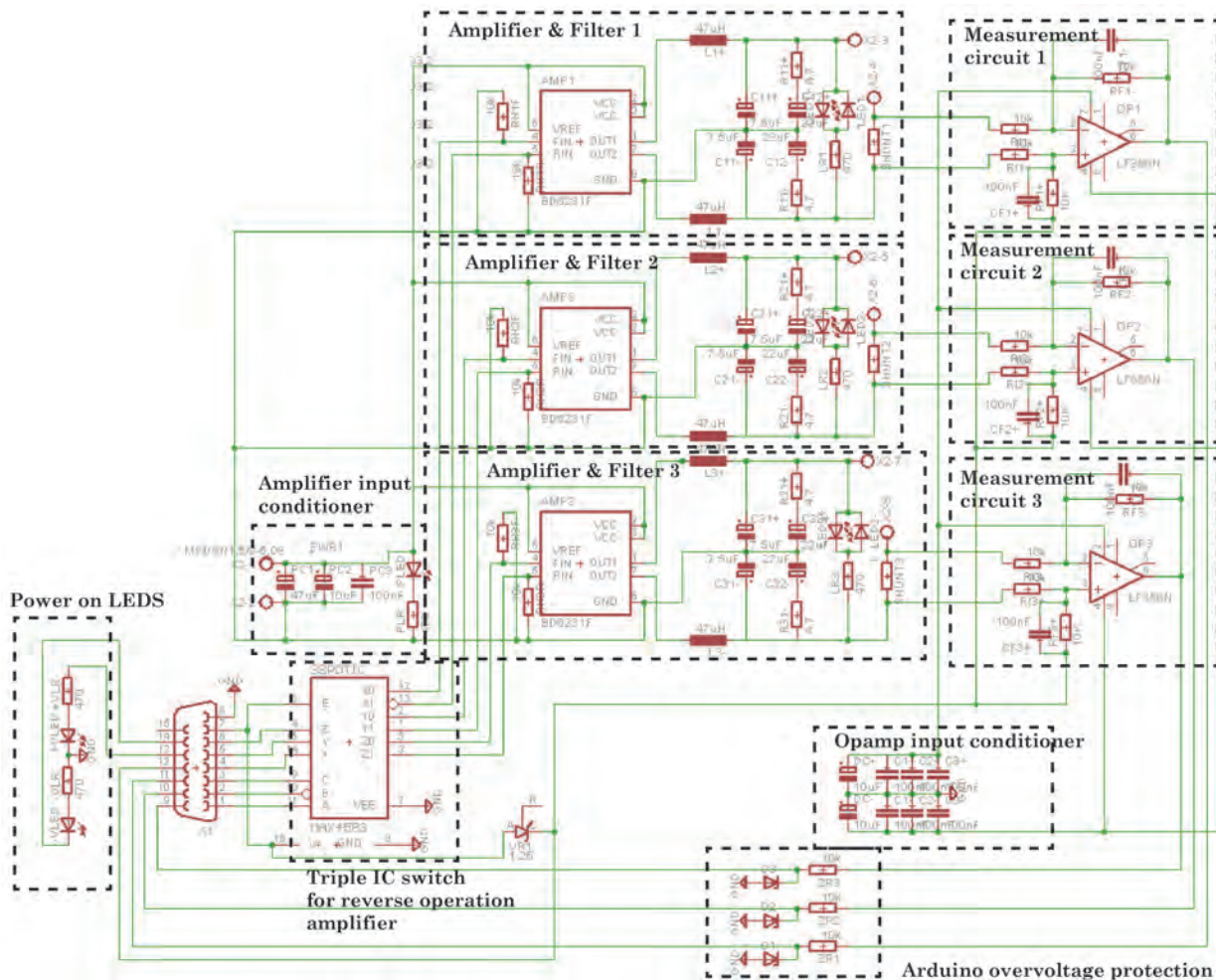


Figure 5.21: The schematics of the board design, with the incorporated measurement circuits and other peripherals

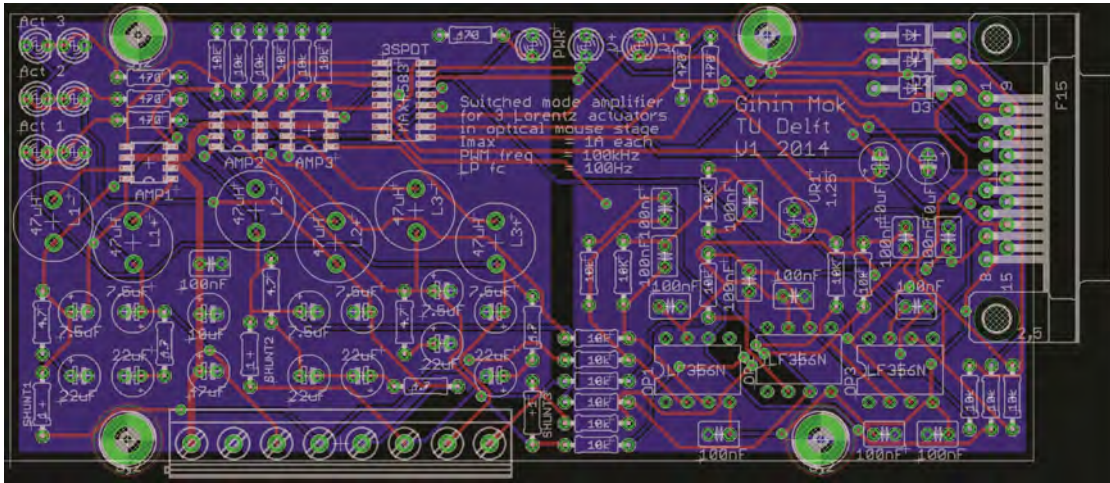


Figure 5.22: The PCB design of the board. The left side is the amplifier side with high currents. On the right side the measurement circuit is located. The circuits are separated and a ground plane is added to reduce crosstalk and electromagnetic interference. All the files are can be found in the archive.

5.3.5 Validation

The full amplifier including the coil was validated with a frequency sweep. Figure 5.23 shows a schematic of the setup. A sine wave is generated with the Arduino and is used as reference. The sine wave is also used to make a PWM signal to control the amplifier. The current in the coil is measured with a shunt resistance. By using a fast fourier transform (FFT), the amplitude of the the frequency response was obtained, see Fig.5.24. The magnitude is constant in the working range till 100Hz as expected. At higher frequencies, the loop speed of the Arduino wasn't high enough to produce sine waves with enough samples.

The phase couldn't be extracted by Matlab. Therefore the overlay of the two signals was observed. Till 400Hz the overlay was still good and no phase lag could be seen, which is shown in Fig.5.25. This means that in the working range of 100Hz there is no phase shift as expected. It is also already visible that the loop speed of the Arduino was not sufficient.

This proves that in the working range of 100Hz the amplifier is as designed. Another validation method needs to be found to validate for the higher frequencies.

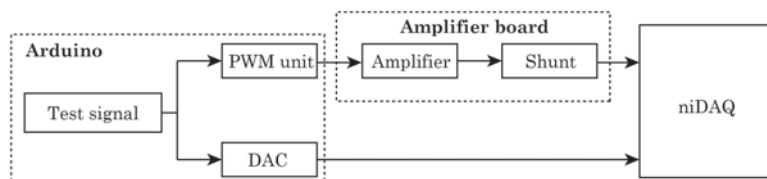


Figure 5.23: Schematic overview of the validation setup. A test signal was generated in the Arduino, in this case a sine. This sine was used to make a reference signal for the measurement with the DAC. The sine was also propagated to the PWM unit to get a PWM signal for the amplifier. The voltage drop over the shunt was then measured by the niDAQ to get the current through the coil.

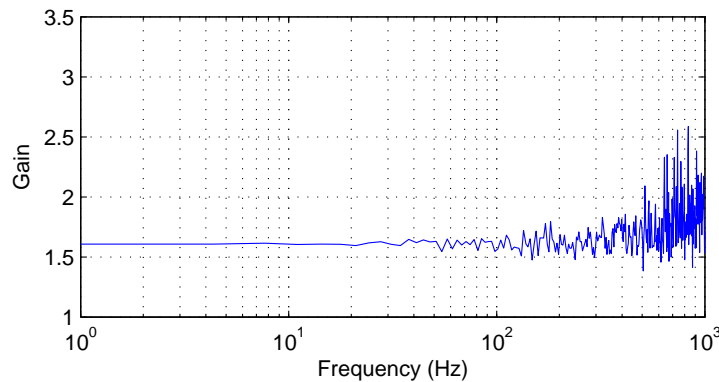


Figure 5.24: The magnitude of the frequency response of the amplifier, filter and actuator system. A sinesweep was generated by the Arduino and was compared with the current through the actuator. The loop frequency of the Arduino was however not high enough, generating low quality sine signals at higher frequencies. Till the system's working range of 100Hz the gain was constant as expected

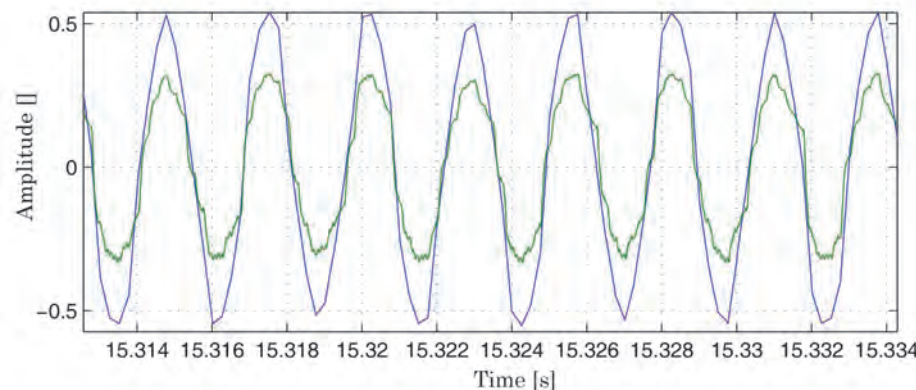


Figure 5.25: Till 400Hz the overlay of the signals was still good. Thus, no phase shift can be observed in the working range till 100Hz, as expected. The degrading of the quality of the sine signal due to the low loop speed of the Arduino was clearly visible at this frequency.

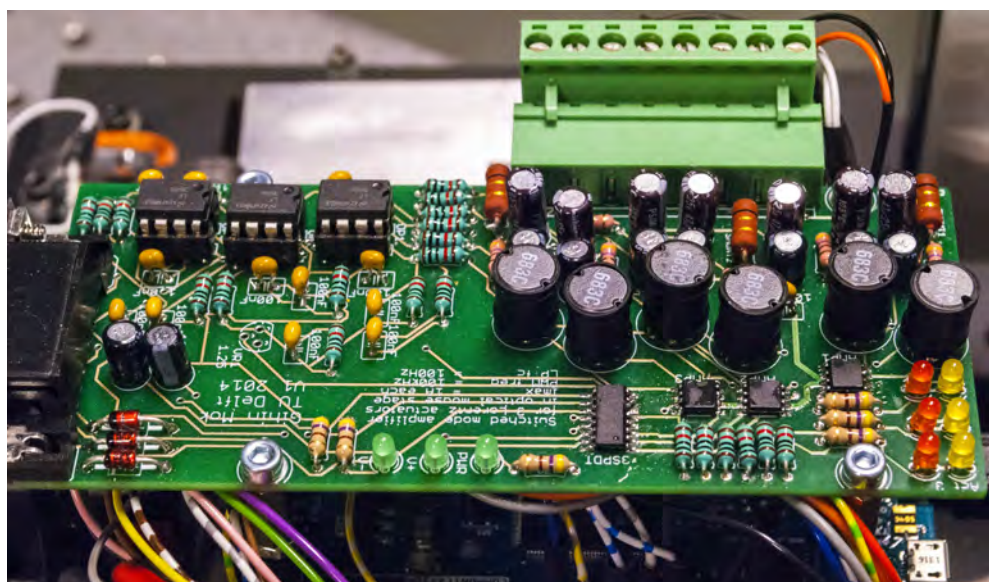


Figure 5.26: The fully assembled amplifier

5.4 Mover

The mover positions the sample so that it can be observed by the microscope. This mover needs to move in-plane with low or no friction for better controllability.

5.4.1 Bearings

The most simple method would be a 3 ball supports with a layer of Teflon in between. This method is kinematically determined[15] and has a high height stiffness too. This height stiffness is important because it influences the magnification, when the S_1 distance varies.

Two methods with Teflon were implemented, by coating the ball contacts with Teflon spray and by adding Teflon pads. Both had the disadvantage that they introduced stick-slip. This slip was hard to control and the movement of the stage went faster than the mouse sensors could detect. The bearings were redesigned and all design considerations based on these bearings can be found in the archive.

5.4.2 Ferrofluids

Several projects about the design of ferrofluid bearings have been conducted recently in the research group. One of the properties of these bearings is that they are frictionless and thus will not introduce stick-slip into the system. The work of Max Cafe[13] and Simon van Veen[14] was extensively used during the design of the bearings for the planar stage system.

Load capacity

Ferrofluids are substances with dissolved ferromagnetic particles, which are attracted by a magnet. This property was used to make a layer of viscous liquid with no friction where the stage can float on, see Fig.5.27. By adding a ferromagnetic ring around the magnet, the magnetic flux density at the corner of the magnet has been increased. This increases the load capacity of the ferrofluid.

The layer of ferrofluid encloses an airpocket beneath the bearing, this airpocket increases the load capacity of the bearing. A safe assumption for a robust design is 50mbar[14]. Resulting in a load capacity of 0.4N per bearing, three of these are used to carry the weight of the mover of 100g, which is enough. These bearings are validated with an experimental setup. Weight was added to the bearings till the ferrofluid layer collapses and contact occurred between the surface and the magnet.

Vertical height

However, the ferrofluid introduces an issue, the vertical height. The ferrofluid bearings have a lower stiffness than ball contacts and have something called wetting. The vertical stiffness of a ferrofluid bearing is in the order of 10^4N/m which means that with varying loads from 0 to 20g, the maximum variation in height is $20\mu\text{m}$.

Next to the stiffness, there is another source for height variation. While moving the bearing leaves a ferrofluid trail behind, this reduces the thickness of the ferrofluid layer. This effect is about $2\mu\text{m}$ per mm translation[13]. Combining both height variations results in a maximum height variation of $40\mu\text{m}$. This causes a magnification variation of 0.3%, when S_1 is 12.7mm. This variation results in a maximum error of $30\mu\text{m}$, with a 10mm displacement. This is much higher than the required accuracy of $10\mu\text{m}$.

The first source of height variation is introduced by different loads on the mover. This can be solved by calibrating the sensor whenever a new load is placed on the mover.

The calibration is done by moving the stage from endstop to endstop, while measuring the displacement with the optical mouse sensors. This distance is known, so the sensitivity of the sensors can be determined. This calibration method can be performed by the end-users themselves and can be pre-programmed such that it is part of the start-up sequence.

The second source of height variation can be reduced by pre-wetting the surface before a measurement is done. A thin layer of ferrofluid is then already deposited on the surface, resulting in a smaller trail. This pre-wetting procedure is pre-programmed in the system and is part of the start-up sequence of the planar stage system.

The design of the bearing should prevent the decrease ferrofluid layer due to trailing. A small gap between the magnet and the ferromagnetic ring serves as a ferrofluid reservoir. How much these methods contribute to the loss in z-height hasn't been quantified or validated.

With these 3 methods the height variations should be minimized, however this hasn't been quantified or validated.

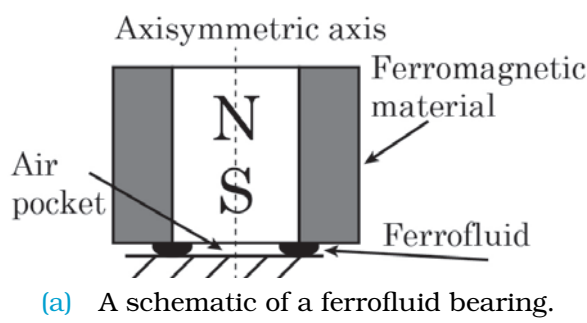


Figure 5.27: By putting a ferromagnetic material ring around the magnet, a higher flux has been achieved at the corners. This is because the reluctance for the returning path is lowered. Resulting in a higher load capacity, additionally the air trapped between the ferrofluid, magnet and the ground also adds load capacity.

5.4.3 Modal analysis

To determine if the mover is stiff enough, the eigenfrequencies are observed. The first estimation was done by simplifying the mover to an in the center of mass clamped cantilever beam with a mass on the end. The stiffness was determined with the beam equation

$$k = \frac{3EI}{l^3} \quad (5.22)$$

with E is the Young's modulus, I is the bending moment of inertia and l the length of the beam. This gives a stiffness of $4.4 \cdot 10^4 \text{ N/m}$.

The eigenfrequency was then determined by

$$f = \sqrt{\frac{k}{m}} \quad (5.23)$$

This gives a eigenfrequency f of 149Hz when the mass m is assumed to be 50g (half of the total mass of 100g) and the length l is 50mm.

A more detailed simulation was performed in COMSOL. An extra boundary condition was applied which should model the vertical connection stiffness of the ferrofluid and

was modeled as 10^4 N/m . The first two modes are shown in Fig.5.29 and shows that the first estimation is close with 149Hz versus the modeled 138Hz. The mode shape however, is instead of a longitudinal (the estimation) a diagonal flapping mode. These eigenfrequencies are higher than the design control frequency of 100Hz. The full drawings with sizes can be found in Appendix A.8.

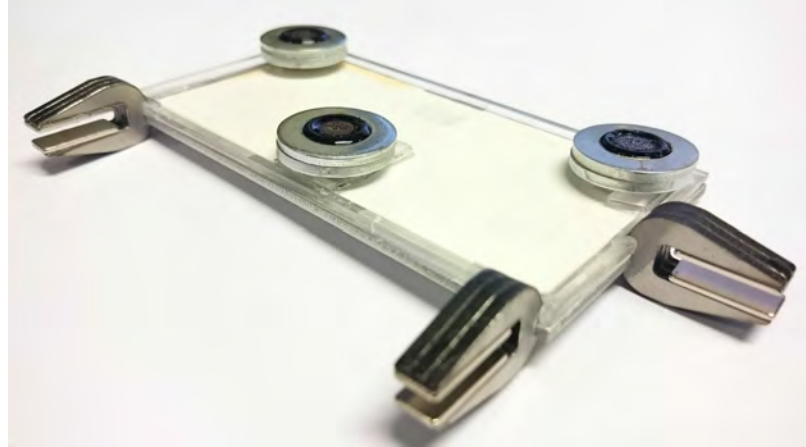
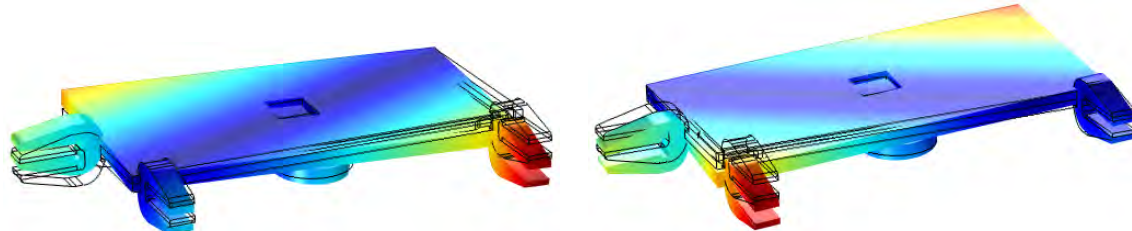


Figure 5.28: The fully assembled mover upside down, the white surface is the diffusely reflecting alumina measuring surface for the optical mouse sensors. Three magnet yokes are attached on the sides and three ferrofluid bearings can be seen.



(a) First mode at 138Hz, diagonal flapping (b) Second mode at 154Hz, other diagonal flapping

Figure 5.29: The eigenfrequencies of the mover, the first one is 138 Hz and is above the required actuation frequency of 100Hz.

5.5 Conclusion: Final design

After extensive design, simulation and validation, a compact and cost effective system has been realized using only simple and low cost components. The optical mouse sensor is integrated in the design and all the other components are designed for a control bandwidth of at least 100Hz.

The final design is as follows:

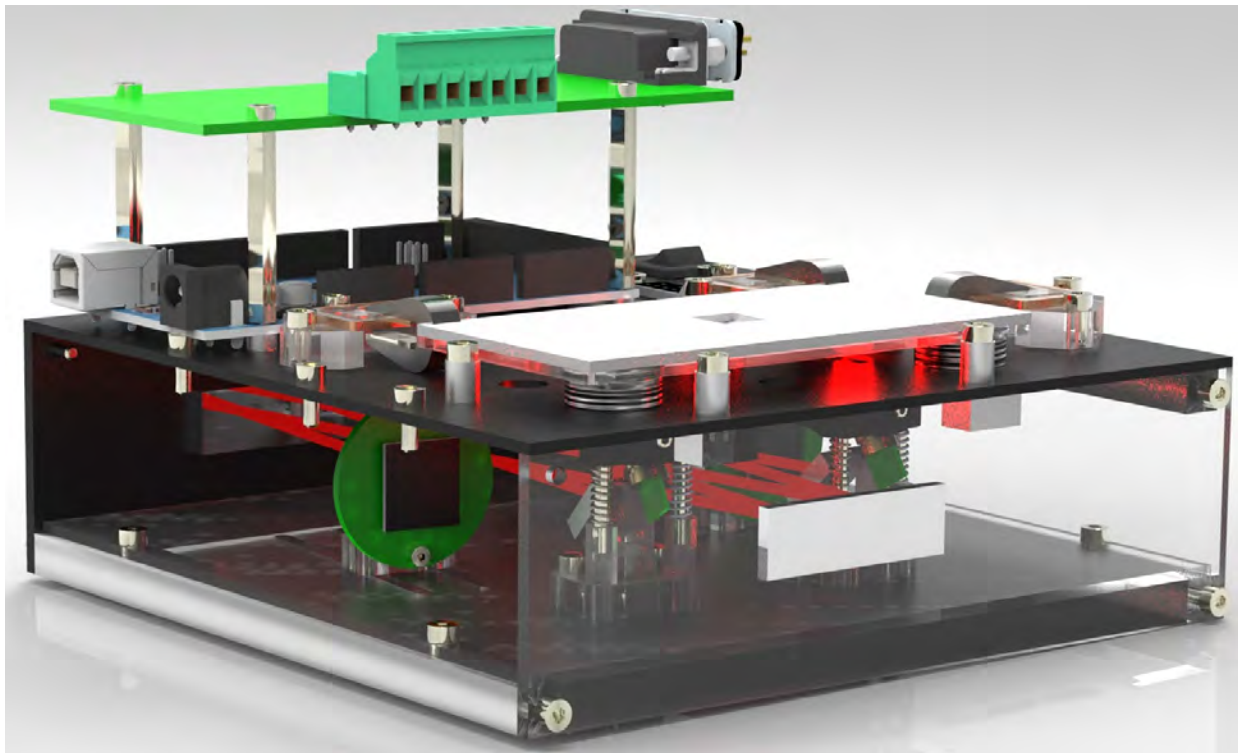
Two optical mouse sensors measure from the bottom of the stage, in line with the region of interest. Mirrors and lenses are used to "fold" the optical path and magnify the image up to $40\times$, which can be changed by interchanging the bottom plate.

Three Lorentz actuators actuate the stage in the 3 DOFs. A moving magnet configuration is chosen so that thermal expansion will not influence the region of interest. The mover is floating on a layer of ferrofluid, to decrease friction and remove stick-slip for higher positioning accuracy.

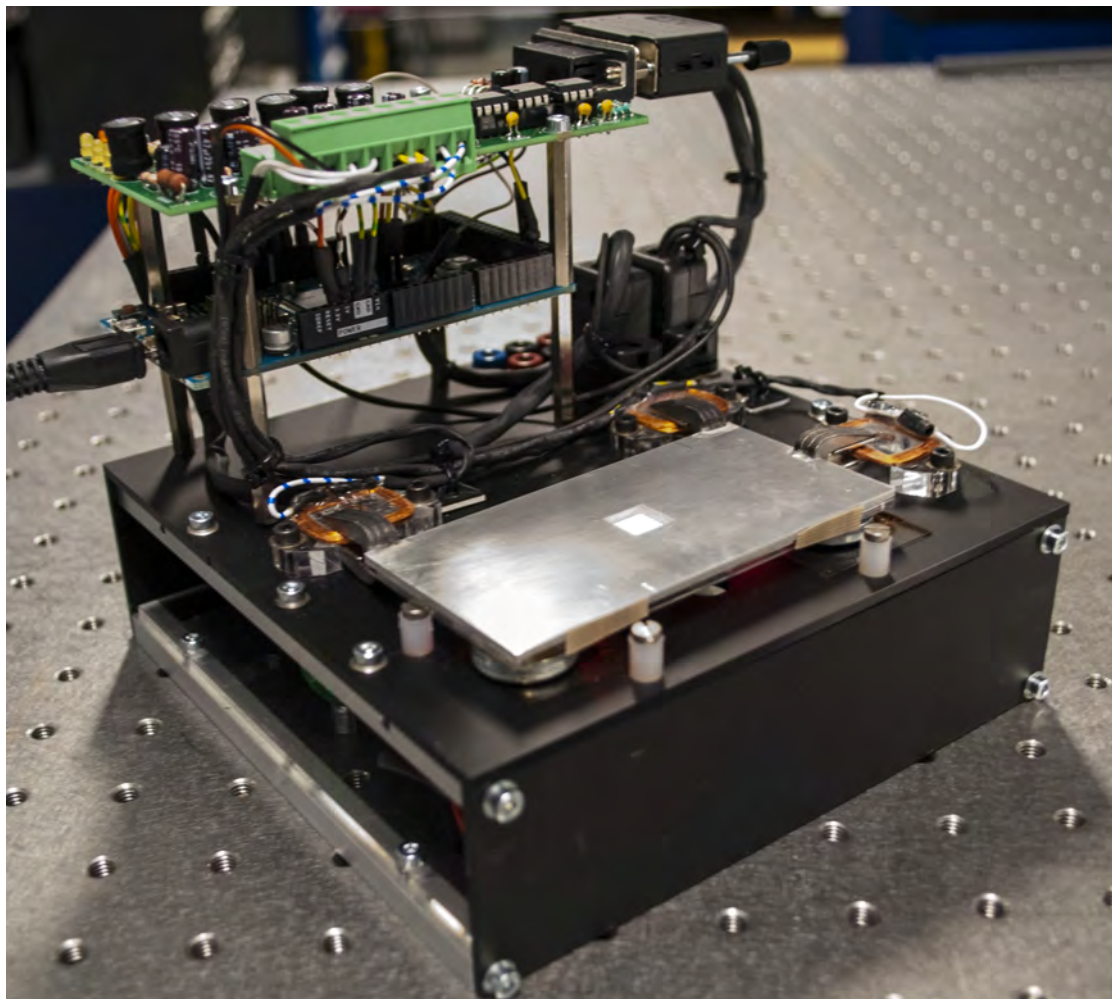
Low cost and high thermal efficiency, were the criteria to choose for switched mode amplifiers. To reduce the high frequency current ripple a LC filter is added. The planar stage is over-designed so that it can be used as a platform for future motion control projects in the department too.

In a complete system the control systems should be included too, however due to the complexity of the controller, the chapters are separated. The control system design is extensively discussed in Chapter 6.

The drawings with all the dimensions of the full system can be found in Appendix A.7.



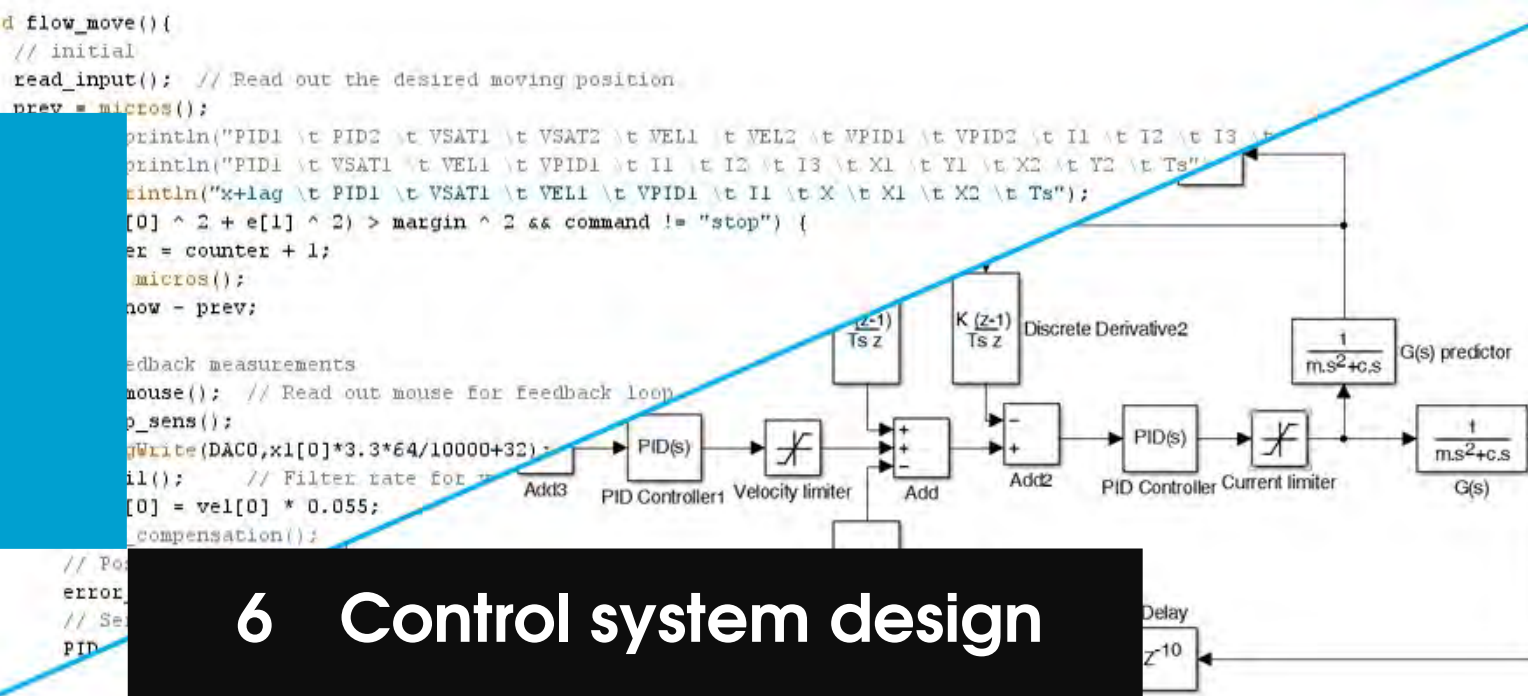
(a) Render of the full demonstrator stage. The front panel has been made transparent so that more of the optics can be seen.



(b) The fully assembled stage

Figure 5.30: The designed and the fully assembled stage.





6 Control system design

In this chapter the design of the controller is discussed. First the controller is designed on a simplified mass-damper model. System identification is performed to validate the model. At last the implementation is discussed.

6.1 Model

For the controller design an one DOF model is used. The mover is described with a mass-damper system as shown in Fig. 6.1. The mover is a floating mass, with damping from the ferrofluid bearings. This system can be described in the Laplace domain with,

$$G(s) = \frac{x}{F} = \frac{1}{ms^2 + cs} \quad (6.1)$$

where m is the mass and c is the damping coefficient. The damping coefficient of the bearing is taken from the measurements of Simon van Veen[14].

The actuator and amplifier gains are assumed unity with no phase lag at the working frequency. However, the optical mouse sensors introduce severe phase lag, this will be introduced later in this chapter.

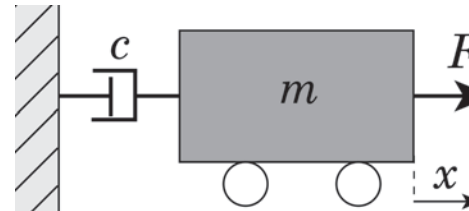


Figure 6.1: The dynamics of the stage is represented with a mass-damper model. The frictionless ferrofluid only has viscous damping, which is represented with the damper.

6.1.1 Control and velocity limit

Normal stages can use a conventional PID controller for positioning. However, the performance of the optical mouse sensors decreases when the velocity is too high, this was discussed in Section 3.2.3. Therefore, a cascaded position-velocity controller with a velocity saturation is designed. This control scheme is shown in Fig.6.2.

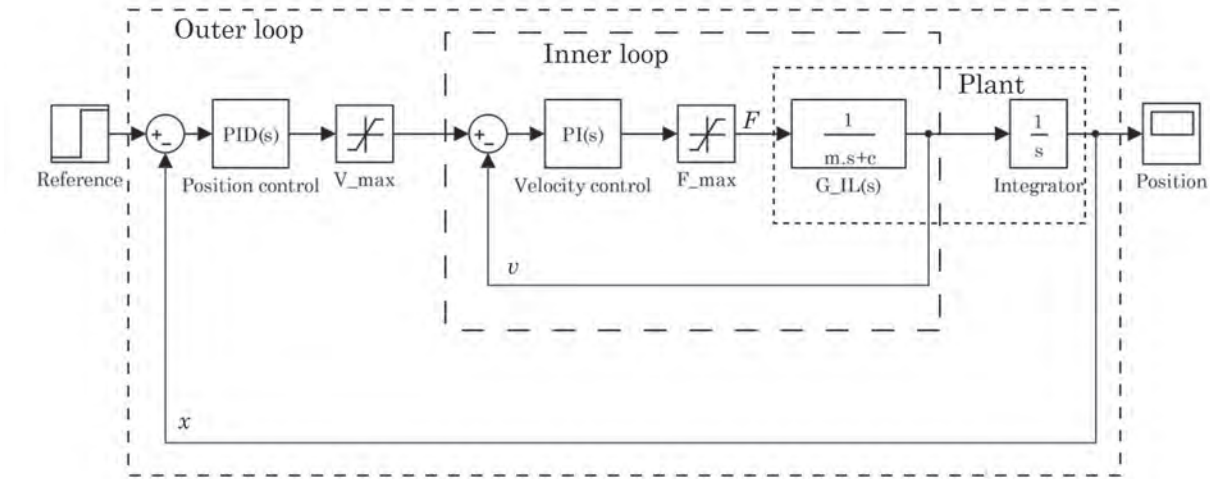


Figure 6.2: Control scheme of the cascaded position-velocity controller. This controller can position the mover while keeping the velocity within the optimal tracking velocity of the optical mouse sensors. The position controller gives a target velocity, if this target velocity is higher than v_{max} it gets saturated. The ideal inner-loop (controller plus the inner-loop plant, $G_{IL}(s)$) follows the saturated velocity target perfectly. The last integrator is only the conversion from velocity to position. Note, that this is a simplification, the velocity information is not present in the planar stage system, it can only be obtained by differentiating the position signal of the optical mouse sensor.

6.1.2 Inner-loop design

The first step is the design of the inner-loop. In the ideal world the closed-loop response of this inner-loop is unity. This means that the planar stage will always follow the velocity reference of the position controller.

That is for the ideal situation. The planar stage system requires a control bandwidth of 10Hz. A PI controller is used to control this inner-loop

$$C_{PI}(s) = k_{p-IL} + \frac{k_{i-IL}}{s} \quad (6.2)$$

The proportional action k_{p-IL} is determined by letting the open-loop response of the inner-loop cross the unity-gain cross-over frequency at 10Hz, see Fig. 6.3.

Integral action increases the gain at lower frequencies for better steady state and error rejection. However, the integration action also adds 90 degrees phase lag. In order to have a robust inner-loop the integral action should be stopped well before the control bandwidth. A "rule of thumb"[12] is to let the integration action stop at a frequency which is a factor 10 lower than the control bandwidth, resulting in

$$k_{i-IL} = 0.1f_c \cdot 2\pi \cdot k_{p-IL} \quad (6.3)$$

The open-loop transfer function of the inner-loop can then be described with

$$L_{IL}(s) = C_{PI}(s) \cdot G_{IL}(s) \quad (6.4)$$

The inner-loop can then be closed by

$$T_{IL}(s) = \frac{L_{IL}(s)}{1 + L_{IL}(s)} \quad (6.5)$$

Figure 6.3 shows the frequency response of the inner-loop. As designed, the open-loop cross-over frequency is at 10Hz, with a phase margin of approximately 120 degrees. The closed loop response is flat on unity till 1Hz. From then on closed-loop tracking is traded in for robustness. With a small slope in the gain till 0.7 at the control bandwidth of 10Hz.

Table 6.1: Inner-loop PI values for a control bandwidth of 10 and 1Hz

Control bandwidth	10Hz	1Hz
k_{p-IL}	6.5	5
k_{i-IL}	39	3.1

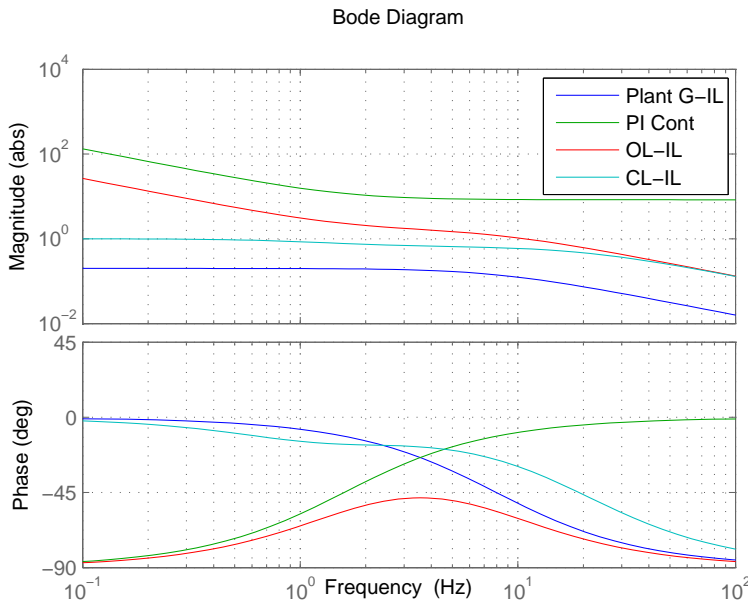


Figure 6.3: The bode plot shows the open- and closed-loop frequency response of the inner-loop. The open-loop unity-gain cross-over frequency is at the control bandwidth of 10Hz, with a phase margin of around 120 degrees. The closed-loop amplitude is unity till 1Hz, and decreases with a small slope till 0.7 at the control bandwidth of 10Hz.

6.1.3 Outer-loop design

Now that the inner-loop is closed, the outer-loop can be designed. The open-loop transfer function of the outer-loop is

$$L(s) = C_{PID}(s) \cdot T_{IL}(s) \cdot \frac{1}{s} \quad (6.6)$$

The integrator needs to be added to get from velocity to position, and is just mathematical. In the real system, only position output is available, and the velocity for the inner-loop needs to be differentiated.

The PID controller in the outer-loop is designed similarly as before. A unity closed-loop response is still desired, however in reality this is not possible. The method for determining k_p is the same as with the inner-loop, the proportional action is sized such that the open-loop unity-gain cross-over frequency matches the control bandwidth of 10Hz.

The outer-loop is a second order system and derivative action is required to add phase lead and damping at the unity-gain cross-over frequency. A "rule of thumb" is to let

the directive action start at a frequency which is 3 times lower than the cross-over frequency, this is described with

$$k_d = k_p \cdot \left(\frac{3}{f_c \cdot 2\pi} \right) \quad (6.7)$$

The derivative action will increase the loop-gain. Therefore, the k_p needs to be divided by a factor 3 to get to the same cross-over frequency.

The derivative is tamed, meaning that it is only working around the cross-over frequency. This taming provides a steeper roll-off and limits the control effort at higher frequencies. The differentiation action is terminated at 3.3 times the cross-over frequency. This is described with.

$$k_{dt} = \frac{k_d}{3.3(f_c \cdot 2\pi)s + 1} \quad (6.8)$$

The integration action is determined exactly the same as before by letting the control action stop a frequency 10 times lower than the control bandwidth, this results in $k_i = k_p \cdot 6$.

The full PID controller is then,

$$C(s) = k_p + k_{dt}s + \frac{k_i}{s} \quad (6.9)$$

This loop is closed just like the inner loop.

$$T(s) = \frac{L(s)}{1 + L(s)} \quad (6.10)$$

Figure 6.4 shows the frequency response of the outer-loop. The cross-over frequency is at 10Hz as designed, with a phase margin 100 degrees. The control parameters are shown in Table 6.2.

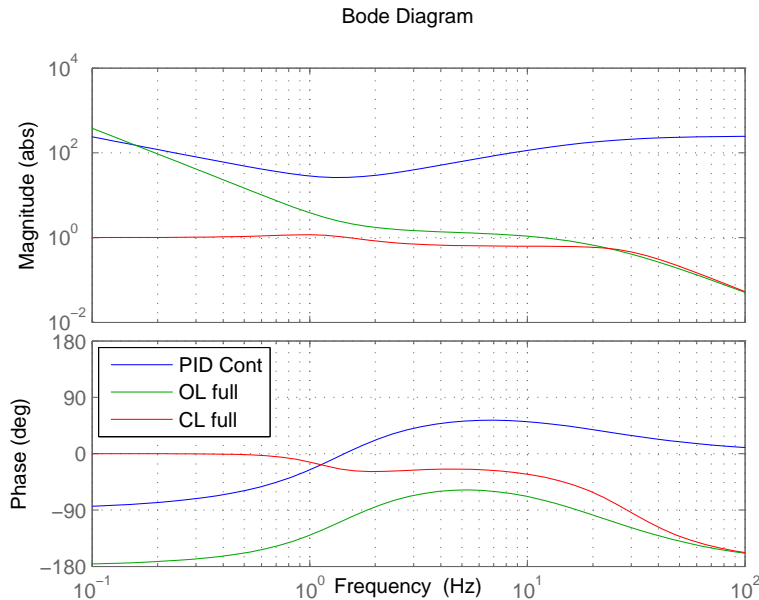


Figure 6.4: Bode plot of the controller, open and closed-loop of the full system. By using the "rules of thumb", the controller is tuned for a high phase and gain margin and a high low frequency gain. The closed-loop bode plot can track the reference till at least 10Hz.

Table 6.2: Outer-loop PID values for a control bandwidth of 10 and 1Hz

Control bandwidth	10Hz	1Hz
k_p	25	4
k_d	1.2	1.9
k_i	150	2.4

6.2 System identification

To see how well this simplified model corresponds with the actual stage, system identification was used. This was done by performing a frequency analysis with the use of an open-loop sine sweep.

To measure the "real" displacement of the mover a reference sensor was used. The MICRO-EPSILON optoNCDT 1402-5 was selected, the datasheet is shown in Appendix B.3. This is an analog position sensor, it uses laser triangulation to measure the position. In combination with the niDAQ data acquisition unit, the sensor noise was measured and shown in Appendix A.9. The (3σ) measurement precision of the sensor is $0.42\mu\text{m}$, when a lowpass filter with a cut-off frequency of 10Hz is used. The measurement setup is shown in Fig.6.5.

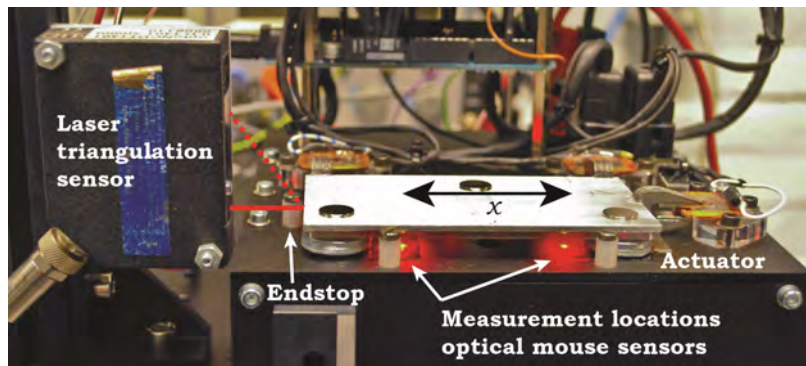


Figure 6.5: A laser triangulation sensor is used to measure the displacement of the stage in one DOF. The laser light is reflected on the side of the mover. During this measurement the optical mouse sensors are also measuring.

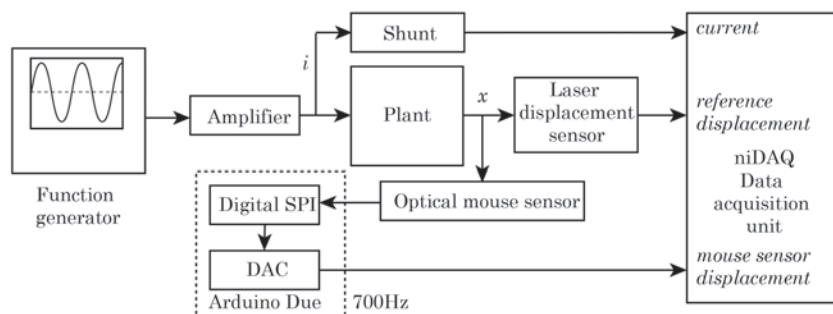


Figure 6.6: Schematic of the measurement setup. A sine generator controls the amplifier and actuators. With a shunt the current is measured. The displacement of the mover is measured by the laser displacement sensor as reference. The signal from the optical mouse sensor is also turned into an analog signal for comparison. These signals are logged by the data acquisition, so that it can be processed on the computer. Note, that this is a more extensive setup, than the one discussed in Section 5.3.5

A function generator was used to generate a sine with an increasing frequency. This signal was propagated through the amplifier to supply the actuator with current. A shunt resistor in series with the coil was used to measure this current. The displacement was measured by the laser triangulation sensor and the optical mouse sensors. The signal from the optical mouse sensors is digital and was processed by the Arduino first. After a digital to analog conversion on the Arduino, the signal was fed into the data acquisition unit. This is shown in Fig.6.6

The results are shown in Fig.6.8a. A sweep from 0.1 to 100 Hz was performed. The red line is the current, the green line is the reference sensor and the blue line is the mouse sensor. The figure shows that with increasing frequency the amplitude of the optical mouse sensor decreases faster than the reference sensor.

To extract more information, a fast Fourier transform (FFT) is used to convert the signal from the time domain to the frequency domain. The bode plot can then be obtained by dividing the different signals over each other and calculating the phase between these signals. This is shown in Fig.6.8b and 6.8c respectively.

The blue line was obtained by dividing the FFT of the mouse sensor over the FFT of the input. This is the magnitude bode plot of the optical mouse sensor and shows some bouncing behavior. These bounces are found in finite impulse response (FIR) filters which are found in digital data processing applications[18]. The phase of the optical mouse sensor starts at the expected -90 degrees damping line and it rolls over -180 degrees at around 2Hz.

When zooming in the time domain plot these little FIR filter bounces can be observed and is shown in Fig.6.7. The signal get smaller and smaller with increasing frequency, till the amplitude is almost zero. Then, with increasing frequency it starts to increase again.

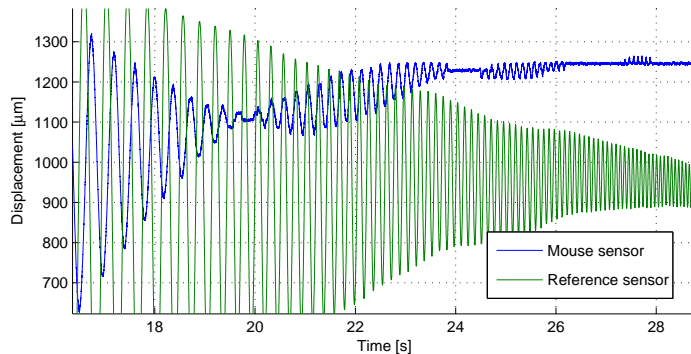
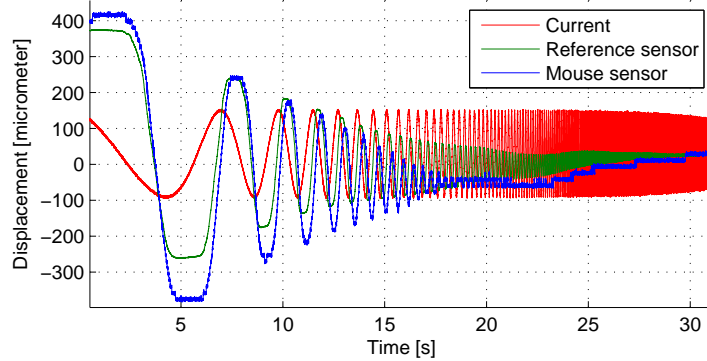
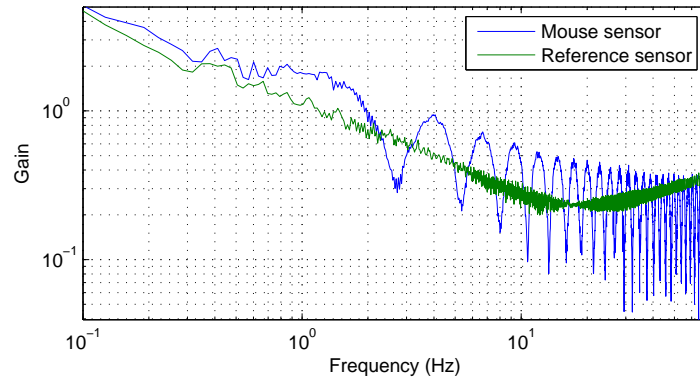


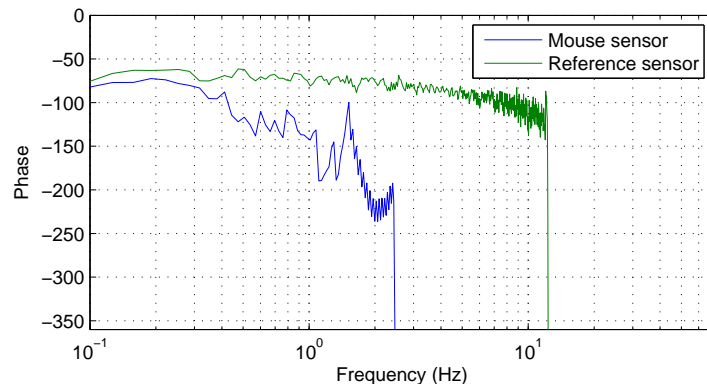
Figure 6.7: This figures shows the digital filter bounces when zooming in on Fig. 6.8a. The frequency of the input signal is increasing, while the amplitude of the displacement is decreasing. The amplitude of the optical mouse sensor reaches zero till it starts moving again while the frequency is still rising.



(a) Sinesweep with increasing frequency in the time domain. Green is the laser triangulation sensor and should represent the movements of the mover on these low frequencies. The blue line is the mouse sensor measuring the mover



(b) The openloop amplitude bode plot, the blue line is the mouse sensor, the green line is the reference sensor. When looking at the blue line small bounces can be observed which are typical for digital filters.



(c) The openloop phase, both phases start at the expected -90 damping line. The optical mouse sensor starts to drop below the -180 at around 1.5Hz.

Figure 6.8: The validated open-loop frequency responses of the planar stage plant, without controllers.

To check if this digital filter can be reproduced, the reference signal was filtered and compared with the optical mouse sensor. An arbitrary step was made with the stage and the position was measured with the reference and optical mouse sensor. Then a moving average filter with a cut-off frequency of 3.5Hz was used to filter the reference signal. Figure 6.9 shows this step response and shows that this 3.5Hz moving average filter overlays well with the sensor dynamics of the optical mouse sensor.

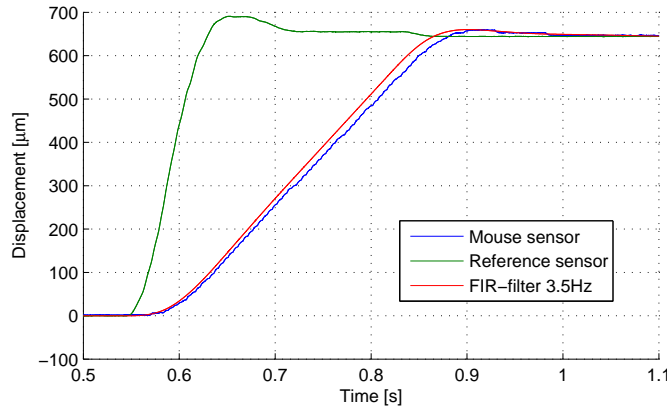


Figure 6.9: A measured step response of the stage. The red line is obtained by filtering the green reference signal. If the red line has a good overlay with the optical mouse sensor, it means that a comparable filter is implemented in the optical mouse.

Updating the model

It seems to be that a heavy digital filter is integrated in optical mouse sensors. To see what effect this filtering has on the system the system is discretized with a sampling frequency of 700Hz. Then the sensor dynamics are added by modeling it as a FIR filter,

$$H_{sens} = \frac{1}{n} \frac{z^n + z^{n-1} + z^{n-2} + \dots + z^2 + z^1 + 1}{z^n} \quad (6.11)$$

where n is the amount samples, this can be determined from the cut-off frequency and the sampling frequency.

$$n = \frac{f_s}{f_c} \quad (6.12)$$

These sensor dynamics are included by adding them to both feedback loops

$$T_{IL}(s) = \frac{L_{IL}(s)}{1 + L_{IL}(s)H_{sens}} \quad (6.13)$$

$$T(s) = \frac{L(s)}{1 + L(s)H_{sens}} \quad (6.14)$$

The bode plot of the system including this filter on the sensor output, is shown in Fig.6.10.

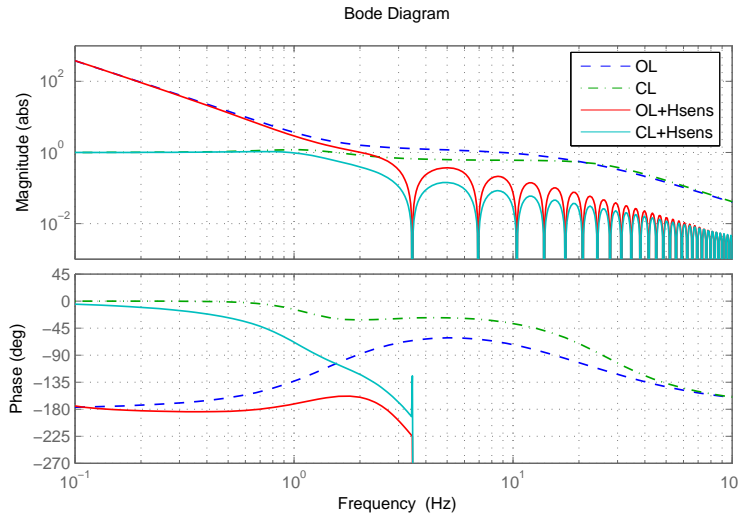


Figure 6.10: The bode plot of the discretized full system including the digital filter.

The model is rebuild in Simulink and extended to 3DOFs, by adding torques based on forces and geometry. This model also gave the possibility to test the force transformation and to add the force and velocity saturation. Then with the FIR filter block the sensor dynamics are included. The controllers are implemented with the previously obtained control parameters discussed in Table 6.2.

With this model it was possible to obtain a simulated step response, which is shown in Fig.6.11. It is clearly visible that the system is unstable with a 10Hz control bandwidth. The control bandwidth is reduced by a factor 10 to 1Hz due to the -180 phase lag at 2Hz of the optical mouse sensor. Resulting in a settling time (95% of the reference value) of 1.5 seconds. Without this phase lag in the mouse sensor the system has a settling time of 0.5 seconds.

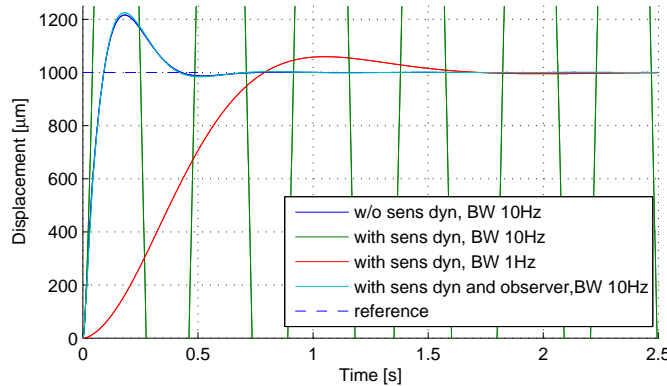


Figure 6.11: Simulated step response. A controller with a control bandwidth of 10Hz is unstable. The system was stabilized by decreasing the control bandwidth to 1Hz with the control parameters shown in Table 6.2. This gives a much slower step response with a settling time going from 0.5s down to 1.5s. With an observer to cancel out the sensor dynamics a controller with a control bandwidth of 10Hz can still be stable as shown with the cyan line. The observer design is discussed in the next section.

6.3 Model based observer

To increase the control bandwidth an observer has been designed. So instead of using filtered and delayed information for the controllers. An observer is used to estimate the position and the velocity. The observer does this by using the current control input, the optical mouse signals and the information about the whole system including sensor dynamics to estimate the actual movement of the mover. With an accurate estimation it is much easier to control the mover[19].

The velocity observer is shown in Fig.6.12. The observer uses two inputs, the control input of the force and the measured velocity signal. The actuation force and other system forces such as damping forces are summed up to a net force and divided by the mass. This estimated acceleration is integrated to get an estimated velocity.

The estimated velocity is now determined with pure feed-forward, and is only true if the systems behaves exactly like the model. This is of course never true in reality, therefore the estimation is compared with the measured value from the optical mouse sensors and the error between these signals fed back into the observer. If these signals are directly compared they will be off, due to the sensor dynamics in the optical mouse sensor. Accordingly, are included in the model by applying the same FIR filter on the estimated velocity signal. This estimation error is multiplied by a feedback gain, which determines the stiffness of the observer feedback loop, and is fed back before the integrator.

The same was done for estimating the position. For the position observer the estimated velocity and the measured position from the optical mouse sensors are used. This observer is easier since only an integrator is needed to get the position from the velocity. The feedback loop is similar as the velocity observer.

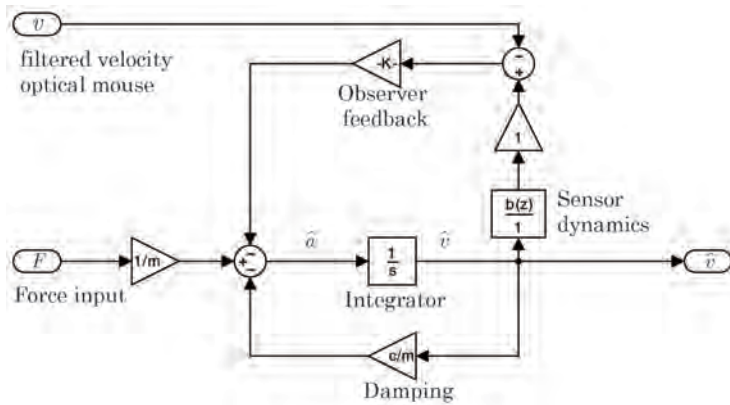


Figure 6.12: Velocity observer, the force control input is used to estimate the acceleration. By integrating this acceleration the velocity is estimated. By propagating this estimated velocity through the sensor dynamics, the error on the velocity estimation is determined. The observer feedback tries to reduce this error by subtracting it before the integration.

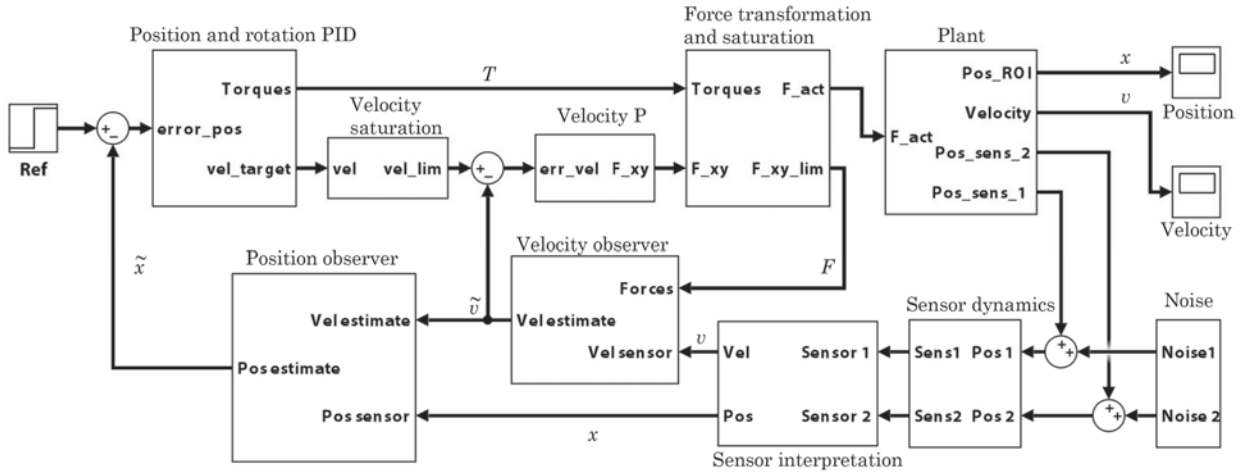


Figure 6.13: The updated 3DOF model with sensor dynamics and observer in Simulink. The position controller uses the position estimation from the position observer to control the velocity. The same goes for the inner-loop which uses the velocity estimation from the velocity observer. This observer should compensate for the sensor dynamics.

6.4 Implementation

To meet the requirement for low cost electronics, the full control scheme is implemented on an Arduino Due. The programming was done manually and the programming structure is discussed in this section.

6.4.1 Structure

The communication with the Arduino is over the serial bus and can be done with any serial communication programs. In the opensource Arduino software, this serial communication is also included. For the Arduino code a structure has been developed which works on identifying strings. Which means that a set of predefined functions can be called. For example when the text "zero" is entered, the Arduino will recognize the text and follow the routine for zeroing. The most important command is the motion control function, this is based on the Simulink model shown in Fig.6.13, all blocks are coded as a function. The structure and the motion control scheme are shown in Appendix A.6. The rest of the code will not be discussed in this thesis and can be found in the digital files in the archive.

6.4.2 Control parameters

After implementing the controller on the Arduino it was clear that the model didn't match the real stage. This is especially troublesome for the observer, resulting in a large estimation error. Increasing the observer feedback loop by too much made the stage unstable. Therefore, an integration action was added to the observer feedback loop, so that the error could be reduced. However, this made the step response slower, because the estimation error needs to be corrected by the integrator. The final control and observer parameter values are shown in Table 6.3.

Table 6.3: Controller and observer parameters for the x direction after fine-tuning

Controllers	Value	Observer	Value
k_{p-IL}	25	G fb vel obs	60
k_{i-IL}	100	I fb vel obs	300
k_p	20	G fb pos obsr	12
k_d	7.5	I fb pos obs	5
k_i	1000		

6.4.3 The Y and rotation DOFs

Until now, only the controllers for the x-direction have been implemented. During the project, the choice was made deliberately to focus on the optimization of the performance in one DOF, rather than having all the three DOFs operating. The increase of performance is in my opinion a challenge which is more scientific and analytic, than getting all three DOFs to work. The three DOFs are already modeled in Simulink and the Arduino controller is build such that the y-axis can be easily added. However, the rotation controller needs to be tuned which can take some time.

6.4.4 Difficulties

The blocks in Simulink look easy, because most of it was already pre-programmed. Programming all these different controllers and observer schemes took a lot of time. To achieve a high loop speed, the calculation time should be reduced. This was done by using only integer math without floating point numbers. Meaning that small numbers had to be multiplied by large factors, without overflowing the 4 bytes of an integer. Monitoring all these multiplications is important so that the variables still make sense. Other difficulties were the lack of good overview such as in Simulink, the sensitivity to typos, the long flash time (20 seconds) and difficulty to probe all variables.

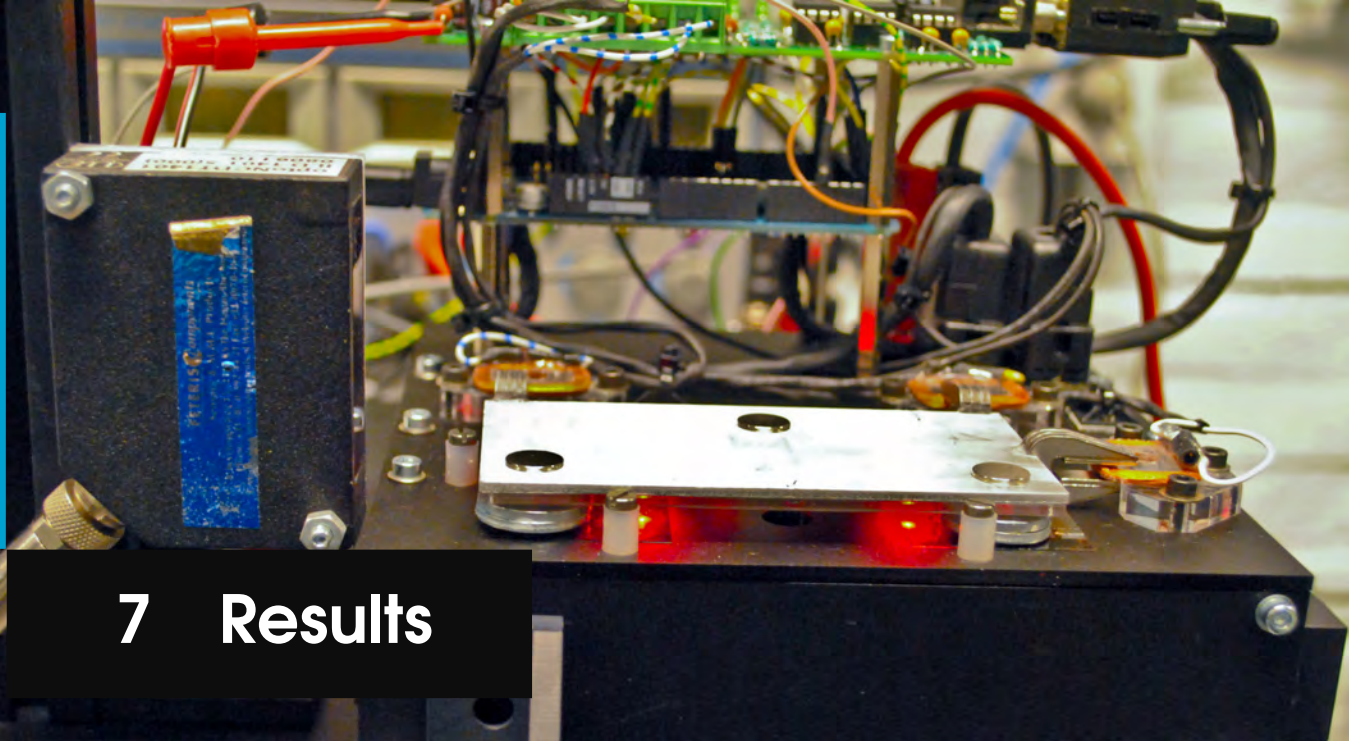
6.5 Conclusions

To ensure that the optimal tracking velocity of the optical mouse sensor is not exceeded a cascaded position-velocity controller has been designed. This control scheme can limit the speed of the mover, while a conventional PID controller cannot.

The dynamic behavior of the optical mouse reduces the possible control bandwidth to only 1Hz. This behavior was experimentally revealed and is caused by a heavy digital filter which is integrated in the mouse sensor. This digital filter has a cut-off frequency of 3.5Hz and introduces a large phase shift which rolls-off the -180 degrees at around 2Hz.

The control bandwidth has been successfully increased with a factor 10 by designing a model based observer, to cancel out the phase lag of the sensor. The observer uses information about the model, sensor dynamics, system inputs and optical mouse sensor output, to estimate the state of the mover. So instead of controlling the stage with delayed information of the optical mouse sensors, the estimation on the "current" state are used. This improved the control bandwidth from 1 to 10Hz.

During implementation, it became clear that model and reality were still a bit off, resulting in an estimation error, which introduced instability. By fine-tuning the controller and observer parameters and introducing an integral term in the observer feedback, the stage was stabilized with a control bandwidth of 10Hz. Everything was successfully implemented on an Arduino, which proved to be a big challenge.



7 Results

After tuning the controllers the results can be obtained. First a step response is performed to determine the settling time. This step is then repeated so that the positioning precision can be determined. At last the position stability of the stage is observed when it is stable on its target.

7.1 Step response

The same reference sensor as in Section 6.2 is used to measure the displacements of the mover and to determine the accuracy, these signals are not used in the feedback control loop. Only the displacement signals of the optical mouse sensors are used in the closed-loop controller on the Arduino to position the mover.

The results are shown in figure 7.1, the settling time (95%) of a 1mm step is 0.98 second. The first wavy part is a small oscillation in velocity around the velocity limit. Then at around 0.5 seconds the stage gets decelerated till a complete standstill, because the estimator has overshot the target. The integration part of the observer slowly reduces the estimation error and the movement is resumed.

This estimation kink took around 0.4 seconds, meaning that a better tuned controller and observer could end up well below 0.5 second, close to the step response of the simulation.

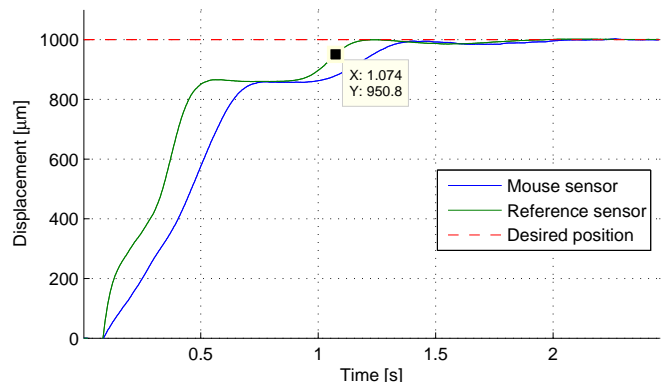


Figure 7.1: A measured closed-loop step response. Green is the reference sensor and the blue line is the optical mouse signal. The settling time (95%) is around 1 second. There are still some oscillations in the step, with a better tuned controller it can be faster.

7.2 Positioning precision

The position output of the reference sensor is compared with the desired target position. This means that measurement errors such as drifts, servo errors from the controllers and external disturbances are all included in the positioning uncertainty. To determine the repeatability, these steps are reproduced for multiple times. The stage is first calibrated and with these settings the step is repeated for 100 times to get an adequate data set. 5 of the 100 steps are shown in Fig.7.2. Between each step the stage is homed against the endstop and the mouse sensor is reset.

The position at the end of each step is taken, to determine the positioning error and can be visualized in a scatter plot, see Fig.7.3a. This figure shows that all errors are within $\pm 8\mu\text{m}$.

These positioning errors are also plotted in a normalized probability density function (PDF), see Fig.7.3b. The red line is the contour of a standard normal distribution with a mean of $0.5\mu\text{m}$ and a σ of $3.2\mu\text{m}$. These values are determined with the methods discussed in Section 3.1.4.

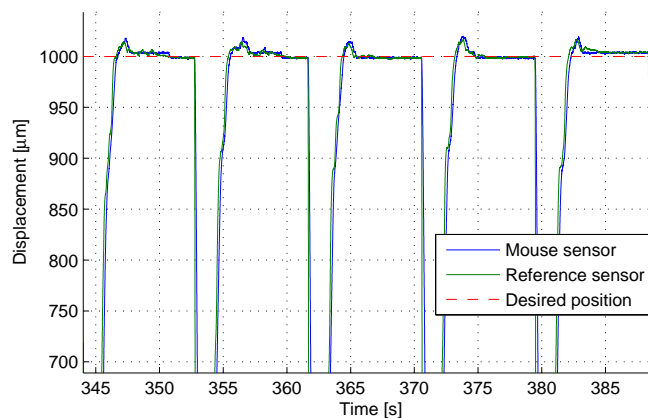
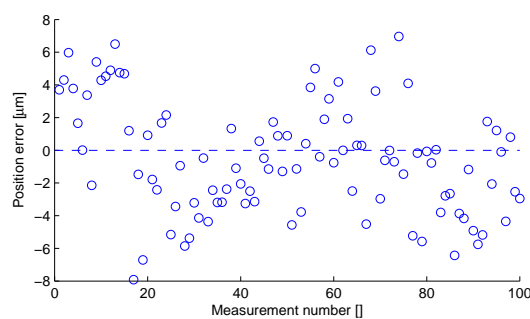
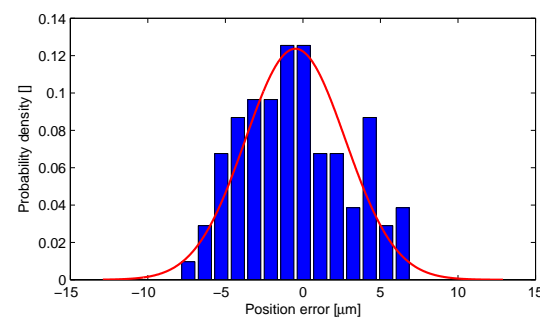


Figure 7.2: 5 of the 100 steps which were made during the measurement are shown. The stage is given a reference location where it should go to and with the external laser triangulation sensor the position is measured. This process is repeated so that the positioning accuracy and precision can be determined.



(a) Scatter plot of the position error for steps of 1mm. All errors are within $\pm 8\mu\text{m}$



(b) A normalized probability density function. The red line is the standard normal deviation with a mean of 0 and a σ of $3.2\mu\text{m}$.

Figure 7.3: The position uncertainty of the planar stage system.

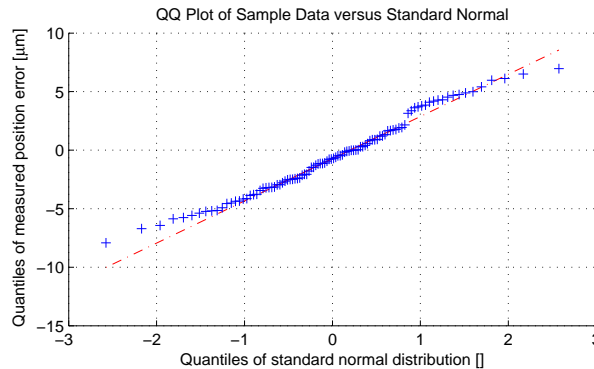


Figure 7.4: A Q-Q plot is used to compare how well the position errors matches the normal distribution. This is done by looking at how close the blue dots match the red line. It is linear and has the same slope. Meaning that the position error is normally distributed.

To check if the position is normally distributed, a Q-Q plot is made, see Fig.7.4. The plot is made by comparing the points in the PDF of the measured position error with the same points on the PDF of a standard normal distribution. The position error of these points are plotted on the Y-axis and the value of the standard normal distribution is plotted on the X-axis. Resulting in a straight linear line when the distributions match, while the slope tells something about the difference in σ .

This gives the positioning results as shown in Table 7.1. The mean error for this dataset is only 2.5 resolution steps off the target, with $0.5\mu\text{m}$. The 3σ precision is $9.7\mu\text{m}$, meaning that 99.7% of the steps will fall within the range of $\pm 9.7\mu\text{m}$.

Table 7.1: Positioning performance of the planar stage system

Results	Value
Measurement size	100 samples
Resolution	$0.16\mu\text{m}$
Mean error	$-0.5\mu\text{m}$
Precision (3σ)	$9.7\mu\text{m}$

However, this mean error is only valid when the stage is calibrated recently. A method to calibrate the stage without the reference sensor was shown in Section. 5.4.2.

7.3 Positioning stability

Next to the stepping motion, the positioning stability is also an important parameter. This positioning stability includes the measurement stability, servo stability and the disturbances.

The mover is positioned at a target location, the reference sensor is used to measure the mover's location over 240 seconds. A PDF of the error is shown in Fig.7.5. The 3σ positioning stability is $3.1\mu\text{m}$. This means that 99.7% of the time the mover stays within $\pm 3.1\mu\text{m}$ of it's target.

The error is normally distributed and symmetric meaning that the sensor is not drifting away at low speeds and that the controller is capable in keeping the mover at the desired target position.

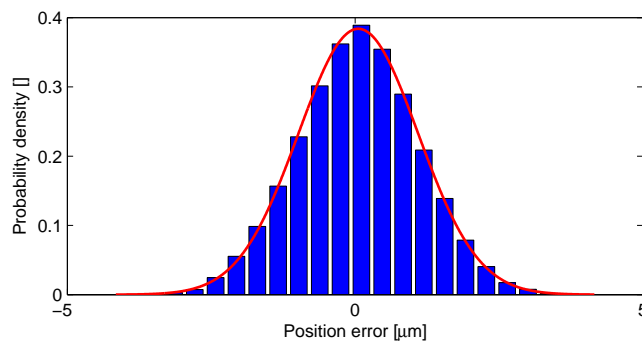


Figure 7.5: A normalized probability density function of the position error, once the stage is stable on its reference

7.4 Constant sensitivity

To see how constant the sensitivity of the sensors are, different step sizes are performed and compared with the their reference value. This is shown in Fig.7.6. Steps from 1000 to 4000 μm are performed and no variations in sensitivity could be observed. The tests are only performed till 4000 μm because the reference sensor only has a range of 5mm, making the last part of a potential 5th step out of range.

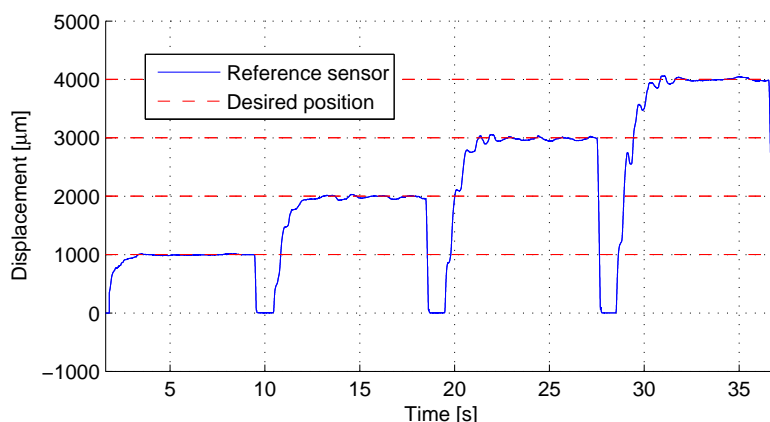


Figure 7.6: Steps with different step sizes were made to check for constant sensor sensitivity, after every step the stage is zeroed at its endstop. The sensor sensitivity was constant and the controller was stable for all those four different step sizes.

7.5 Conclusions

The planar stage system shows that it is capable of positioning with a 3σ precision of 9.7 μm and a settling time of 1s. Furthermore, the sensitivity with different displacement was constant and the controller was stable. Proving that it is possible to reach micrometer precision with a simple low cost system.



8 Conclusion

To look for the possibilities of decreasing the cost of precision stages. A low cost planar stage system with optical mouse sensors has been successfully designed, realized and validated. This system has a 3σ precision of $9.7\mu\text{m}$ and a resolution of $0.16\mu\text{m}$, which is for the €200,- of component cost a good result. The performance of the system is mainly limited by the optical mouse sensor. How these performance limiting challenges have been overcome to get to this final performance, is discussed in the following conclusions.

The optical mouse sensor integrates the displacements to obtain the position. During this integration small errors are accumulated to large integration errors, making the sensor inaccurate. This is solved by using a homing procedure between every step to reset the integration error. Resulting in a position sensor with limited drift, measurements proved that with a step of 1mm a measurement precision (3σ) of $2.7\mu\text{m}$ could be achieved, meaning that 99.7% of the measurements is between $\pm 2.7 \mu\text{m}$ of 1mm.

Another issue with the mouse sensor is the non-constant sensitivity as function of the displacement. The sensitivity decreases with smaller displacements, while with larger displacement the sensitivity is constant. By introducing an optical magnification the non-constant sensitivity for small displacements is removed, because the mouse sensor "see" the magnified displacement. Additionally, the resolution of the optical mouse sensor can be increased from $2.5\mu\text{m}$ to $0.16\mu\text{m}$.

Due to the magnification the maximum tracking speed decreases. Therefore, a cascaded position-velocity controller has been designed. With this control scheme it is possible to saturate the speed and stay within the maximum tracking speed of the optical mouse sensor, which is not possible with a conventional PID controller.

The dynamic behavior of the optical mouse reduces the possible control bandwidth to only 1Hz. This behavior was experimentally revealed and is caused by a digital filter which is integrated in the mouse sensor. This digital filter has a cut-off frequency of 3.5Hz and introduces a large phase shift which rolls-off the -180 degrees at around 2Hz.

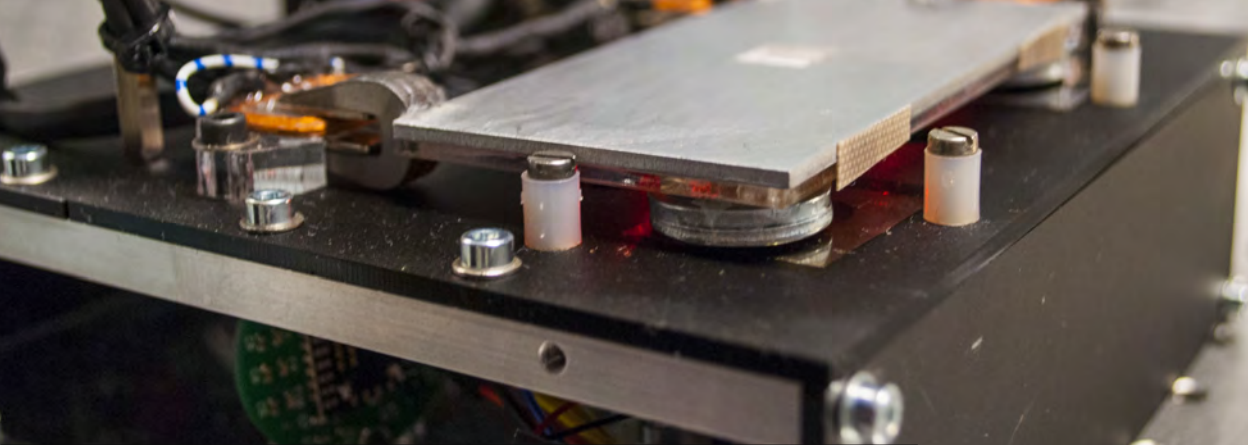
The control bandwidth has been successfully increased with a factor 10 by designing an observer, to cancel out the phase lag of the sensor. The observer uses information about the model, sensor dynamics, system inputs and optical mouse sensor output, to estimate the state of the mover. So instead of controlling the stage with delayed information of the optical mouse sensors, the estimation on the "current" state are used.

This improved the control bandwidth from 1 to 10Hz.

In line with the low cost requirements, a cheap microcontroller is used to control the system. The full controller, observer, sensor read-out and amplifier were implemented on an Arduino. Furthermore, no expensive lab equipment is used to control the planar stage system. Only a laptop with open-source software and a 12V adapter is needed to operate the system.

With all these challenges it was still possible to realize a system with a repeatability of $9.7\mu\text{m}$ for steps of 1mm, with a settling time (95%) of 1.0s. The 3σ positioning stability once it has settled is $3.1\mu\text{m}$. The controller is stable for different stepsizes and the sensitivity remains constant. When the stage is used as a region of interest tracker, the 3σ measurement precision is 0.1% of the traveled distance.

Summarizing, it can be concluded that the maximum possible performance of the planar stage system was achieved with the selected extreme low cost optical mouse sensor as position sensor. The integration of this sensor system was only possible with all the above mentioned methods and design considerations. This was all done with a component cost of €200,- in a time frame of 1 year.



9 Recommendations

When the full system is compared with commercially available stages, it is still lacking in performance due to the drift and heavy filtering in the optical mouse sensor. Therefore, some recommendations can be given on how the system could be improved.

The performance of the stage is currently limited by the optical mouse sensors. Development in PSD sensors and 2D grid encoders in the MSD group are very promising since they have a higher bandwidth and positioning precision. The combination of such a measurement system with the rest of the demonstrator stage could give a system which is still cost effective and has a higher performance.

The optical mouse sensor was selected for its high resolution, it is proven that the current resolution is more than enough. However, drift and the dynamic performance are the main problem, it could be possible that there is a trade-off between these characteristics. Choosing an optical mouse sensor with less phase lag and drift could be a good alternative. The possible loss in resolution can be compensated with higher magnification factors, since the maximum magnification is two times higher than the currently implemented magnification. However, this could be a time consuming process since these characteristics are not mentioned in the specifications by the manufacturer, which means that they have to be determined experimentally.

If the unprocessed mouse signals could be made directly available on the same speed as it is currently being processed internally, an alternative algorithm can be developed specifically for precision positioning instead of normal everyday mouse tracking. This could have a great potential to improve both the dynamics as the precision.

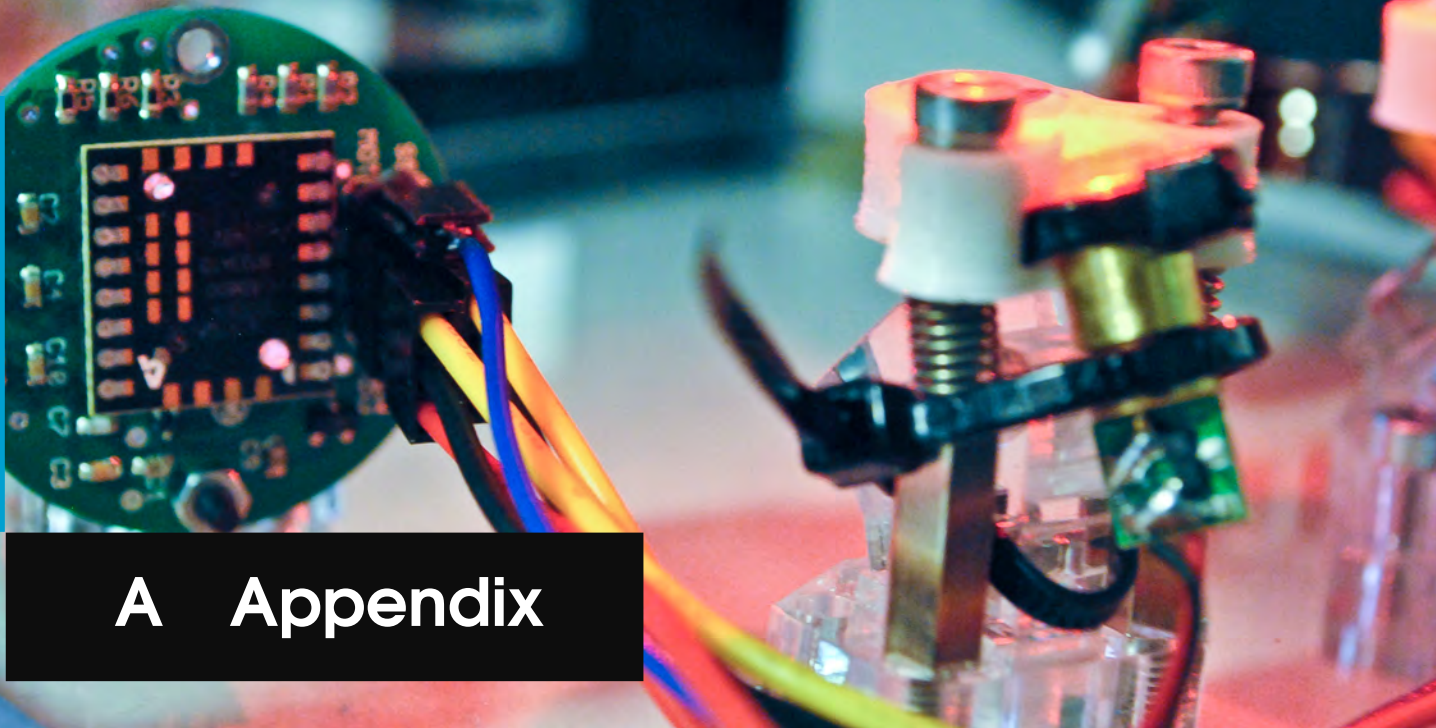
The current stage needs to reset its integration error at the home position. This procedure could be replaced by adding a webcam or camera to the system. This system can be incorporated in the observer so that the drift in the mouse sensor can be corrected by the absolute measurements of the vision system. The requirements for such a vision tracking system in combination with the optical mouse sensor can be much lower. Since the measurements only have to be performed at a lower frequency.



References

- [1] L.M. Williams and R.S. Cherry. *Optical mouse*. US Patent 4,751,505. June 1988. URL: <http://www.google.com/patents/US4751505>.
- [2] TW Ng. “The optical mouse as a two-dimensional displacement sensor.” In: *Sensors and Actuators A: Physical* 107.1 (2003), pp. 21–25.
- [3] TW Ng and TL Cheong. “The optical mouse as an inexpensive region-of-interest position recorder in optical microscopy.” In: *Microscopy research and technique* 63.4 (2004), pp. 203–205.
- [4] K. Lee and D. Zhou. “A Real-Time Optical Sensor for Simultaneous Measurement of Three-DOF Motions.” In: *IEEE/ASME Transactions on Mechatronics* 9.3 (2004), pp. 499–507. ISSN: 1083-44351. DOI: 10.1109/TMECH.2004.834642.
- [5] Ping-Lin Wu, Shyr-Long Jeng, and Wei-Hua Chieng. “Least squares approach to odometry based on multiple optical mouse sensors.” In: *Industrial Electronics and Applications (ICIEA), 2010 the 5th IEEE Conference on*. IEEE. 2010, pp. 1573–1578.
- [6] Kazi M Hossain and Arif A Sohel. “Using Optical Mouse as a Position Feedback Sensor for AGV Navigation.” In: *International Journal of Mechanical & Mechatronics Engineering* 13.2 (2013).
- [7] TW Ng and KT Ang. “The optical mouse for vibratory motion sensing.” In: *Sensors and Actuators A: Physical* 116.2 (2004), pp. 205–208.
- [8] Michal Bachraty and Milan Žalman. “2D Position Measurement with optical laser mouse sensor.” In: *NSSS Slovakia*. 2010.
- [9] S. Juds. *Photoelectric Sensors and Controls: Selection and Application, First Edition*. Mechanical Engineering. Taylor & Francis, 1988. ISBN: 9780824778866. URL: http://books.google.nl/books?id=BkdBo1n%5C_oo4C.
- [10] Umberto Minoni and Andrea Signorini. “Low-cost optical motion sensors: An experimental characterization.” In: *Sensors and Actuators A: Physical* 128.2 (2006), pp. 402–408.
- [11] D. H. Hensler. “Light Scattering from Fused Polycrystalline Aluminum Oxide Surfaces.” In: *Appl. Opt.* 11.11 (Nov. 1972), pp. 2522–2528. DOI: 10.1364/AO.11.002522. URL: <http://ao.osa.org/abstract.cfm?URI=ao-11-11-2522>.
- [12] R. Munnig Schmidt, G. Schitter, and J. van Eijk. *The Design of High Performance Mechatronics*. IOS Press, 2012. ISBN: 978-1-60750-825-03.

- [13] M. Cafe. "Design of a 6 DOF nanometer ferrofluid stage." Unpublished, Master Thesis. 2014.
- [14] S. van Veen. "Ferrofluid Bearings." Unpublished, Master Thesis. Jan. 2013.
- [15] H.M.J.R. Soemers. *Design Principles: For Precision Mechanisms*. Herman Soemers, 2011. ISBN: 9789036531030.
- [16] P.A. Tipler and G. Mosca. *Physics for scientists and engineers*. W.H. Freeman, 2008. ISBN: 0-7167-8964-7.
- [17] Ned Mohan, Tore M. Undeland, and William P. Robbins. *Power Electronics. Converters, Applications and Design*. third. John Wiley and Sons, Inc, 2003.
- [18] E.W. Kamen and B.S. Heck. *Fundamentals of Signals and Systems*. Pearson, 2007. ISBN: 0-13-168737-9.
- [19] K.J. Astrom and R.M. Murray. *Feedback Systems, an introduction for scientists and engineers*. Princeton, 2008. ISBN: 978-0-691-13576-2.



A Appendix

A.1 Market research

There are dozens of different companies selling precision planar stages for microscopy. In table A.1 three stages from different companies. The price range starts at around €2000, and can get 3 times as high for higher specifications. The repeatability ranges from 0.25 to 5 μm .

Table A.1: Specifications of a 2 DOF precision stage from Zaber

	Zaber	Thorlabs	Optics Focus
Price [€]	4010	5915	1895
Resolution [μm]	0.15	0.1	1.25
Accuracy [μm]	12	<3	<5
Repeatability [μm]	2	0.25	<5
Stroke X // Y [mm]	100 // 120	110 // 75	100 // 100



Figure A.1: Three different commercial available planar precision stages for microscopy.

A.2 Laser rotation sensor

A method to measure the rotation of the stage is to double the amount of sensors. However there might be more efficient/cheaper ways. This appendix is a side project about a rotational sensor which could have been used on the demonstrator stage. The design was finished and didn't get implemented, because it wouldn't add anything to the research goal.

Working principle

The idea of the sensor is to use a laser spot on two photo diodes to determine the rotation of the stage. This concept is visualized in figure A.2. When the mover rotates with an angle α the angle between the reflecting and incoming beam is twice this angle α . When the distance l is known, this angle α can be determined when the translation β is known. Two photodiodes as shown in figure A.2b can be used to measure this translation β . The laserspot will translate to the left and right depending on the rotation of the mover. This means that the ratio of irradiance on the two photodiodes will vary. The photodiode are used in photoconductive mode or also known as reverse biased mode. The photocurrent is then linearly proportional to the current. This difference in current can be measured to determine the translation β , which is used to calculate the rotation of the stage.

$$\alpha = 0.5 \arctan \left(\frac{\beta}{l} \right) \quad (\text{A.1})$$

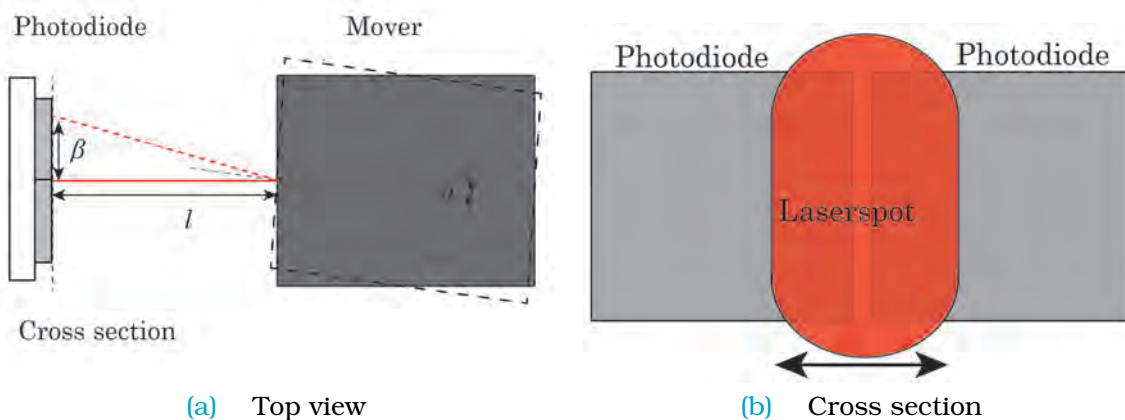


Figure A.2: Laser dot moves over the photodiodes when the stage rotates

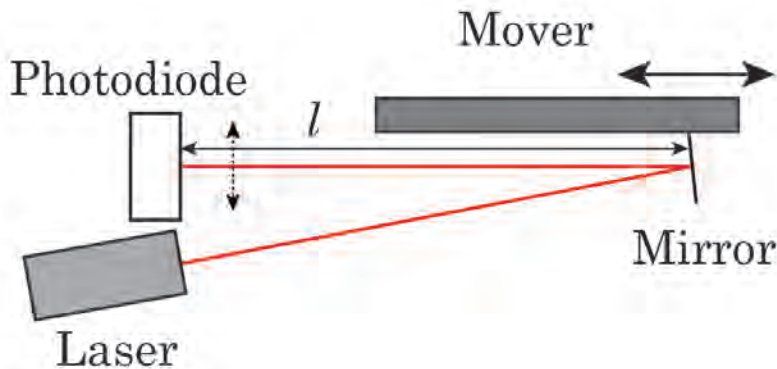


Figure A.3: Side view of the system, as can be seen the distance l is not constant because the stage can move in both planar directions. Therefore the sensor is used to keep the rotations small.

As can be seen in figure A.3, the distance l is not constant at all. This means that a change in gain will act on the sensor and that the laser spot can drift upwards and downwards. Since it's a difference measurement between the left and right photodiode, the upward shifting of the laser spot will not be noticed. But should be designed such that for the whole range of the stage the dots stays on the photodiodes.

The change in gain is for an absolute sensor difficult to cope with, since then the position of the stage needs to be integrated in the algorithm. However, looking back at what is required, the rotation only needs to be locked. So with a sufficient stiff feedback loop, the variation in gain is not important at all.

Figure A.3 also shows why the design didn't make it onto the stage. The alignment of all the parts is critical, such as the mirror on the stage which should be placed on half the angle between the laser and photodiode. To keep everything adjustable, very difficult and complex brackets were designed consisting of multiple parts. The sheer amount of alignment and assembly work didn't weight up since it's only a side track.

Electronic design

The electronic design was finished and is shown in figure A.4, it consisted of two transimpedance amplifiers to convert the current from the photodiode to a voltage. This voltage is then amplified by a differential amplifier. 1.65V is added to raise the voltage between 0-3.3V so that it is compatible with the Arduino. Protection circuitry with zeners should be added for over voltage protection of the Arduino, this is done with the amplifier.

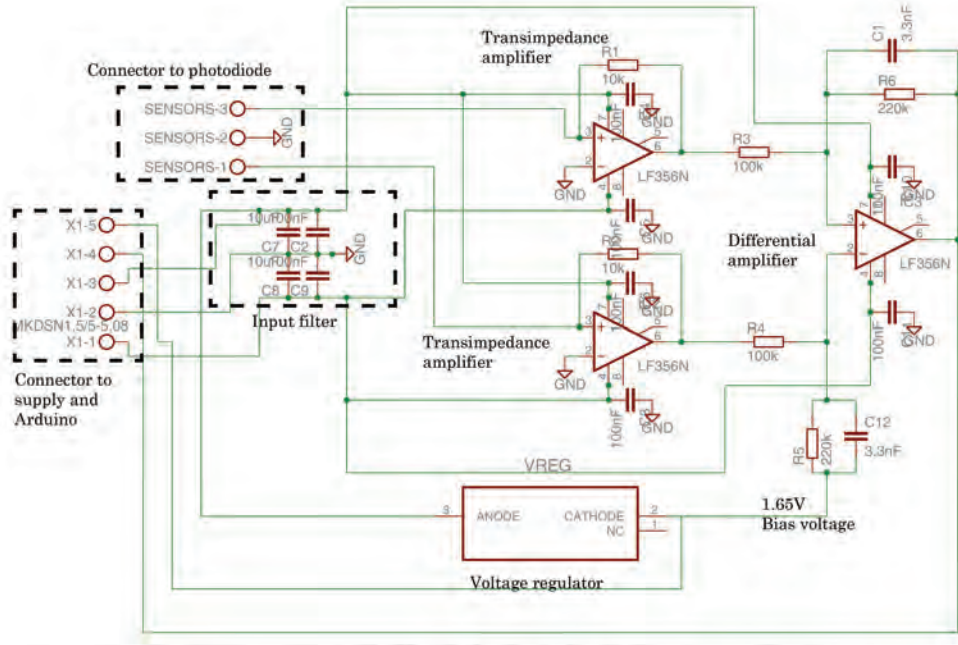


Figure A.4: Schematics of the amplifier board for the photodiodes

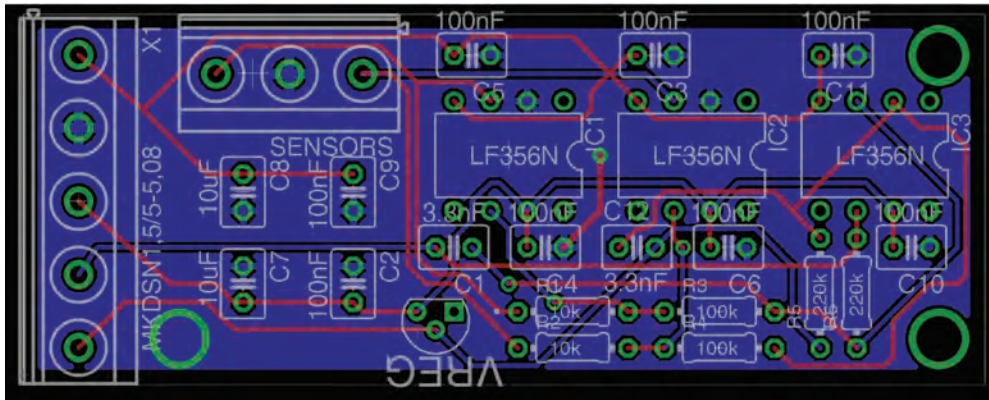


Figure A.5: Design of the print

The resolution of this sensor system is determined by its noise. From the datasheet it was possible to find the noise-equivalent power (NEP). Assuming a bandwidth of 100Hz the minimum detectable current will be around $4 \cdot 10^{-12} \text{A}$. Which translates to a minimum detectable translation of $5 \cdot 10^{-12} \text{degree}$.

Validation by a colleague, Paul Ouwehand

Paul Ouwehand, a fellow student who is working on a planar nanometer resolution pre-sliding stage, was interested in the sensor and wanted to implement it into his demonstrator stage. He build an experimental setup to validate the noise level to determine the resolution. The setup is shown in figure ???. A laser is put on a manual micrometer stage, and the photodiodes are stationary. The output of the amplifiers is put on a scope and the peak to peak value of the noise is determined. Then the manual stage is moved and the peak to peak value of the noise is then compared with the traveled distance to get the noise level in micrometers.

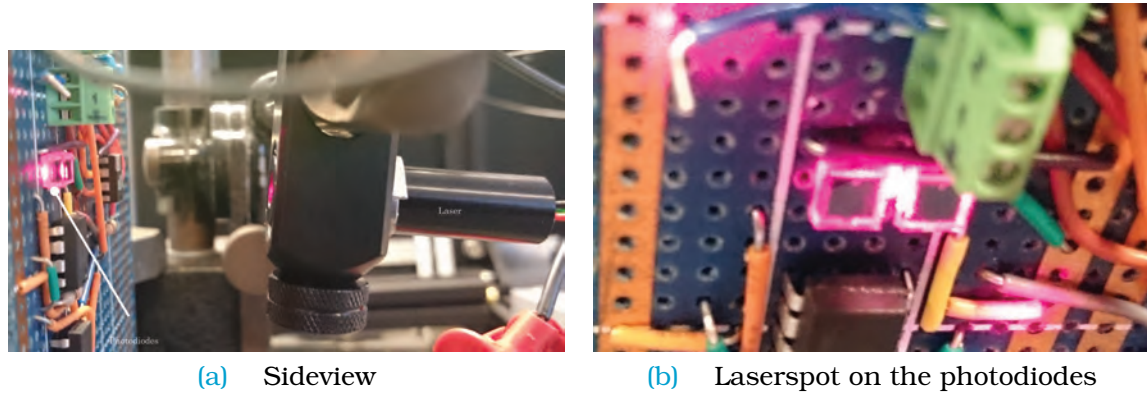


Figure A.6: Validation setup by Paul Ouwehand, the laser can move to the left and right(out of plane of the picture). By measuring the noise and comparing it to the displaced

The noise which could be measured is $0.5\mu\text{m}$ which means that with a 100mm l the noise in angle is only $4.4 \cdot 10^{-8}$ degree which is higher than the previously calculated value. This is because more error sources are in the circuit such as the laser, the resistors and the opamps. However, this resolution is much higher than the requirements. Meaning that they can be used to lock the rotation in a planar high precision stage. With these results, Paul will use them in his demonstrator stage and I am looking forward to see it's successful implementation.

A.3 Laser alignment

Alignment rig

The stage is designed such that the optics compartment can be removed from the stage. This is handy for the alignment of all components. Now that all parts have been produced and assembled, the distance between the measurement surface and the ground can be measured. An alignment rig can then be built according to this distance. Now all adjustment bolts and screw can be operated while the measurement surface is on the correct distance. The rig and how the optics compartment can be taken out is shown in Fig. A.7.

Alignment tools, photodiode

Aligning all the optics without feedback is hard. Therefore different tools were made such white paper targets to aim the lasers spots, additional mirrors and a photodiode to measure the irradiance.

The photodiodes from the rotation sensor were not used anymore. So one photodiode was put on a stick and wired to a transimpedance amplifier. This amplifier converts the current to a voltage. The output of the amplifier was put on the oscilloscope so that the irradiance can be read out as a voltage. By putting this photodiode in front of the assembled mouse sensors the light intensity could be measured. Furthermore, the irradiance on both the sensors could be compared and adjusted accordingly.

Surface quality parameter

The optical mouse sensors can output a variable which is surface quality. This number indicates how many individual surface details the sensor can detect. So aligning the optics while having the mouse sensor output this parameter is handy to get the alignment right.

Framecapture

As a last step it is possible to capture the frame of the sensor and visualize it. Letters with a fontsize of 1 or 2 needs to be printed on 1200 dpi on white paper. This can be put on the rig and if everything is in focus the letters should be distinguishable. This can be used as a last check.

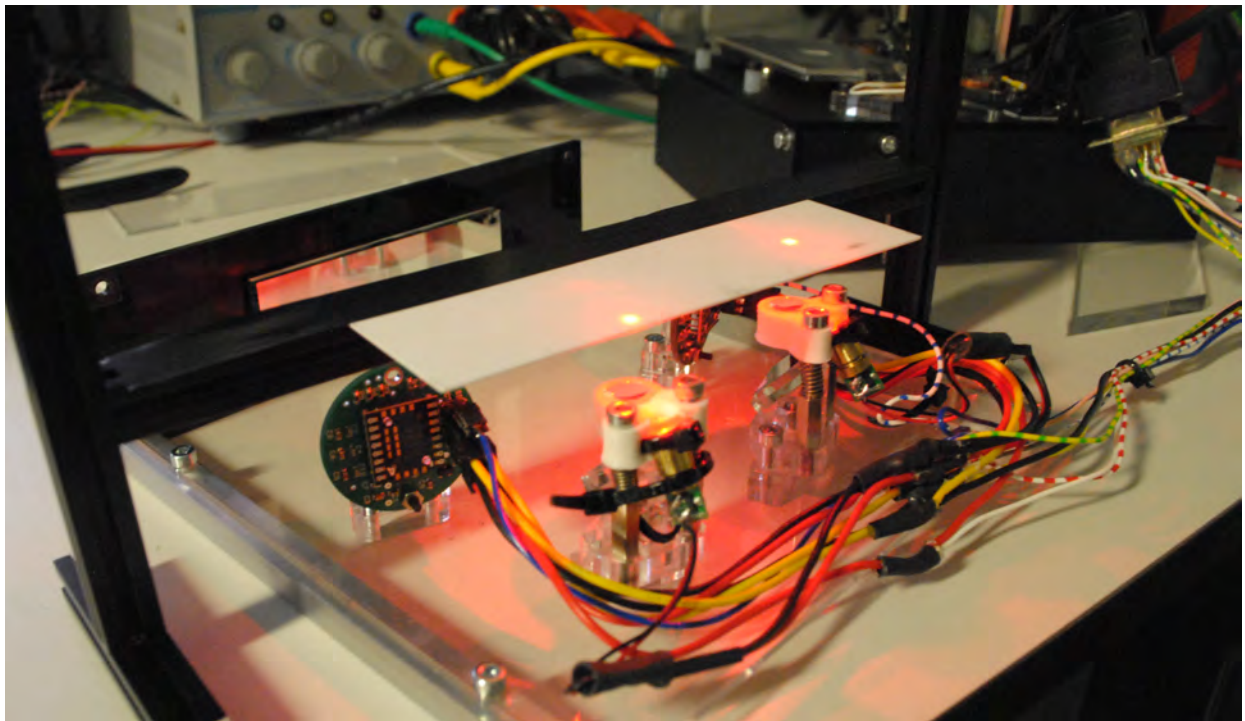


Figure A.7: This figure shows the alignment with the rig. The complete optics compartment can be taken out of the demonstrator stage with just 4 bolts. The rig with the white alumina is adjusted such that it has the same height as the mover. All the optical elements can be aligned.

A.4 Additional control concepts

Sensor delay compensation

The mouse has some sort of built-in delay. This delay can be averaged at about 50 ms. To compensate for this delay a Smith predictor can be used. An example of such a predictor is shown in figure A.8

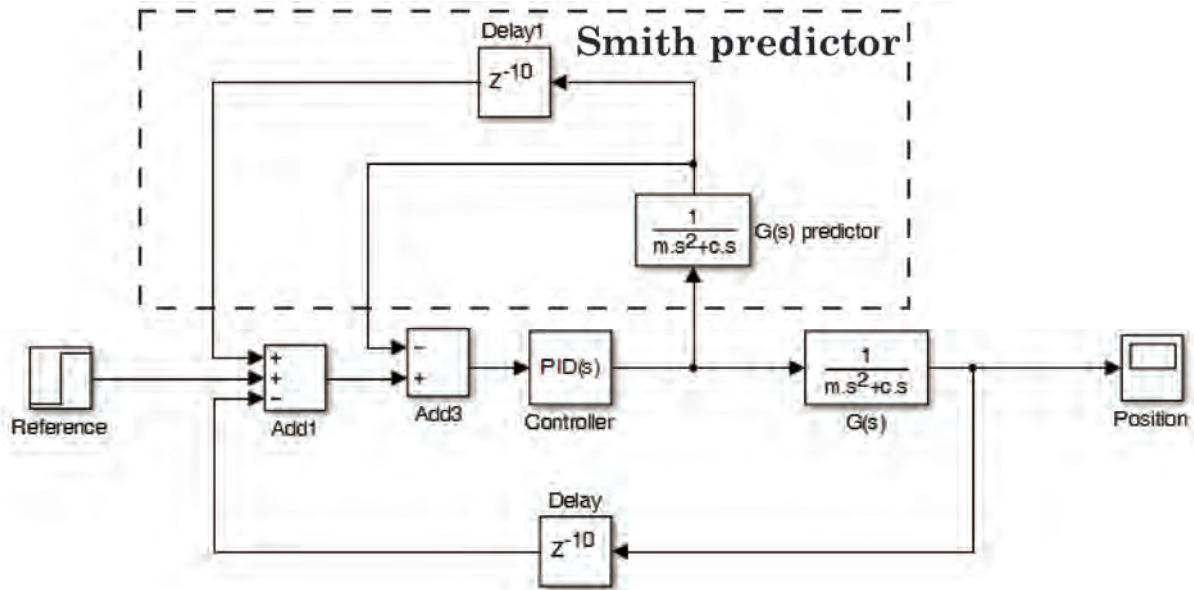


Figure A.8

The output of the controller is put on the plant, but also on a modeled plant. The output of this plant is then fed back to the controller and used to cancel the delayed signal. However the performance of such a filter depends heavily on the accuracy of the model. Applying this filter on the cascaded position velocity controller yields the following control scheme.

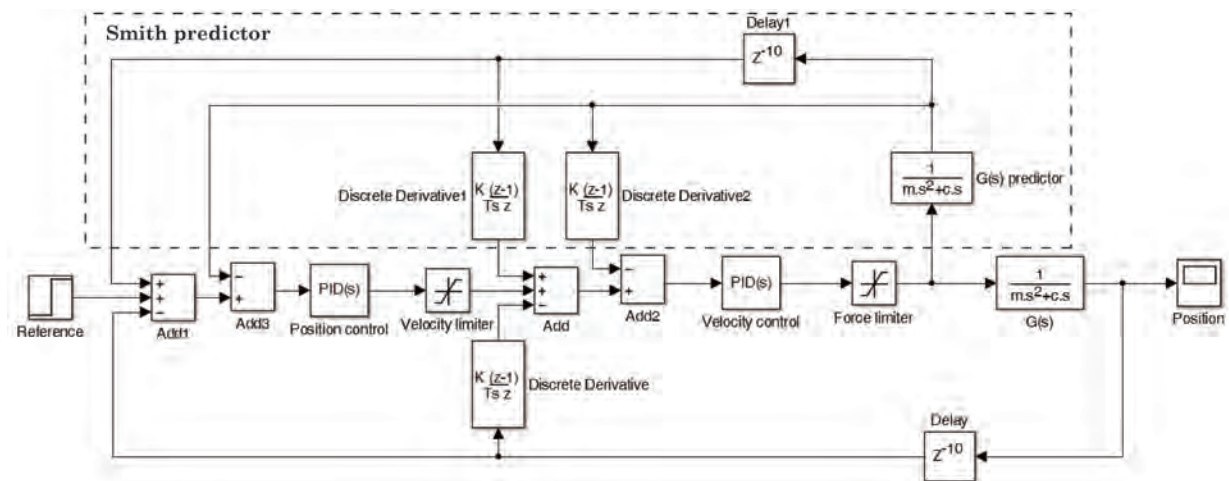
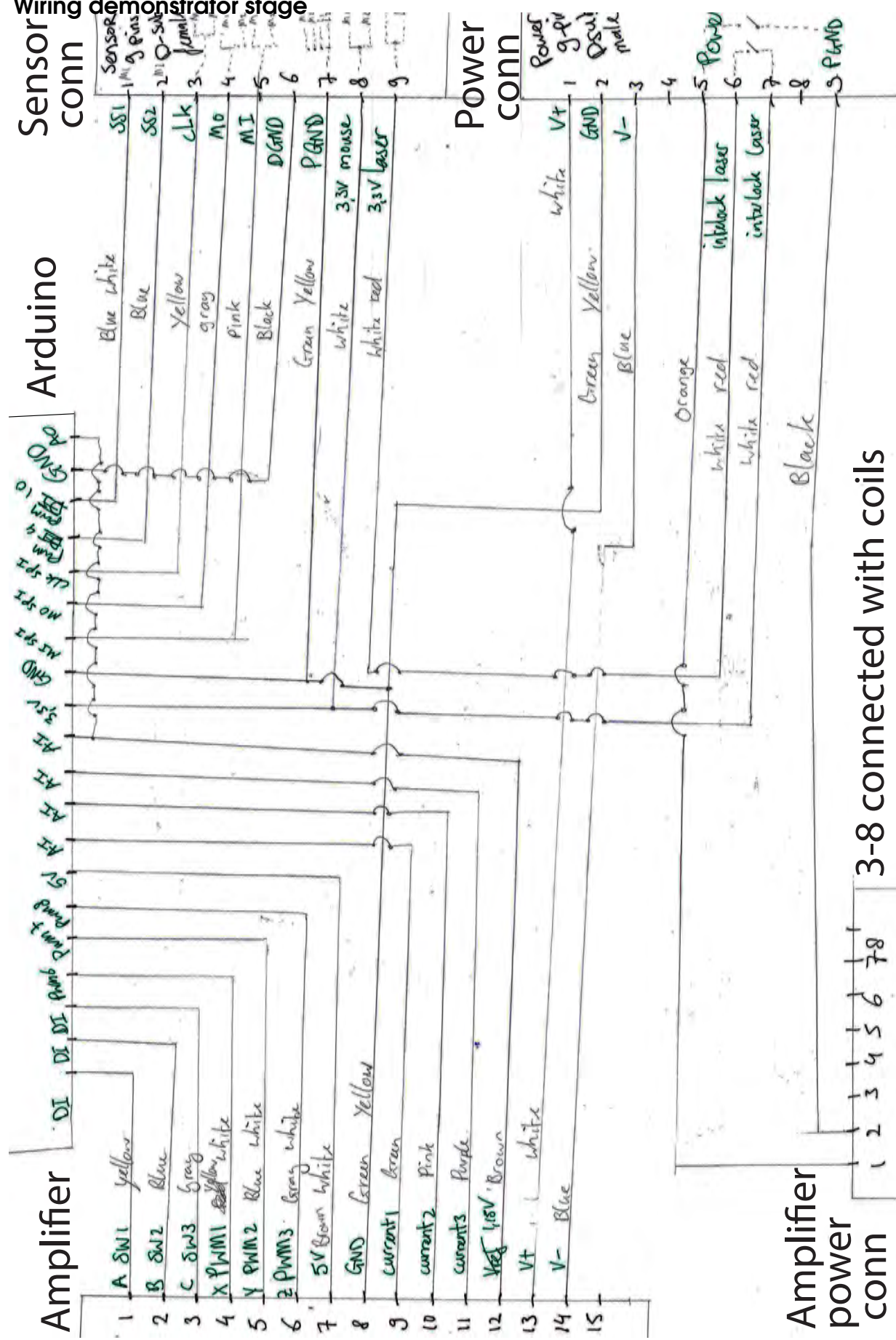


Figure A.9

This method was implemented and showed that it could stabilize the planar stage system. However due to the implementation of the observer, this method became obsolete. The estimation of the observer, is more accurate than the estimation of this method.

A.5

Wiring demonstrator stage



A.6 Arduino structure

The following table shows the different commands which can be given to the Arduino. The motion control code scheme is shown on the next page. For the full code and the functions, please refer to the digital files in the archive.

Table A.2: The programmed communication commands for the Arduino

Command	Meaning
move	Uses the controller to move the stage to a user defined position
zero	Moves the mover to zero and resets the mouse sensor values
config	Access the controller and observer parameters for rapid tuning
sine	Sinesweep while continuously measuring the position
test	Constantly changing test mode for small tests
position	Output the optical mouse sensor position
track	Continuously measure the position and output it
help	Gives an overview of all possible commands

```
void flow_move(){

    flow_zero(); // Home procedure, go to home and rest error
    read_input(); // Read out the desired moving position

    // Initialize
    prev = micros(); // Determine current time

    while (command != "stop") { // Continue till the stop function is triggered
        now = micros(); // Determine current time
        dt = now - prev; // Determine delta time for velocity and damping action

        // Sensors
        read_mouse(); // Read out mouse for feedback loop
        interp_sens(); // Sensor transformation matrix
        analogWrite(DAC0,x[0]*3.3*100/10000); // write position through DAC for
                                                // validation
        vel(); // Differentiate position to velocity
        observer(); // Estimate position

        // Outer-loop
        error_p(); // Determine position error between estimation and reference
        PID_pos(); // PID outer-loop controller
        saturation(); // Velocity saturation

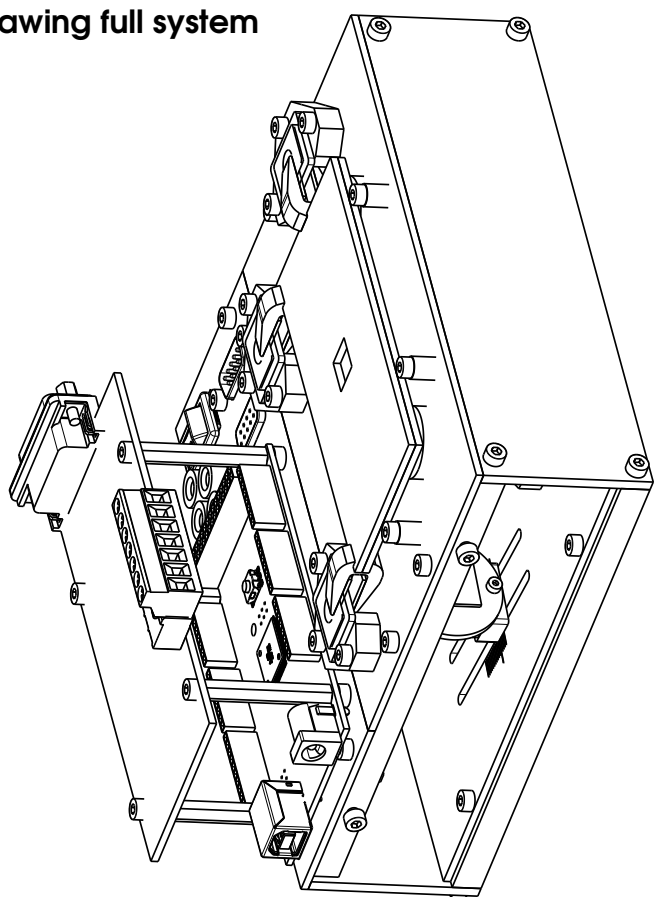
        // Inner-loop
        error_v(); // Determine velocity error between estimation and saturated
                    // velocity
        PID_vel(); // PI inner-loop controller

        // Transformation and plant
        transform(); // Transform principal forces to actuator currents
        move_act(); // Turn currents to PWM duty cycle and let the actuators work

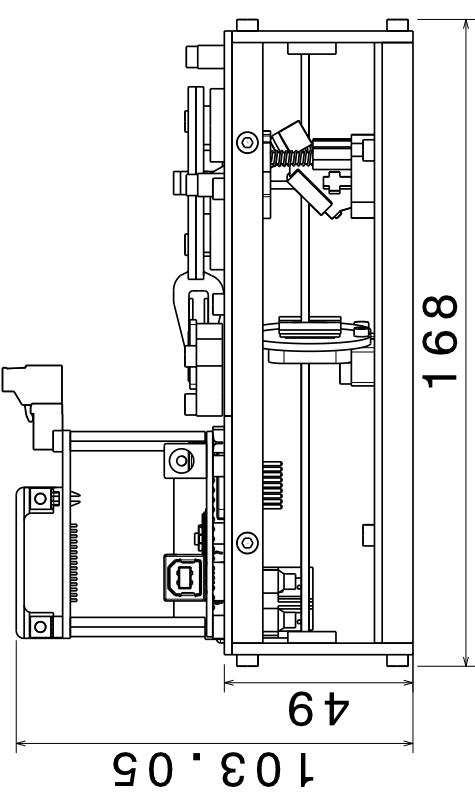
        prev = now; // Determine current time for next loop.
        command = comminterrupt(); // Stop when stop command is given
    }
}
```

A.7 Drawing full system

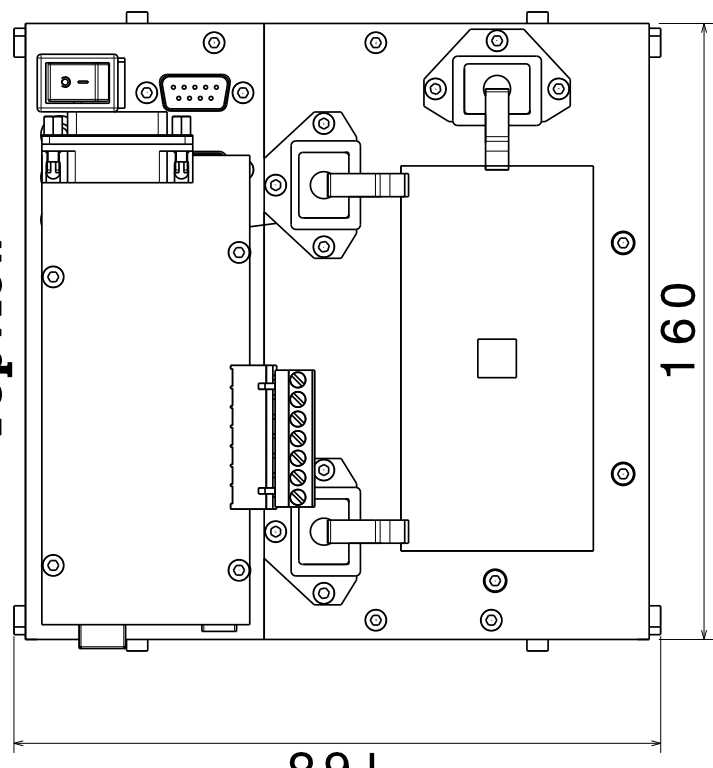
Isometric view



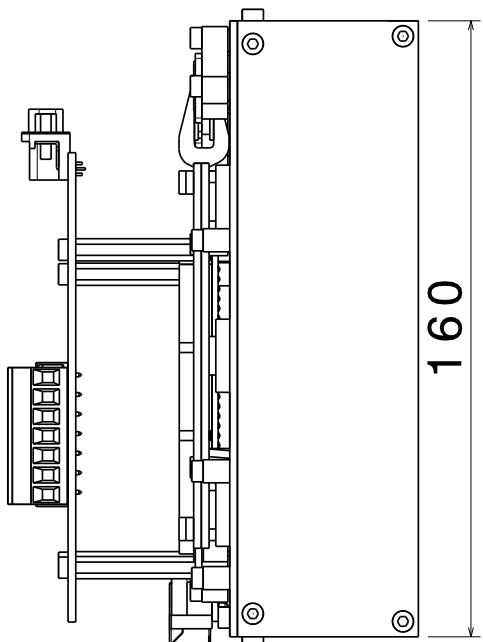
Sideview

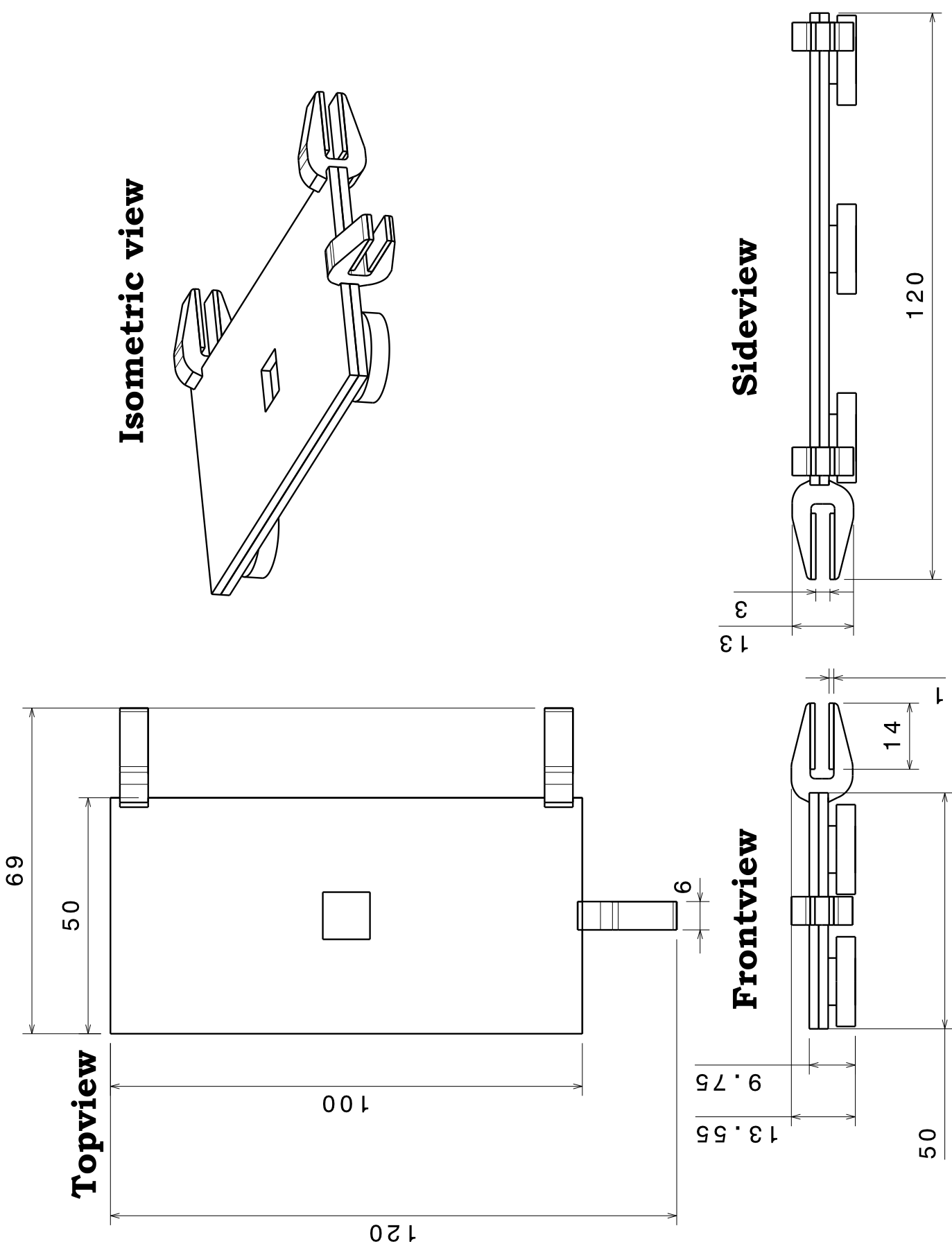


Topview



Frontview



A.8 Drawing mover

A.9 Reference sensor noise measurement



Figure A.10: The laser triangulation sensor optoNCDT

Before the sensor can be used, the noise level needs to be determined. This can easily be done by aiming the sensor to a stationary target and by letting the sensor measure over a long time period. To make sure that the target surfaces are equivalent. The stage is locked on its position with weights and the sensor is measuring the position between the stationary mover and the stationary sensor. The whole setup is placed on a vibration isolation system. The spread in position of the signal is then the noise of the system. The probability density function is shown in Fig. A.11. This measurement is done with a lowpass filter with a cut-off frequency of 10Hz to decrease the noise. This filter is also used in all the validations. The noise of the sensor is spread with a normal distribution. This gives a standard deviation σ of $0.13\mu\text{m}$. Resulting in a 3σ measurement precision of $0.4\mu\text{m}$. The unfiltered response over frequency is shown in a FFT in Fig. A.12, there are no distinguishable noise peaks at certain frequencies. This means that the noise is white and normally distributed.

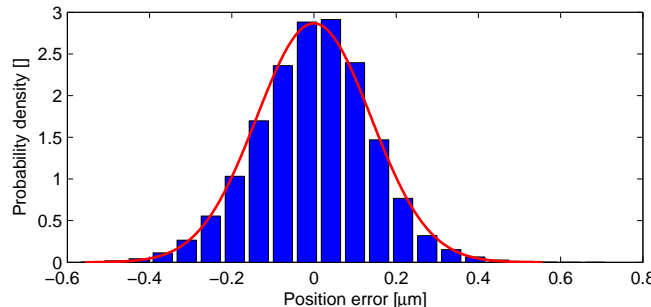


Figure A.11: The probability density function of the sensor output. The sensor is measuring a stationary target, which means that the spread in signal is noise. The signal is filtered with a 10Hz lowpass filter.

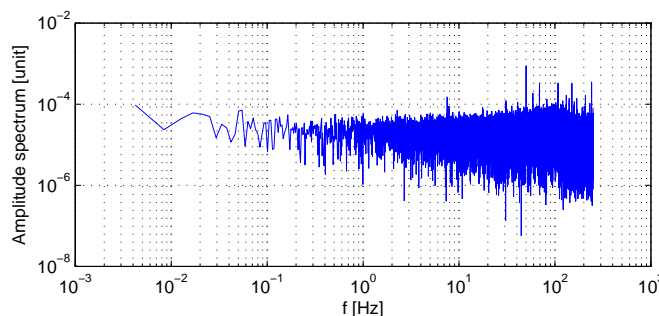


Figure A.12: The FFT of the unfiltered sensor signal, no amplitude peaks could be observed. This means that the noise is pure white.

A.10 How to design your own electronics

During the project, multiple fellow students asked me how I designed my own electronics. In this appendix I'll try to explain in steps how you can create your own PCB's from schematic to fully assembled print. As an example the amplifier board will be used.

Concept

First of all, a concept is required. What do you want the PCB to do?

For the amplifier it was

- Supply and control the current to the Lorentz coils.
- Measure this current.

With the following requirements

- Max 12V DC.
- Min 1A.
- Low ripple current.
- Must work with an Arduino.

Schematic

Draw the circuit in block functions to detailed schematics.

For the amplifier it was something like as shown in Fig. A.13

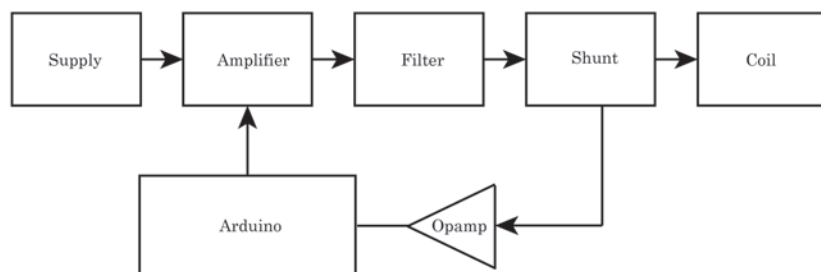


Figure A.13: Schematic block diagram of all the functions

Component selection

Once the concept or schematic is complete, components can be selected. For the amplifier a switched mode h-bridge was preferred, see Section 5.3. Selection can be done on for example on of the following webshops, nl.rs-online.nl or on nl.farnell.com. Personally I prefer Farnell for it's better search engine.

When one h-bridge is found which matches the criteria, it can be selected and imported to a PCB program like EAGLE. On the datasheet of the h-bridge it is described how it must be connected, an example is shown in Fig. A.14. Pay attention to the text in the datasheet, they usually also specify how the signals should be conditioned and what capacitors are needed on the inputs for example. When the components are selected, put them directly in the shopping cart. This makes it easier to order them later on. It is advised to make a prototype on a breadboard before ordering the print.

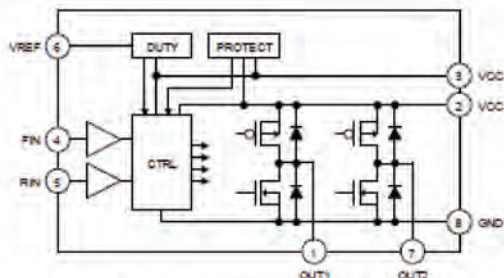
BD6220F / BD6221F

Fig.25 BD6220F / BD6221F



Fig.26 SOP8

Table 1 BD6220F/BD6221F

Pin	Name	Function
1	OUT1	Driver output
2	VCC	Power supply
3	VCC	Power supply
4	FIN	Control input (forward)
5	RIN	Control input (reverse)
6	VREF	Duty setting pin
7	OUT2	Driver output
8	GND	Ground

Note: Use all VCC pin by the same voltage.

Figure A.14: Schematic of how the h-bridge should be connected.

Board design

When the parts are selected they only have to be connected accordingly. When all the important parts like the H-bridge, opamp and connectors are selected, the smaller ones can be done. This results in a system as shown in Fig.A.15. This is one of the 3 amplifier circuits. Starting from right to left we have the supply and ground for the H-bridge. The middle two lines are from the Arduino and are the PWM'ed current signal. This signal is processed by the H-bridge and will try to follow the PWM signal but then with some more power, which is drawn from the supply. This PWM'ed power signal still has a large ripple current and is filtered out by an output filter, the design is shown in Section 5.3.2. I added some LED's over the coils so it is visible when a current is flowing. The current then flows through the coil to deliver a force to the mover. A shunt is put in series so that the current can be measured. Since it is a floating current (it is not connected to ground, because it is bi-polar) it needs to be read out by a differential amplifier. In this particular example the opamp only amplifies with a factor 1, because the signal is big enough. A low-pass filter can be added by putting a capacitor in series with the feedback resistors. The cut-off frequency can be determined with.

$$f_c = \frac{1}{RC} \cdot \frac{1}{2\pi} = 160Hz \quad (A.2)$$

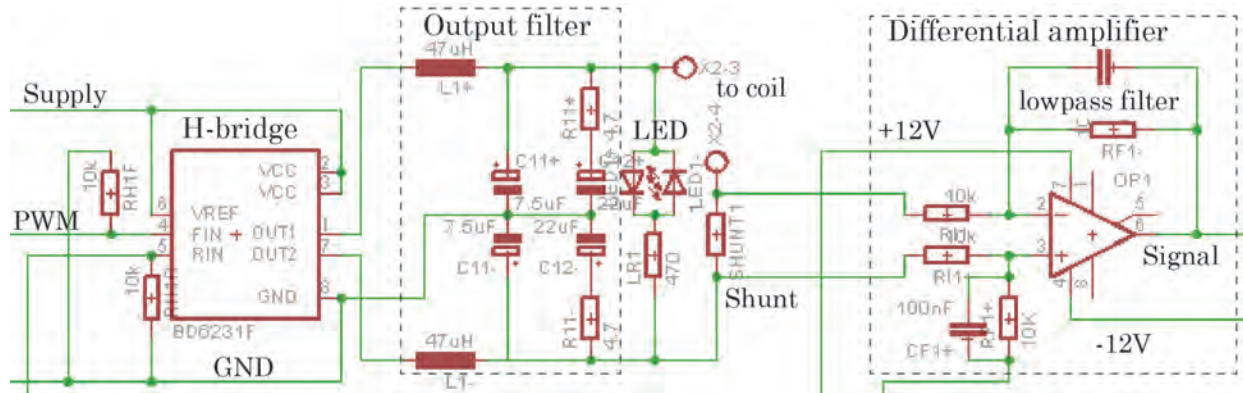


Figure A.15: Detailed schematic of the amplifier

This EAGLE program automatically connects the parts in the board design according to the drawn schematics. Now its just simply dragging the parts to the board. There are some practical tips to reduce cross-talk and noise.

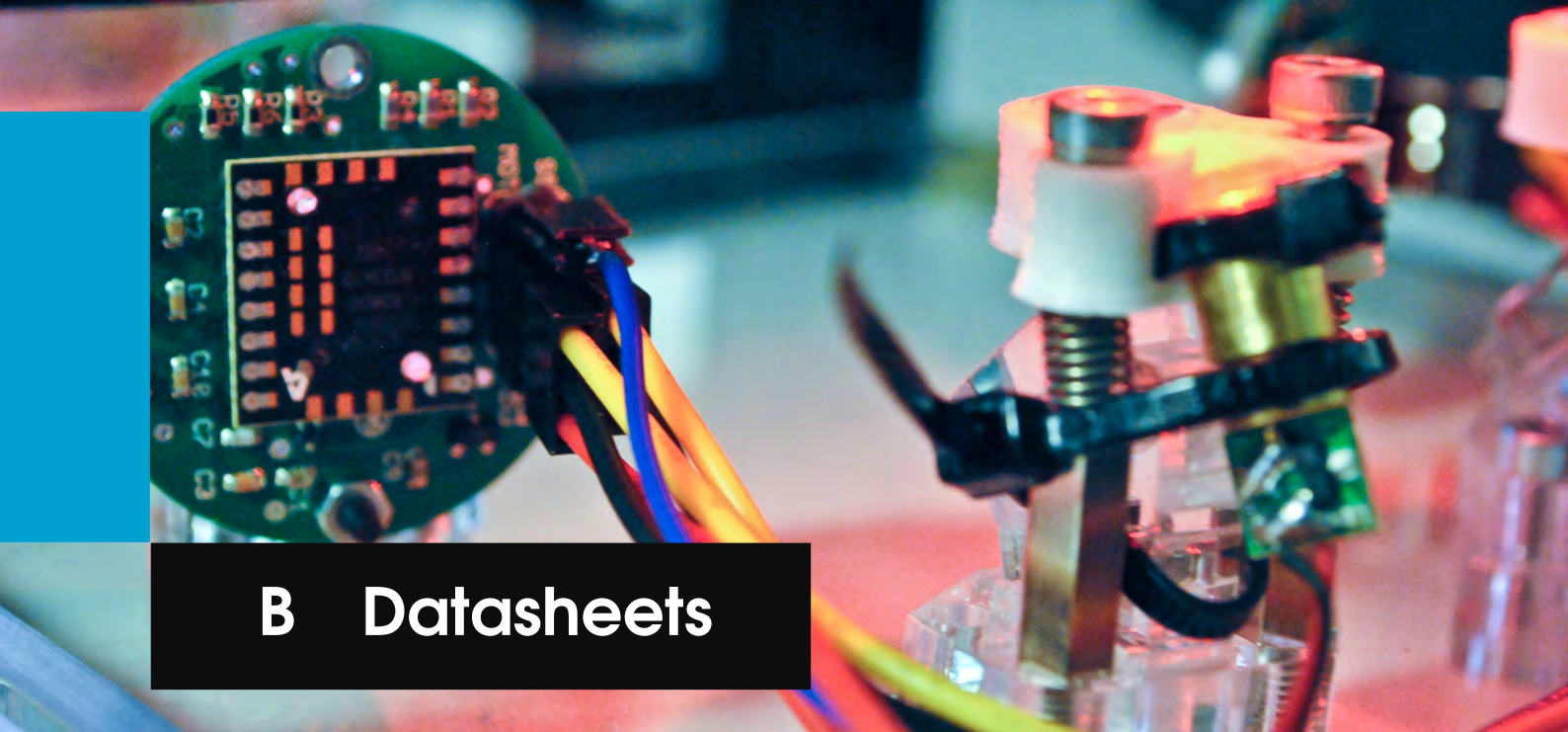
- Add a ground plane, in this example the power ground and measuring ground are separated, they can be made by drawing a polygon and by naming it GND.
- Place components which are noisy far away from the sensitive measurement circuit.
- Place small capacitors of 100nF very close to opamps to regulate a clean supply voltage.
- Add two capacitors with a large range to filter out noise on the input supply voltages. In this example it is done with a 100nF and a 10 μ F.

Before pressing the auto-route button, the design rules needs to be adjusted to what the manufacturer can make. In the design rules different settings like, layers, layer heights, thicknesses, spacings etc can be specified. Else the auto-router will make a design which is for example not producible. If everything is done the auto-route button can be hit and a nice routed board will appear (if not, try to make the routing grid smaller or add more layers). It is also good to add some extra text on the print so that you know what component should be where during assembly.

When everything is connected and you are happy with the design you can send it to a manufacturer. I used Euro-Circuits, it is handy because the EAGLE files can be uploaded directly and they have a visualization tool. You can directly see if your design is interpreted correctly.

Board assembly

When the print is ordered the electronic parts can also be ordered. For RS the components are delivered in one or two days. The prints at Euro-Circuits needs 10 working days. Happy soldering!



B Datasheets

B.1 ADNS 9800



ADNS-9800

Data Sheet



Description

The ADNS-9800 Laser gaming sensor comprises of sensor and VCSEL in a single chip-on-board (COB) package. ADNS-9800 provides enhanced features like programmable frame rate, programmable resolution, configurable sleep and wake up time to suit various PC gamers' preferences.

The advanced class of VCSEL was engineered by PixArt Imaging to provide a laser diode with a single longitudinal and a single transverse mode.

This Laser gaming sensor is in 16-pin integrated chip-on-board (COB) package. It is designed to be used with ADNS-6190-002 small form factor (SFF) gaming laser lens to achieve the optimum performance featured in this document. These parts provide a complete and compact navigation system without moving part and laser calibration process is NOT required in the complete mouse form, thus facilitating high volume assembly.

Theory of Operation

The sensor is based on Laser technology, which measures changes in position by optically acquiring sequential surface images (frames) and mathematically determining the direction and magnitude of movement. It contains an Image Acquisition System (IAS), a Digital Signal Processor (DSP), and a four wire serial port. The IAS acquires microscopic surface images via the lens and illumination system. These images are processed by the DSP to determine the direction and distance of motion. The DSP calculates the Δx and Δy relative displacement values. An external microcontroller reads the Δx and Δy information from the sensor serial port. The microcontroller then translates the data into PS2, USB, or RF signals before sending them to the host PC or game console.

Features

- Small form factor chip-on-board package
- Dual power supply selections, 3 V or 5 V
- VDDIO range: 1.65 – 3.3 V
- 16-bits motion data registers
- High speed motion detection up to 150 ips and acceleration up to 30 g
- Advanced technology 832-865 nm wavelength VCSEL
- Single mode lasing
- No laser power calibration needed
- Compliance to IEC/EN 60825-1 Eye Safety
 - Class 1 laser power output level
 - On-chip laser fault detect circuitry
- Self-adjusting frame rate for optimum performance
- Motion detect pin output
- Internal oscillator – no external clock input needed
- Enhanced Programmability
 - Frame rate up to 12,000 fps
 - 1 to 5 mm lift detection
 - Resolution up to 8200 cpi with ~50 cpi step
 - X and Y axes independent resolution setting
 - Register enabled Rest Modes
 - Sleep and wake up times

Applications

- Corded and cordless gaming laser mice
- Optical trackballs
- Motion input devices

CAUTION: It is advised that normal static precautions be taken in handling and assembly of this component to prevent damage and/or degradation which may be induced by ESD.

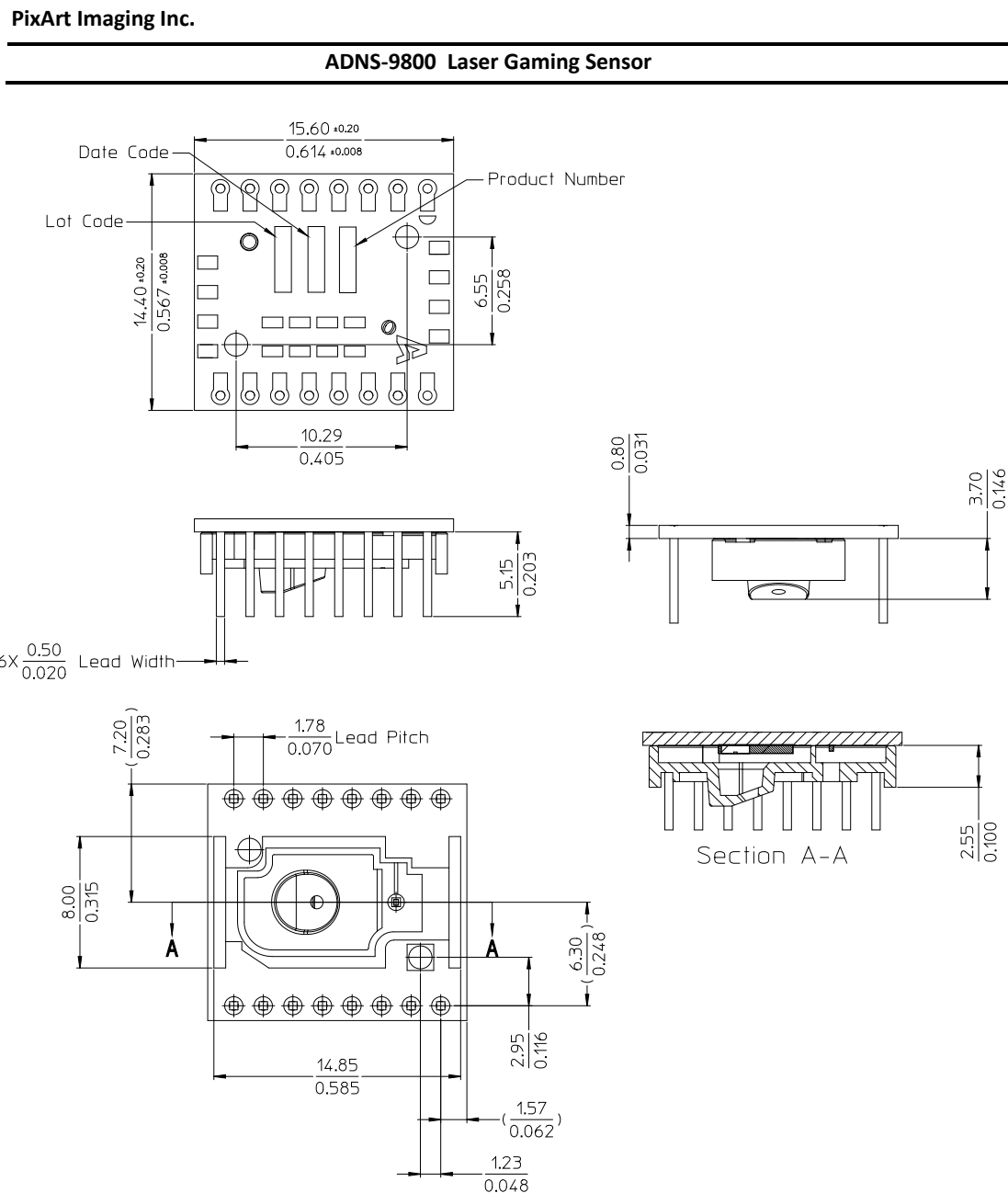


Figure 2. Package outline drawing

All rights strictly reserved any portion in this paper shall not be reproduced, copied or transformed to any other forms without permission.

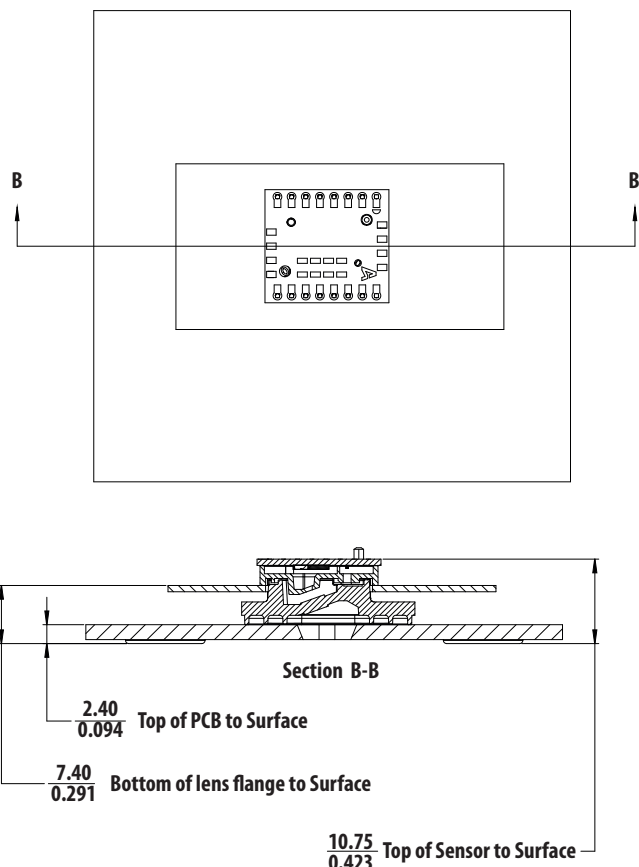
PixArt Imaging Inc.

E-mail: fae_service@pixart.com.tw

PixArt Imaging Inc.

ADNS-9800 Laser Gaming Sensor

Overview of Laser Mouse Sensor Assembly



Note: Dimensions in millimeters/inches and for reference only.

Figure 3. 2D Assembly drawing of ADNS-9800 sensor and ADNS-6190-002 lens coupled with PCB and base plate

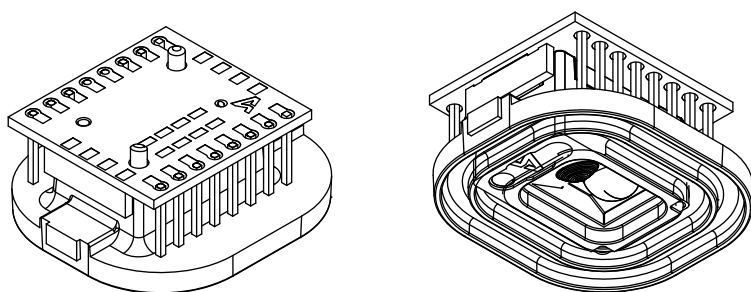


Figure 4. Isometric drawing of ADNS-9800 sensor and ADNS-6190-002 lens

All rights strictly reserved any portion in this paper shall not be reproduced, copied or transformed to any other forms without permission.

PixArt Imaging Inc.

4 E-mail: fae_service@pixart.com.tw

PixArt Imaging Inc.**ADNS-9800 Laser Gaming Sensor****Absolute Maximum Ratings**

Parameter	Symbol	Minimum	Maximum	Units	Notes
Storage Temperature	T _S	-40	85	°C	
Lead-Free Solder Temp			255	°C	For 10 seconds, 1.8 mm below seating plane. See soldering reflow profile in Figure 9.
Supply Voltage	V _{DD5}	-0.5	5.5	V	
	V _{DD3}	-0.5	3.4	V	
	V _{DDIO}	-0.5	3.4	V	
ESD (Human body model)		2	kV	All Pins	
Input Voltage	V _{IN}	-0.5	V _{DDIO} + 0.5	V	All I/O Pins
Laser Output Power	LOP _{max}		716	μW	Class 1 Eye Safety Limit
VCSEL DC Forward Current	I _F		7	mA	For maximum duration of 240 hrs Applicable when driving VCSEL externally and internally using sensor's laser registers setting Refer to reliability datasheet
VCSEL Reverse Voltage	V _R		5	V	I = 10 μA

Notes:

1. Stresses greater than those listed under "Absolute Maximum Ratings" may cause permanent damage to the device. These are the stress ratings only and functional operation of the device at these or any other condition beyond those indicated for extended period of time may affect device reliability.
2. The inherent design of this component causes it to be sensitive to electrostatic discharge. The ESD threshold is listed above. To prevent ESD-induced damage, take adequate ESD precautions when handling this product.

Recommended Operating Conditions

Parameter	Symbol	Minimum	Typical	Maximum	Units	Notes
Operating Temperature	T _A	0		40	°C	
Supply voltage	V _{DD5}	4.0	5.0	5.25	Volts	Including Supply Noise for 5 V mode
	V _{DD3}	2.7	2.8	3.3	Volts	Including Supply Noise for 3 V mode
	V _{DDIO}	1.65		3.3	Volts	Including noise.
Power supply rise time	V _{RT5}	1		100	ms	0 to 5.0 V for 5 V mode
	V _{RT3}	1		100	ms	0 to 2.8 V for 3 V mode
Supply noise (Sinusoidal)	V _{NA}			100	mV _{p-p}	50 kHz – 50 MHz
Serial Port Clock Frequency	f _{SCLK}			2	MHz	Active drive, 50% duty cycle
Distance from lens reference plane to surface	Z	2.18	2.40	2.62	mm	Results in +/- 0.22 mm minimum DOF. Refer to Figure 10.
Speed	S			150	ips	inch/sec
Acceleration	A			30	g	In Run mode only
Load Capacitance	C _{out}			100	pF	MOTION, MISO
Frame Rate	FR			12,000	fps	Frame per second
VCSEL Peak Wavelength	λ	832		865	nm	
Laser Output Power	LOP			506	μW	Operating LOP when assembled with ADNS-6190-002 lens and internally driven by the sensor

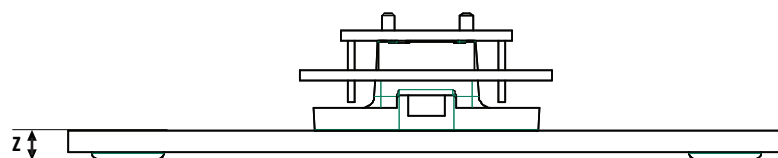


Figure 9. Distance from lens reference plane to surface, Z

PixArt Imaging Inc.**ADNS-9800 Laser Gaming Sensor****DC Electrical Specifications**

Electrical Characteristics over recommended operating conditions.

For 3 V mode, Typical values at 25° C, $V_{DD} = 2.8$ V, $V_{DDIO} = 2.8$ V. For 5 V mode, Typical values at 25° C, $V_{DD} = 5.0$ V, $V_{DDIO} = \text{REFB}$

Parameter	Symbol	Minimum	Typical	Maximum	Units	Notes
DC Supply Current with Variable Frame Rate SROM & in 3 V mode	$I_{DD_RUN3_LOW}$	18	20	mA	Average current, including LASER current. No load on MISO, MOTION.	
	$I_{DD_RUN3_MED}$	24.5	27.5	mA		
	$I_{DD_RUN3_HIGH}$	33	45	mA		
	I_{DD_REST1}	0.26	0.4	mA		
	I_{DD_REST2}	0.12	0.2	mA		
	I_{DD_REST3}	0.08	0.15	mA		
DC Supply Current in 3 V mode	I_{DD_RUN3}	33	45	mA		
DC Supply Current in 5 V mode	I_{DD_RUN5}	36	50	mA		
Peak Supply Current	I_{DDP3}		60	mA	For 3 V mode	
	I_{DDP5}		65	mA	For 5 V mode	
Shutdown Supply Current	$I_{DDSTDWN}$	45	85	mA	NCS, SCLK, MOSI = VDDIO MISO = GND	
REFB Output Voltage	V_{REFB}	2.85	3.05	3.25	V	Do not connect this pin as a supply to other chips other than the integrated VCSEL and VDDIO
Input Low Voltage	V_{IL}		0.3* V_{DDIO}	V	SCLK, MOSI, NCS	
Input High Voltage	V_{IH}	0.7* V_{DDIO}		V	SCLK, MOSI, NCS	
Input Hysteresis	V_{I_HYS}	100		mV	SCLK, MOSI, NCS	
Input Leakage Current	I_{leak}	± 1	± 10	mA	$V_{in} = 0.7*V_{DDIO}$, SCLK, MOSI, NCS	
Output Low Voltage, MISO, MOTION	V_{OL}		0.3* V_{DDIO}	V	$I_{out} = 1$ mA, MISO, MOTION	
Output High Voltage, MISO, MOTION	V_{OH}	0.7* V_{DDIO}		V	$I_{out} = -1$ mA, MISO, MOTION	
Output Low Voltage, LASER_NEN	V_{OL}		0.3* V_{REFB}	V	$I_{out} = 1$ mA, LASER_NEN	
Output High Voltage, LASER_NEN	V_{OH}	0.7* V_{REFB}		V	$I_{out} = -0.5$ mA, LASER_NEN	
Input Capacitance	C_{in}		10	pF	MOSI, NCS, SCLK	

All rights strictly reserved any portion in this paper shall not be reproduced, copied or transformed to any other forms without permission.

PixArt Imaging Inc.

E-mail: fae_service@pixart.com.tw

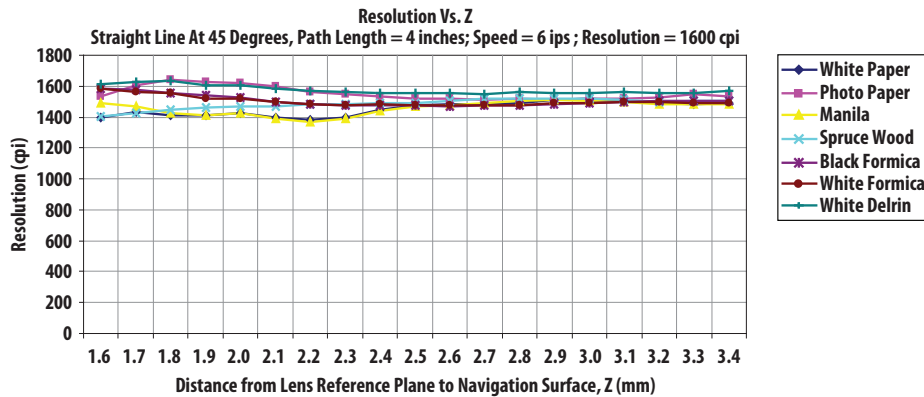
PixArt Imaging Inc.**ADNS-9800 Laser Gaming Sensor****Sensor's Typical Performance Characteristics**

Figure 10. Mean Resolution vs. Z at default resolution at 1600 cpi

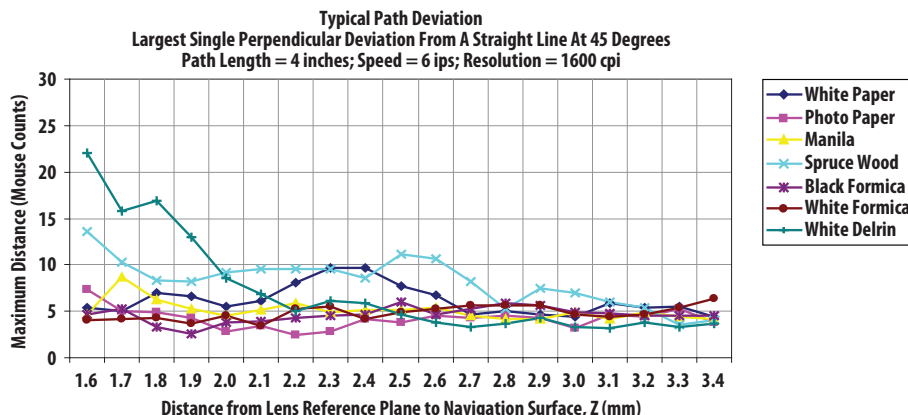


Figure 11. Average Error vs. Distance at default resolution at 1600 cpi (mm)

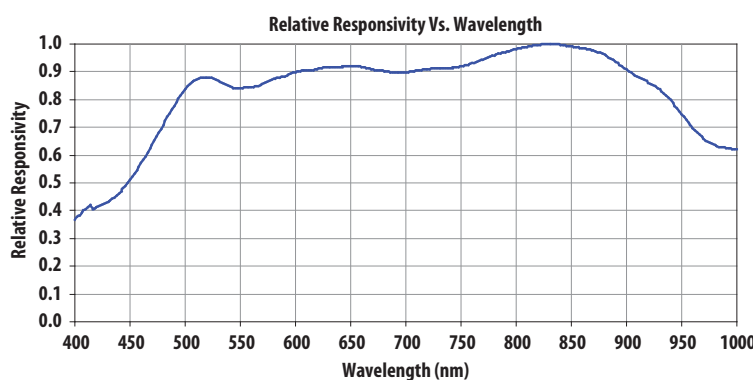


Figure 12. Wavelength Responsivity

All rights strictly reserved any portion in this paper shall not be reproduced, copied or transformed to any other forms without permission.

PixArt Imaging Inc.

E-mail: fae_service@pixart.com.tw

B.2 Thorlabs Linear Stage DDSM100

Chapter 6 Specification

Parameter	Value
Travel Range	100 mm (3.9")
Velocity (Max)	500 mm/s
Acceleration (Max)	5000 mm/s ²
Bidirectional Repeatability	±1.5 µm
Backlash	N/A (No Leadscrew)
Min Incremental Movement	500 nm
Horizontal Load Capacity	0.9 kg (1.98 lbs)
Absolute On-Axis Accuracy	±5.0 µm
Straightness/Flatness	±5.0 µm
Pitch	±175 µrad
Yaw	±175 µrad
Continuous Motor Force	0.8 N
Peak Motor Force (5 sec)	2.3 N
Bearing Type	High Rigidity Recirculating Precision Linear Bearing
Limit Switches	Magnetic Sensor at Each End of Stage
Operating Temperature Range	5 to 40 °C (41 to 104 °F)
Motor Type	Brushless DC Linear Motor
Cable Length	1 m (3.3')
Dimensions (Mid Travel)	195 mm x 57 mm x 35 mm (7.7" x 2.25" x 1.38")
Weight (with cables)	0.72 kg (1.6 lbs)

*Note

The default tuning parameters can be changed to optimise settling times for a specific load - see Section 4.1.

Caution

The maximum speed and acceleration values quoted can be safely achieved with the maximum load and a high duty cycle. However in this case, some heating of the stage may occur and dimensional stability of the stage may be affected. This could result in less than optimal repeatability and accuracy. For cases where repeatability and accuracy are critical it is recommended that the stage temperature is allowed to reach a steady state before measurements are taken. Alternatively the load, acceleration and duty cycle should be reduced from the maximum values. Some trial and error in setting these values may be necessary before the ideal settings are attained.

B.3 MICRO-EPSILON optoNCDT 1402-5

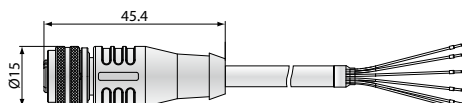
Model	ILD 1402-5	ILD 1402-10	ILD 1402-20	ILD 1402-50	ILD 1402-100	ILD 1402-200	ILD 1402-250VT	ILD 1402-400	ILD 1402-600	
Measuring range	5mm	10mm	20mm	50mm	100mm	200mm	250mm	400mm	600mm	
Start of measuring range	SMR	20mm	20mm	30mm	45mm	50mm	60mm	100mm	200mm	
Midrange	MMR	22.5mm	25mm	40mm	70mm	100mm	160mm	225mm	400mm	
End of measuring range	EMR	25mm	30mm	50mm	95mm	150mm	260mm	350mm	600 mm	
Linearity ¹⁾	5...9µm	5...18µm	7...36µm	12...90µm	20...180µm	40...360µm	50...1200µm	120...2000µm	120...3000µm	
				≤0.18% FSO				≤0.5% FSO		
Resolution ²⁾	averaged with averaging factor 64	0.6µm	1µm	2µm	5µm	10µm	13µm	32µm	80µm	
						0.01% FSO				
Resolution ²⁾	dynamic 1.5 kHz	1...3µm	2...5µm	5...10µm	6...25µm	12...50µm	13...100µm	32...300µm	80...480µm	
						0.02...0.05% FSO		0.02...0.12% FSO		
Measuring rate, programmable						1.5kHz; 1kHz; 750Hz; 375Hz; 50Hz				
Light source						semiconductor laser <1mW, 670nm (red)				
Laser safety class						class 2 IEC 60825-1 : 2008-05				
Spot diameter	SMR	110µm	110µm	210µm	1100µm	1400µm	2300µm	5000µm	2.6 x 5mm	
	MMR	380µm	650µm	530µm	110µm	130µm	2200µm	5000µm	2.6 x 5mm	
	EMR	650µm	1200µm	830µm	1100µm	1400µm	2100µm	5000µm	2.6 x 5mm	
Protection class						IP 67				
Vibration					15g / 10Hz ... 1kHz		20g / 10Hz...1kHz	15g / 10Hz...1kHz		
Shock						15g / 6ms (IEC 68-2-29)				
Weight (without cable)					appr. 83g			appr. 130g		
Temperature stability				0.03 % FSO/°C			0.08 % FSO/°C			
Operation temperature						0 ... +50°C				
Storage temperature						-20 ... +70°C				
Output	analogue			4 ... 20mA (1 ... 5V with cable PC 1402-3/U); free scalable within the nominal range						
	digital					RS422 / 14bit				
Control I/O				1x open collector output (switching output, switch, error); 1x input (teach in, trigger); 1x laser on/off						
Supply					11 ... 30VDC, 24VDC / 50mA					
Controller						integrated signal processor				
Software					free setup and aquisition tool + SDK (software development kit)					
Electromagnetic compatibility (EMC)					EN 61326-1:2006 / EN 55011 Class B (Interface emission) EN 61326-1:2006 / EN 61000-4-2:1995 + A1:1998 + A2:2001 (Interference resistance)					

FSO = Full scale output All specifications apply for a diffusely reflecting matt white ceramic target

¹⁾ values apply for 0 - 30% FSO and 30 - 100 % FSO ²⁾ resolution digital output 14bit

SMR = Start of measuring range MMR = Midrange EMR = End of measuring range

Connector axial



12-pin-connector
(view on solder termination side of male inserts)



Pin	Description	colour PC1402-x/I
3	RS422 Rx+	serial input
4	RS422 Rx-	serial input
5	RS422 Tx+	serial output
6	RS422 Tx-	serial output
7	+U B	11-30DV 24V MP
8	Laser off	switch input
9	Teach in	switch input
10	Error	switch output
11	I OUT	4 ... 20mA
12	GND	supply and signal ground
1/2	n.c.	

The cable screen is connected with the sensor housing. The interface and power supply cable are robot rated and UL certified. At one end there is a 12pin M12 connector, the other end is open.